Continuum description of living matter

Mehrana R. Nejad

Rudolf Peierls Centre for Theoretical Physics

University of Oxford

A thesis submitted for the degree of

Doctor of Philosophy in Theoretical Physics

Michaelmas 2023

Abstract

Living systems are one of the most complex forms of matter. Among their many different aspects, one unifying property of any living matter is activity. Active materials continually extract energy from their surroundings to move, grow, and self-replicate [1].

To perform these functions, active units exert forces on their environment and this raises the question of the extent to which the behaviour of biological systems can be understood by measuring forces and flows and using the generic physical theories of active matter.

At the microscale, several important aspects of the dynamics of living systems can be described by the theories of active nematics. We discuss, in the second chapter of this thesis, that long-range interactions in active suspensions at the microscale have a nematic symmetry, and this makes active nematic models a powerful tool for studying living systems.

In this thesis, we extract essential features from living systems in experiments to build continuum active nematic models that are able to capture the behaviour of the experiments. Using the continuum models, we then perform numerical simulations and linear stability analyses to explore the dynamical steady states of the model, and compare them with the ones in the experiments. We show that the conventional active nematic models need to be modified and evolved, according to the active system under study, to allow us to capture the patterns observed in different experiments.

Our results indicate that fractal-like patterns that form at the interface of bacterial droplets cannot be explained by the conventional active biphasic models. We suggest that the presence of an active layer at the bacterial interface produces the cell orientation and flow patterns in the experiments.

We then construct a continuum description for living tissues and demonstrate that introducing new continuum fields associated with cell area and aspect ratio and decoupling the direction of the active force from the cell elongation, introduces new phases to the system. Analysing experimental data on MDCK cells, we use our model to understand the misalignment in the cell shape and stress orientation in the experiments.

Finally, we extend our study to three dimensions and show that active materials with extensile activity promote formation of twist-type defects and three-dimensional flows.

To my parents, Mahboube and Ali

Acknowledgements

I am first and foremost thankful to my supervisor Julia Yeomans for introducing me to the world of biophysics and for her unwavering support and guidance. I am grateful for all the opportunities you offered me, for enjoyable scientific discussions, and for allowing me to establish my own research interests and way of thinking. I could not have grown as much without you. I also appreciate your support beyond physics - it was very heartwarming to have you not only as a thoughtful supervisor but also as a friend. I immensely enjoyed the time I spent with your family.

For the many fruitful scientific discussions, thank you to many former and current members of the group: Amin Doostmohammadi, Kristian Thijssen, Sumesh Thampi, and Jan Rozman. It has been a pleasure collaborating with you.

I would also like to thank my experimental collaborators Yilin Wu, Haoran Xu, Jacob Notbohm, Jay Zhang, Stefano Guido, Sergio Caserta, and Molly McCord. I learned a lot about living systems, through these collaborations and by trying to build models for these experiments.

I also thank the members of the Yeomans group, in particular James Graham, and Ioannis Hadjifrangiskou who proofread some part of this thesis. I also thank Francesco Mori, Samantha Lish, Liam Ruske, Saraswat Bhattacharyya, and Muriel van der Laan for our social meetings and board game evenings.

I would also like to thank Shuofeng Zhang, Wilber Lim, Yoonsoo Nam, and Hanzhi Zhang for being great officemates in the Beecroft Building, and I am grateful for the amazing discussions and conversations that emerged from working alongside each other.

I would also like to thank Ali Najafi for introducing me to fluid dynamics before starting my DPhil at Oxford. My background in fluid dynamics has been helpful to me during my research and has helped me gain a deeper understanding of my work.

A Clarendon Fund Scholarship supported my DPhil. I am incredibly grateful for the opportunity and community Clarendon provided. I enjoyed many of the events that were organised by the Clarendon panel, from all the trips to gallery visits, from taking part in competitions to all the hikes and walks. In particular, I thank Ajantha Abey, Ayako Hatano, Marston Bailey, Dylan Sherman, Diyi Liu, and Souvik Giri for all their efforts in organising the awesome events.

I thank Eliska Harris for all the lovely walks, discussions, cake and coffees, ice creams, and trips. I enjoyed the time I spent with you and learned a lot about humanities, social sciences, culture and tradition, and art from you.

I also thank the Lincoln College social reps, Michael Goode, Maria Murad, and Matthew Ball for organising pub quizzes, music nights, painting competitions, scavenger hunts, and tours. These events led to knowing people from different fields, which helped me to gain a better insight into the world outside physics.

My time in Oxford would not have been the same without you: Mariona Eiren Miyata-Sturm, and Siyuan Yan. Thank you so much for being wonderful friends, and for all the walks, talks, picnics, discussions, dinners, cinemas, and trips.

I also thank Grace Borchert, for being an amazing friend, and for all the trips, concents, and gallery visits.

I also thank the Oxford Walking group for organising many relaxing walks, and also the Oxford Basketball team. Taking part in these activities brought me so much joy.

Publications

Authored publications contributing to this thesis

- S. Santhosh, M. R. Nejad, A. Doostmohammadi, J. M. Yeomans, and S. P. Thampi, Activity induced nematic order in isotropic liquid crystals, *J. Stat. Phys. 180*, 699 (2020).
- K. Thijssen, M. R. Nejad, and J. M. Yeomans, Role of Friction in Multidefect Ordering, *Phys. Rev. Lett.*, 125, 218004 (2020).
- M. R. Nejad, A. Doostmohammadi, and J. M. Yeomans, Memory effects, arches and polar defect ordering at the crossover from wet to dry active nematics, *Soft Matter*, 17, 2500 (2021).
- S. A Sultan, M. R Nejad, and A. Doostmohammadi, Quadrupolar active stress induces exotic patterns of defect motion in compressible active nematics, *Soft Matter*, 18, 4118 (2022).
- M. R. Nejad and J. M. Yeomans, Active extensile stress promotes 3D director orientations and flows, *Phys. Rev. Lett.*, 128, 048001 (2022).
- F. Ascione, S. Caserta, S. Esposito, V. R. Villella, L. Maiuri, M. R. Nejad, A. Doostmohammadi, J. M. Yeomans, and S. Guido, Collective rotational motion of freely expanding T84 epithelial cell colonies, *J. R. Soc. Interface*, 20, 20220719 (2023).
- H. Xu, M. R. Nejad, J. M. Yeomans, and Y. Wu, Geometrical control of interface patterning underlies active matter invasion, 120, *Proc. Natl. Acad. Sci. U.S.A.*, e2219708120 (2023).
- M. R. Nejad, and J. M. Yeomans, Spontaneous rotation of active droplets in two and three dimensions, *arXiv:2305.04018* (2023).
- M. R. Nejad, L. J. Ruske, M. McCord, J. Zhang, G. Zhang, J. Notbohm, and J. M. Yeomans, Stress-shape misalignment in confluent cell layers, *arXiv:2309.04224* (2023).

Other publications contributing to this thesis

- M. R. Nejad, G. Zhang, and J. M. Yeomans, Continuum approach for cell monalyers, *in preparation* (2023).

Contents

List of Figures

The love for all living creatures is the most noble attribute of man.

Charles Darwin

1 Introduction

1.1 Living matter

The intricate and captivating world of living systems has long been a subject of wonder and curiosity. As we explore biology, we uncover an astounding array of structures, processes, and behaviors that collectively give rise to the diversity of life on Earth. Yet, beneath the surface of this biological complexity lies a fundamental truth: living systems are governed by the principles of physics [1–4]. The convergence of biology and physics has given birth to a fascinating interdisciplinary field known as the *physics of living systems* [5–7].

From the way cells communicate and self-organize to the dynamics of ecosystems and the emergence of collective behaviors in animal groups, the physics of living systems provides a framework for understanding the underlying principles that give rise to these phenomena [8–12]. This interdisciplinary approach has led to groundbreaking insights into a range of topics, including the mechanics of cell movement [13–15], the patterns of biological growth and development [16–18], and even the dynamics of neural networks in the brain [19, 20]. The field's broad scope extends to various levels of biological organization, from the microscopic world of molecules to the macroscopic interactions of ecosystems.

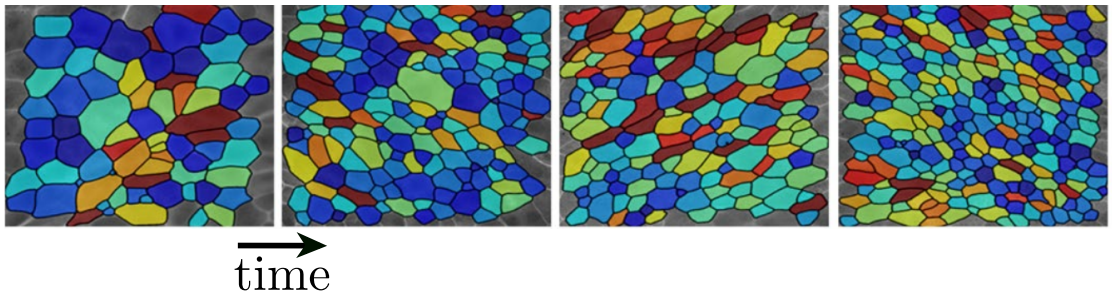

Figure 1.1: Cells change their shapes during maturation. As maturation continues, cells become more isotropic and become jammed. The experiment is performed on a *pseudostratified bronchial* epithelial layer. The snapshot is adopted from Ref. [30].

1.1.1 Living systems at microscale

The rules that govern life's behaviors at microscale are often quite distinct from those at larger scales [21, 22], as microorganisms navigate their world using diffusion, and molecular interactions as their guiding forces.

A bacterium, a micrometer-size unicellular organism that lacks a distinct nucleus and membrane-bound organelles, is one of the simplest living creatures that carry out essential life processes, including metabolism, growth, and responding to their environment. To do these functions, it obtains energy through various mechanisms, such as photosynthesis, chemosynthesis, or by consuming organic material from its surroundings. When thousands of bacteria exist in a fluid environment, they show intriguing patterns of collective motion [23, 24]. The phenomenon of collective motion among bacteria stands out as a remarkable illustration of emergent behavior.

Another example of living systems at the microscale is a cell monolayer such as an epithelial layer. Epithelial tissues, which form the linings and coverings of organs and body surfaces, exhibit an interplay of mechanical forces and cellular interactions, shaping the growth, development, and function of organisms. The ability of these cell layers to dynamically rearrange [25], change their shape and elongate [26], and collectively migrate during development [27, 28], wound healing [29], and organ formation has recently attracted a lot of interest in the physics community. **Fig. 1.1** shows cell shape changes during epithelial maturation.

1.2 Introduction to mathematical modeling of living matter

Despite the biological complexity of living matter, there is a potential to uncover many underlying patterns and principles through mathematical modeling. By transforming biological questions into mathematical constructs, physicists can help to bridge the gap between theory and experiments.

To describe the behaviour of living systems at the microscale, three general approaches are commonly used: agent-based simulations, continuum models, and phase field models. In the following subsections, we give an outline of these approaches.

1.2.1 Agent based models

Showing how individual interactions lead to emergent behaviors, agent-based models offer a versatile tool for understanding the dynamics of cells, molecules, and other microscopic entities within complex biological environments. By assigning characteristics such as movement, growth, division, and communication to cells, one can construct a virtual model that mirrors real-world biological processes. Agent-based models also allow for the modeling of individual differences among agents. This enables the exploration of how these subtle variations lead to emergent behaviors and patterns that might not be apparent, or be hard to achieve through continuum descriptions.

The Vicsek model was one of the earliest computer implementations of an agent-based approach [31, 32]. This model was initially used to describe a macroscopic flock of birds using interacting particles. The particles have a fixed speed and prefer to align their velocity vectors parallel to their neighbors. As a result of neighbor-neighbor aligning interactions, a transition between the disordered random motion of units to a phase with collective directed motion can arise. The transition is called flocking transition, and in contrast to passive magnets, can happen in two dimensions.

Another example of an agent-based approach is simulations of bacterial rods that interact with their surrounding rods by directed motion, excluded volume, or

growth. These models can be used to study various biological phenomena, including bacterial colony formation, biofilm development [33], antibiotic resistance, and the effects of different environmental conditions on bacterial behavior [34].

Agent-based models are a useful tool to study the dynamics of individual active units in a group, and in particular, for studying the effects of variations in single species in a multi-species system. However, many of the emergent phenomena in active systems appear when the number of active units exceeds a threshold. In this regime, agent-based models are computationally expensive, and continuum models provide a more efficient approach to understanding collective behaviour.

1.2.2 Continuum models

Continuum models treat biological systems as continuous media, where variables such as concentration, density, and stress are represented as functions that vary smoothly across space and time. By expressing these variables using partial differential equations, we can capture the essential dynamics of microscale living systems, accounting for processes like diffusion, reaction, growth, motion, and mechanical interactions.

The strength of continuum models lies in their ability to describe macroscopic trends and behaviors while averaging out microscopic details. This allows us to gain insights into the overall trends and patterns that emerge from the collective actions of numerous individual components. Continuum models are particularly effective in scenarios where the detailed interactions between individual entities are less crucial than understanding the system's overall behavior.

These models find applications in a diverse array of microscale living systems. Within cell biology, continuum models can describe processes like nutrient transport, intracellular signaling, and cell polarization. In tissue engineering, they help predict the growth and remodeling of tissue structures.

The first continuum model introduced to study the behaviour of living material was the Toner-Tu model [35, 36]. This model uses a phenomenological approach to write down the continuum equations to describe a flocking transition. The Toner-Tu

model was built to describe bird flocks, and as such the dynamics is governed by inertia. This regime is different from the regime in which microscale biological systems live. At the microscale, the Reynolds number is low and the dynamics is governed by highly viscous flows. To study living organisms in a low Reynolds number regime, the Toner-Tu model was later modified [3, 37–39]. It was shown that in a low Reynolds number regime, living units produce long-range flows, which mediate long-range interactions in an active suspension at the microscale. As a result, when interested in the collective behaviour of systems, the long-range interaction allows us to ignore many of the microscopic details of the individual active units. In addition, since the flow created by each unit has a nematic symmetry, the symmetry of a nematic liquid crystal, in many cases one can use theories of *active nematics* to predict the collective behaviour of living systems at microscale [1, 3, 24, 40–45].

1.2.3 Phase field model

The phase field model is a mathematical framework used to describe the evolution of interfaces and phase boundaries in various systems, including materials, fluids, and biological systems such as cells. In the context of cells, particularly in developmental biology and tissue growth studies, the phase field model can be employed to simulate the motion of cells, their shape changes, and their interactions within a tissue [46, 47].

The phase field model for cells incorporates principles from both agent-based and continuum models: each cell is represented by a continuous field that varies across space. This field assigns a value to each point in space, indicating the *state* of that point with respect to the presence of a cell. The phase field can take on different values to represent different cell states, such as *inside the cell*, *outside the cell*, *cell boundary* or even different cell types.

The phase field model typically involves an energy functional that describes the total energy of the system. This functional includes terms related to the cell-cell interactions, cell-substrate interactions, and other relevant factors. The system evolves over time to minimise this energy, leading to changes in the phase field that represent cell movements, deformations, and interactions. The model can also

be extended to include additional factors such as mechanical properties, chemical signaling, adhesion forces, and active interactions between neighbouring cells, making it a versatile tool for studying various aspects of cell behavior and tissue dynamics.

1.3 Thesis outline

This thesis demonstrates how continuum active nematic models can be modified to account for the features of living systems in different experimental settings. In particular, we distinguish between living materials such as bacteria, in which units have a fixed shape, and the direction of the force is along the symmetry axis of the cells, and living materials such as tissues, in which cells change their shape, and the direction of the force is set by an internal degree of freedom, interior active filaments, instead of cell shape. This is the path to using continuum modeling to help investigate behaviour of living matter.

In this thesis, we use a continuum approach based on the physics of active nematics, to study and understand the collective dynamics of living systems at microscale and in different settings.

In chapter 2 we introduce the conventional continuum model of active nematics and the numerical implementation of the model.

In chapter 3 we show that depending on the ground state of the free energy (nematic or isotropic phase), increasing friction in active nematic systems leads to the formation of polar or nematic ordering of $+1/2$ defects.

In chapter 4 we modify the conventional active nematohydrodynamic model to account for the features observed in *P. mirabilis* bacterial droplets, and we show that this allows us to understand the fractal-type invasion patterns that form at the interface of the droplet. We then compare our results, describing the role of the interface curvature on the formation of the patterns, with the experiments.

In chapter 5 of this thesis, we use concepts underlying the phase field model to build a more coarse-grained model for living tissues. We develop a continuum model that accounts for the area and aspect ratio change of deformable cells. The model also introduces a new field for the direction of the active stress. This has

been neglected in the continuum models studied so far, and we later show that it is a necessary ingredient for understanding the behaviour of living tissues.

In chapter 6 we analyse the experimental data on *MDCK* and *LP9* cells, and report the formation of extensile regions in a contractile monolayer. We then use the continuum model that we constructed in chapter 5, and show that the model captures the formation of extensile regions in contractile monolayers, and the key features of the experiments, including spatiotemporal correlations in the orientation of cell shape and the stress.

Finally, to understand the difference between active material in two and three dimensions, in chapter 7 we study the behaviour of flows and disclination lines in three dimensions and show that, extensile active stress promotes three-dimensional flows and forms twist disclination lines.

The past is solid, the future is liquid.

Jean-Louis Aubert

2

Continuum description of liquid crystals

This chapter establishes the theoretical framework upon which the remainder of this thesis is constructed. We investigate active fluids with high viscosity, and at a micron-scale, where the Reynolds number is small. We consider systems in which the long-range flows are produced by active units that have a nematic symmetry. This allows us to use the theories of active nematics [1]. In addition, we study systems at spatial scales that are large compared to the size of a single active unit, which allows us to use a continuum description for the system.

We commence this chapter by introducing nematic liquid crystals, which we characterise using a tensor order parameter. Subsequently, the symmetry of the nematic tensor is used to formulate a Landau-de Gennes free energy [48]. The free energy parameters determine if the system's ground state is an isotropic phase or a phase with a nematic order. The free energy also allows for the formation of discontinuities in the orientation field called defects.

We then introduce the nematohydrodynamic equations, which are coupled equations for the dynamics of the liquid crystal and the surrounding velocity field, and introduce the Cahn-Hilliard equations, which allow us to study liquid crystal droplets.

Lastly, we introduce active stress and the instabilities it produces in active nematics. We use linear stability analysis and first look at the growth rate of

instabilities in a regime in which, without activity, the liquid crystal forms a nematic phase. We then study a case in which, without activity, the liquid crystal forms an isotropic phase. We show that different types of active instabilities destabilise the homogeneous phase in these two regimes. Both systems form defects, and active turbulence, a state with collective flows and vortices.

2.1 Passive liquid crystals

Liquid crystals are a unique state of matter that exhibits properties that are intermediate between those of conventional liquids and solids. They possess a molecular orientation similar to that of solids, but they also retain the ability to flow like liquids. **Fig. 2.1**(a) compares the arrangement of molecules in a solid, and in a liquid, with a liquid crystal [49].

The molecules in a liquid crystal are typically elongated or rod-like, and they tend to align themselves along a preferred direction, which in the absence of an external field is random. Depending on their alignment, liquid crystals can be classified into different phases, with the most common ones being isotropic and nematic phases [48, 50, 51]. The isotropic and the nematic phases of the liquid crystal are shown in **Fig. 2.1**(b) and (c), respectively.

In an isotropic phase of liquid crystals, nematogens lack long-range positional and orientational order. In a nematic phase, nematogens show long-range directional order, but they lack any long-range positional order.

2.1.1 Nematic order parameter

To distinguish between nematic and isotropic phases of a liquid crystal, one can define a nematic tensor, which is a second-rank tensor, often denoted as $\mathbf{Q}$. The nematic tensor helps quantify the directional alignment of molecules in a way that reflects both their average orientation and the degree of order present. The nematic tensor is defined by averaging over the orientation of many elongated

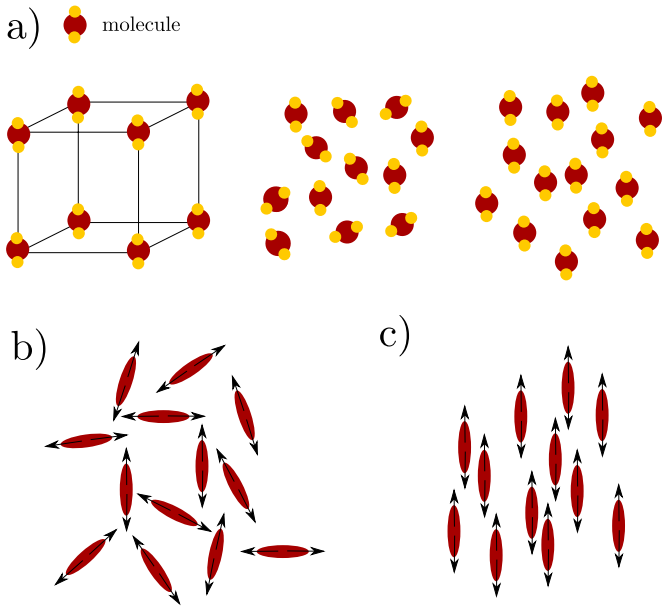

Figure 2.1: (a) Left: In solids, molecules demonstrate both positional and orientational order - meaning they are restricted to specific directions and positions relative to each other. In contrast, liquids (in the middle) lack both positional and orientational order; molecules in liquids exhibit random directions and positions. Right: liquid crystals exist between the solid and the liquid phase - the molecules in a liquid crystal do not exhibit any positional order, but they do possess a certain degree of orientational order. (b) In an isotropic phase of nematic liquid crystals, nematogens lack long-range positional and orientational order. (c) In a nematic phase, nematogens show long-range directional order, but they lack any long-range positional order.

particles. In d-spatial dimensions, this reads

$$\mathbf{Q} = S(\mathbf{nn} - \frac{\mathbf{I}}{d}) := \frac{1}{N}\sum_{\alpha=1}^{N}\left(\mathbf{c}_\alpha\mathbf{c}_\alpha - \frac{\mathbf{I}}{d}\right), \tag{2.1}$$

where the sum is over a local number of particles N with individual directions $\mathbf{c}_\alpha$, and $\boldsymbol{I}$ shows the unit tensor [48]. In this definition, $0 \leq S \leq 1$, denotes the average magnitude and $\mathbf{n}$ is the average direction of the nematic order. In an isotropic phase (**Fig. 2.1**(b)), the average $\frac{1}{N}\sum_{\alpha=1}^{N}(\mathbf{c}_\alpha\mathbf{c}_\alpha) \sim \mathbf{I}/d$, and as a result the magnitude of the order S is zero. In a phase with complete nematic order where all the particles are aligned in a specific direction (**Fig. 2.1**(c)), the summation in **Eq. 2.1** simplifies and we have $S = 1$.

2.1.2 Transition from isotropic to nematic phase

By manipulating external factors such as temperature, concentration of particles, or mechanical stress, one can induce a transition from an isotropic phase to a nematic phase [48].

From a physics standpoint, this transition can be explained through the concept of symmetry breaking. In the isotropic phase, molecules exhibit rotational symmetry, meaning their orientations are equally probable in all directions. As the system cools, this rotational symmetry is broken, leading to a preferred direction for molecular alignment. The direction of the order is chosen randomly through the spontaneous breakdown of symmetry.

Mathematically, the transition is often described using the Landau-de Gennes free energy. The Landau-de Gennes free energy $\mathcal{F}_{\mathcal{LD}}$, rooted in statistical mechanics and symmetry principles, provides a mathematical description that quantifies the system's energy based on order parameters associated with molecular orientation. It captures the balance between energetic costs due to misaligned molecules, that in the absence of an external field comes from the excluded volume interaction between the molecules and entropic energetic gains from alignment. In the case of the isotropic to nematic transition, the free energy landscape favors nematic order when the alignment's energy gain outweighs the entropy cost of the order.

The Landau-de Gennes free energy assumes an expansion of the free energy in powers of the order parameter $\mathbf{Q}$, and its spatial derivatives $\boldsymbol{\nabla}\mathbf{Q}$, keeping the lowest order terms that are allowed by symmetry. The terms containing expansions of $\boldsymbol{Q}$, are called the bulk free energy density $\mathcal{F}_b$, and terms related to derivatives of the nematic tensor are called the elastic free energy $\mathcal{F}_e$ [48]. The bulk free energy can be written as

$$\mathcal{F}_b = \frac{\mathcal{A}}{2} tr(\boldsymbol{Q}^2) - \frac{\mathcal{B}}{3} tr(\boldsymbol{Q}^3) + \frac{\mathcal{C}}{4} (tr(\boldsymbol{Q}^2))^2, \tag{2.2}$$

with $\mathcal{A}, \mathcal{B} \geq 0$ and $\mathcal{C}$ called Landau-de Gennes coefficients.

Minimising the free energy introduced in **Eq. 2.2**, one can find the magnitude of the order parameter associated with the minimum. The trivial solution is $S = 0$. The other solutions to the minimising problem are [48]

$$S_0 = \frac{\mathcal{B}}{6\mathcal{C}} \pm \left((\frac{\mathcal{B}}{3\mathcal{C}})^2 - \frac{8\mathcal{A}}{16\mathcal{C}} \right)^{1/2}. \tag{2.3}$$

Eq. 2.3 shows that, by changing the coefficients $\mathcal{A}, \mathcal{B}$ and $\mathcal{C}$, one can set the isotropic or nematic state as the global ground state of the free energy.

There are a few points that one needs to be careful about when choosing the values of the coefficients. In two dimensions where the transition from the isotropic to the nematic phase is continuous, $tr(\boldsymbol{Q}^3) = 0$, and the second term in Eq. 2.3 vanishes [48, 52]. In addition, the coefficient $\mathcal{C}$ has to be positive, to avoid unbounded growth of the order parameter S.

The elastic free energy, written based on symmetries and by keeping the lowest order derivative term, reads

$$\mathcal{F}_e = \frac{K_Q}{2} \partial_k Q_{ij} \partial_k Q_{ij}, \tag{2.4}$$

where we have used a single Frank elastic constant approximation for bend, splay, and twist deformations. In Appendix A, we introduce a general form of elastic free energy that distinguishes between bend, splay, and twist deformations. In chapter 7, we use this definition to study the growth rate of these deformations due to active flows.

2.1.3 Defects in passive liquid crystals

In liquid crystals, topological defects manifest as localised regions where the alignment of molecules deviates from the surrounding order. These defects are called *topological* as their existence cannot be removed by continuous deformations in the orientation of the liquid crystal around them. Instead, defects represent singular points around which molecular orientation changes in a way that conserves the total number of molecules pointing in a particular direction. As a result, defects can only be created or annihilated in pairs [48].

In a passive liquid crystal, topological defects emerge due to the inherent challenge of aligning molecules across a continuous medium in which orientational order prevails. The presence of topological defects can have profound consequences on the optical properties and mechanical behavior of liquid crystals. Defects scatter light and influence how it interacts with the material, leading to intricate patterns and colours when viewed under polarised light. Moreover, defects can exert mechanical forces on neighboring molecules, giving rise to unique material responses under external stresses [48].

Different types of topological defects arise based on the symmetry of the systems. The lowest defect charge that can be observed in systems with polar symmetry, is equal to ± 1, whereas nematic systems can form defects of charge $\pm 1/2$. As a result, studying the types of defects can shed light on the underlying symmetry of the system. **Fig. 2.2**(a) shows examples of defects that form in liquid crystals in two dimensions.

To calculate the charge associated with defects, one needs to measure how many times the director winds along a circle around the defect. The charge m associated with a defect is defined as

$$m = \frac{1}{2\pi} \oint d\theta, \tag{2.5}$$

where θ shows the director angle with the x axis, $\mathbf{n} = (\cos\theta, \sin\theta)$, and the line integral is taken around the defect core [48].

In two-dimensional liquid crystals, defects form discrete points. In three dimensions, they form disclination lines. In addition, since in three dimensions the director can rotate in 3D, defects have more freedom, and a new type of defect called a twist-type defect, can form in three dimensions. Twist-type defects and three-dimensional disclination lines are shown in **Fig. 2.2**(b) and (c), respectively.

Appendix B explains the process of finding point-like defects and disclination lines in our simulations.

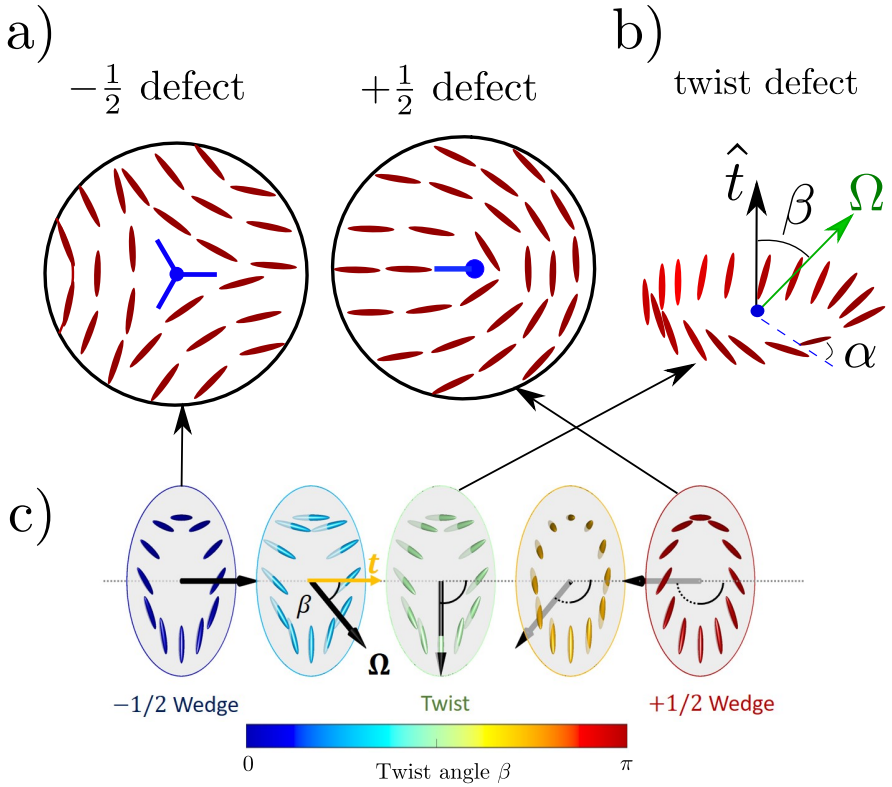

Figure 2.2: The lowest order charge defects allowed in a liquid crystal are the $+1/2$ and $-1/2$ defects. These defects have a lower elastic cost for the system, compared to defects with higher charges. (a) Shows examples of defects in a system with nematic symmetry in two dimensions. (b) Shows an example of a twist-type defect in a system with nematic symmetry in 3D. The blue circle shows the core of the defect, $\hat{t}$ represents the direction along the disclination line, and the blue dashed line connects the center of the twist-type defect to the position with an in-plane director. α is the angle between this line and the local director. The director rotates out of the plane around the rotation vector Ω to form the twist defect. (c) Represents a disclination line in three dimensions. Cross sections perpendicular to a three-dimensional disclination line can form $\pm 1/2$ defects or twist-type defects. (c) is adopted from Ref. [53].

2.2 Nematohydrodynamics

The dynamics of liquid crystals can be studied using the nematohydrodynamic equations. Nematohydrodynamics involves understanding how the orientation and ordering of the elongated molecules, nematogens, within a fluid medium affect the fluid's flow behavior and vice versa. The interactions between the fluid flow and the orientation of nematogens can lead to complex and interesting phenomena, such as flow-induced alignment or reorientation of the nematogens, and changes in the flow properties due to the presence of these ordered structures [54].

In the following subsections, we introduce the nematohydrodynamic equations.

2.2.1 The convection-diffusion equation

The convection-diffusion equation is a partial differential equation that describes the transport of a quantity, such as concentration of a substance or a physical property, in a fluid medium through a combination of convection (advection) and diffusion processes. In a fluid with anisotropic particles, one needs to take into account the asymmetry in the orientation of the particles, and the change in the orientation of the particles due to flows.

The dynamics of the nematic order parameter due to fluid velocity $\mathbf{u}$, and due to interaction between liquid crystal units can be described by the Beris-Edwards equation [54],

$$(\partial_t + \mathbf{u} \cdot \boldsymbol{\nabla})\, \boldsymbol{Q} - \boldsymbol{S} = \Gamma \boldsymbol{H}. \tag{2.6}$$

Here, Γ is a rotational diffusivity, $\boldsymbol{S}$ is the co-rotational advection term, and $\boldsymbol{H}$ is the molecular field.

The co-rotational advection term describes the rotation of the elongated particles due to gradients in the fluid velocity $\boldsymbol{\nabla}\mathbf{u}$. Velocity gradients can be divided into symmetric and anti-symmetric parts. The symmetric part of the velocity gradient is called the strain rate tensor and is defined as

$$\boldsymbol{E} = (\boldsymbol{\nabla}\mathbf{u}^T + \boldsymbol{\nabla}\mathbf{u})/2. \tag{2.7}$$

The anti-symmetric part of the flow gradient is called the vorticity tensor and is defined as

$$\boldsymbol{\Omega} = (\boldsymbol{\nabla}\mathbf{u}^T - \boldsymbol{\nabla}\mathbf{u})/2. \tag{2.8}$$

Using the definition of the strain rate and vorticity, the co-rotational advection term is written as

$$\boldsymbol{S} = (\lambda \boldsymbol{E} + \boldsymbol{\Omega}) \cdot \left(\boldsymbol{Q} + \frac{\boldsymbol{I}}{d}\right) + \left(\boldsymbol{Q} + \frac{\boldsymbol{I}}{d}\right) \cdot (\lambda \boldsymbol{E} - \boldsymbol{\Omega}) - (d-1)\lambda \left(\boldsymbol{Q} + \frac{\boldsymbol{I}}{d}\right) \mathrm{tr}\,(\boldsymbol{Q} \cdot \boldsymbol{\nabla}\mathbf{u}), \tag{2.9}$$

where d is the spatial dimension, and λ is the flow-aligning parameter [55]. The flow-aligning parameter describes the alignment behavior of liquid crystals within a flowing fluid. It is a measure of how the molecules within the liquid crystal tend to align or orient themselves in response to the strain rate. Depending on the respective magnitude of the nematic order S, and the flow-aligning parameter λ, a liquid crystal can be in a flow-aligning or a flow-tumbling regime. If $|\lambda| > 9S/(3S+4)$, the liquid crystal is in a flow-aligning regime and aligns at a certain angle to the principal axis of flow deformation. If the inequality is not satisfied, the director continuously tumbles in shear flows [56, 57].

In addition to flows, the orientation of the particles and the magnitude of the nematic order also change due to the free energy. This is captured in the molecular field

$$\boldsymbol{H} = -(\frac{\delta \mathcal{F}}{\delta \boldsymbol{Q}} - \frac{\boldsymbol{I}}{d}\,\mathrm{Tr}\frac{\delta \mathcal{F}}{\delta \boldsymbol{Q}}), \tag{2.10}$$

that relaxes the nematic tensor to the ground state of the free energy in **Eq. 2.2** and **Eq. 2.4**.

2.2.2 The Navier-Stokes equations

To be able to close the set of the equations, one needs to consider the dynamics of the mass ρ and momentum $\rho\mathbf{u}$, which is given by the Navier-Stokes equations [55]. For a liquid crystal, the Navier-Stokes equations can be written as

$$\frac{\partial \rho}{\partial t} + \boldsymbol{\nabla} \cdot (\rho \mathbf{u}) = 0, \tag{2.11}$$

$$\rho \left(\partial_t + \mathbf{u} \cdot \boldsymbol{\nabla}\right) \mathbf{u} = \boldsymbol{\nabla} \cdot \boldsymbol{\Pi} - \gamma \mathbf{u}, \tag{2.12}$$

where $\boldsymbol{\Pi}$ is a generalised stress tensor that includes a viscous stress $\boldsymbol{\Pi}_{\mathrm{Visc}} = 2\eta \boldsymbol{E}$, and an elastic stress due to the reorientations of the liquid crystal

$$\begin{aligned}\boldsymbol{\Pi}_{\mathrm{Elastic}} = &-P\boldsymbol{I} + 2\lambda\left(\boldsymbol{Q} + \frac{\boldsymbol{I}}{3}\right)(\boldsymbol{Q} : \boldsymbol{H}) - \lambda \boldsymbol{H} \cdot \left(\boldsymbol{Q} + \frac{\boldsymbol{I}}{3}\right) - \lambda\left(\boldsymbol{Q} + \frac{\boldsymbol{I}}{3}\right) \cdot \boldsymbol{H} \\ &- \boldsymbol{\nabla Q} : \frac{\delta \mathcal{F}}{\delta \boldsymbol{\nabla Q}} + \boldsymbol{Q} \cdot \boldsymbol{H} - \boldsymbol{H} \cdot \boldsymbol{Q},\end{aligned} \tag{2.13}$$

where P denotes pressure. The stress tensor $\mathbf{\Pi}$ may also contain terms due to concentration differences $\mathbf{\Pi}_{\boldsymbol{\phi}}$ and an active stress $\mathbf{\Pi}_{\boldsymbol{a}}$, which will be introduced in subsection 2.2.3 and 2.3.1, respectively.

Eq. 2.12 takes into account frictional damping with the substrate through a friction coefficient γ. This is particularly important in systems in two dimensions where the liquid crystal, or the active units are in contact with a substrate, and friction leads to momentum dissipation.

2.2.3 The Cahn-Hillard equation

To study the behavior of living systems in a droplet, one needs to account for the dynamics of the concentration of the active material. A two-phase description in which an active liquid crystal coexists with an isotropic liquid can be helpful in this setting.

In the two-phase system, the isotropic phase retains the characteristics of a conventional liquid, with molecules displaying no preferential alignment ($S = 0$) and activity. Contrastingly, the anisotropic liquid crystalline phase is characterised by the alignment of molecules ($S \neq 0$), and with a non-zero activity. The models that describe the behaviour of two phases, use a phase-field parameter ϕ to account for the concentration of the active phase. The dynamics of the phase field is governed by flows, free energy that leads to the phase separation of the active ($\phi = 1$) and passive ($\phi = 0$) liquids, and a term to penalise shape changes at the interface of the droplet. The free energy of the phase field model reads

$$\mathcal{F} = \mathcal{F}_A + \mathcal{F}_K = \frac{A}{2}\phi^2(1-\phi)^2 + \frac{K_\phi}{2}(\boldsymbol{\nabla}\phi)^2, \tag{2.14}$$

where $A > 0$ is the phase separation coefficint, and $K_\phi > 0$ is the surface tension coefficient [58]. This free energy allows for the smooth variation of the concentration at the droplet interface.

To study the behaviour of an active droplet in a nematic phase inside an isotropic liquid, one can modify the bulk free energy $\mathcal{F}_b$ to lead to a nematic phase with $S = S_0$

inside the active material, and to an isotropic phase outside the active material. This can be achieved by substituting the bulk free energy introduced in **Eq. 2.2** with

$$\mathcal{F}_b = \frac{\mathcal{A}'}{2}(S_0^2\phi - \boldsymbol{Q}:\boldsymbol{Q}/2)^2. \tag{2.15}$$

For positive values of $\mathcal{A}'$, this guarantees that the magnitude of the order is equal to zero in regions with zero concentration of the active material $\phi = 0$, and non-zero in regions where the active material exists $\phi = 1$. For regions with $\phi = 0$ the nematic free energy is at the critical point of the 2d isotropic-nematic transition.

The dynamics of the concentration is governed by the Cahn-Hilliard equation. The Cahn-Hilliard equation is a partial differential equation that describes the evolution of phase separation and microstructure formation in a binary fluid [58].

The dynamics of the concentration reads

$$\partial_t\phi + \boldsymbol{\nabla}\cdot(\mathbf{u}\phi) \quad = \quad \Gamma_\phi\nabla^2\mu, \tag{2.16}$$

where $\mu = \frac{\delta\mathcal{F}}{\delta\phi}$ is the chemical potential and Γ_ϕ is a mobility coefficient.

Finally, the stress associated with the droplet concentration imbalances appears in the Navier-Stokes equation, **Eq. 2.12**, as [28]

$$\boldsymbol{\Pi}_{\boldsymbol{\phi}} = (\mathcal{F} - \mu\phi)\boldsymbol{I} - \boldsymbol{\nabla}\phi\left(\frac{\delta\mathcal{F}}{\delta\boldsymbol{\nabla}\phi}\right). \tag{2.17}$$

The Cahn-Hilliard equation describes how concentration gradients drive diffusion, causing phase separation to occur, while higher-order derivatives penalise interfaces with high curvature, preventing the formation of extremely fine structures. The equation can result in the formation of complex patterns and microstructures as the components separate and create distinct regions [28, 59–61]. In this thesis, we use the Cahn-Hilliard equation to study the behaviour of active droplets, and we do not study the process of phase separation.

2.2.4 Implementation of the model

The equations of nematohydrodynamics are solved using a hybrid lattice Boltzmann and finite difference method [55, 62–64]. The Navier-Stokes equations, **Eq. 2.11** and **Eq. 2.12**, are solved with a lattice Boltzmann scheme.

The lattice Boltzmann method is a numerical approach widely used to simulate fluid flow. The Boltzmann equation uses a microscopic description of a fluid, elucidating how the density and velocity distributions of particles change over time because of interparticle collisions. This approach is different from the Navier-Stokes approach as it describes dynamics of particle distributions instead of a macroscopic velocity field $\mathbf{u}$. However, the Navier-Stokes equations can be deduced from the Boltzmann equation under specific conditions, such as the assumption of local thermodynamic equilibrium. The lattice Boltzmann method has been proven successful in capturing many features of active systems such as phase separation [65], spontaneous flow transition [66] and active turbulence [67].

The lattice Boltzmann method operates by solving for the distribution of particles with various velocities on a discrete lattice. In this thesis we use a D3Q15 (D2Q9) grid to study the behaviour of active nematics in three (two) spacial dimenstion. In the D3Q15 (D2Q9) grid, 15 (9) discretised velocity vectors are assigned to each grid.

These functions evolve according to discrete collision and streaming processes. One can then model macroscopic phenomena such as fluid dynamics by establishing a connection between microscopic distribution functions and macroscopic parameters like density, velocity, and temperature.

In this thesis, we use the simplest collision operator that can be used for Navier-Stokes simulations, which is the Bhatnagar-Gross-Krook (BGK) collision operator [55, 68]. This is now well documented, and the details can be found in Refs. [66, 68, 69].

The convection-diffusion and Cahn-Hillard equations, **Eq. 2.6** and **Eq. 2.16**, are solved using an RK4 iteration scheme [55, 62, 69–72]. The time and spatial grid sizes are set to one.

2.3 Active nematohydrodynamics

Since we are interested in the dynamics of living systems, we study the dynamics of liquid crystals in which nematogens exert forces on their surrounding liquid.

As a result, we need to take into account active stress due to the activity of the suspended particles.

In this section, we introduce the active stress appropriate for describing living systems at the microscale. As a result of this active stress, active liquid crystals form collective patterns of flow, and director orientations that are reminiscent of the flows and orientation of living systems such as bacteria and living tissues. This section also helps us understand the emergence of active flows in two different regimes: (a) a regime in which there is no thermodynamic order without activity, and (b) a regime in which the liquid crystal forms a nematic order in the absence of activity.

2.3.1 Active stress

It is known that, in a low Reynolds number regime, the leading order term in the active force that units can exert on their surroundings is a force dipole [21]. This is because, in a low Reynolds number regime, the net force that a swimmer exerts on its surrounding fluid has to be zero. In a continuum description, one can derive the active stress from coarse-graining the forces that units exert on their surrounding. This was done in Refs. [73, 74], and it was shown that such force dipoles lead to an active stress proportional to the nematic tensor $\mathbf{\Pi}_a = -\zeta\mathbf{Q}$. The proportionality constant ζ depends on the details of the forces that units exert on their surrounding, and can have a positive or a negative sign. If the forces in the force dipole point away from each other, active units are called pushers, and active suspension is called extensile ($\zeta > 0$). In the other case where the force dipoles associated with the units point inwards, the active units are called pullers, and suspension is called contractile ($\zeta < 0$).

Both extensile and contractile systems exist in nature. Most bacterial systems and suspensions of microtubules and kinesin motors are extensile [38, 75]. On the other hand, living cell layers are usually considered to be contractile [26]. We challenge the latter arguments in chapter 6, and show that cell layers can form both extensile and contractile domains.

In subsections 2.3.2 and 2.3.5, we study the instabilities that can arise due to activity in an active nematic that has a nematic and an isotropic passive ground state, respectively. Active instabilities in the nematic phase have been the subject of many previous studies, and as a result, we put more emphasis on the instabilities in the isotropic phase.

2.3.2 Instabilities in the nematic phase

Let us consider an incompressible two-dimensional active suspension and study the stability of the homogeneous nematic phase. We assume that the director is oriented along the x-direction and follow the evolution of small perturbations over time. The elements of the perturbed nematic tensor are $Q_{xx} = Q^0_{xx} + \delta Q_{xx}$ and $Q_{xy} = Q^0_{xy} + \delta Q_{xy}$, where $(Q^0_{xx}, Q^0_{xy}) = (S_0/2, 0)$, and $\delta\mathbf{Q}$ shows the perturbations in the nematic phase. Using **Eqs. 2.6 - 2.13**, and representing the Fourier transform of any fluctuating field δf as $\delta f(\mathbf{r}, t) = \int d\mathbf{q} d\omega\ \tilde{f}(\mathbf{q}, \omega)\, e^{i\mathbf{q}\cdot\mathbf{r}+\omega t}$, the evolution of the perturbations in the low-Reynolds number limit are governed by

$$\begin{aligned}
\omega\tilde{Q}_{xx} &= \tilde{Q}_{xx}\left\{(-K_Q q^2 - 2S_0^2\mathcal{A})\Gamma + (\gamma + \eta q^2)^{-1} M\right\} \\
&\quad + \tilde{Q}_{xy}\left\{\zeta\lambda(1 - S_0^2/2)q^2 \sin 4\theta (4\gamma + 4\eta q^2)^{-1}\right\}, \qquad (2.18)\\
M &= \lambda q^2 (1 - S_0^2/2)\cos^2\theta(\cos 2\theta - 1)[\zeta + 2S_0^2\lambda\mathcal{A}(1 - S_0^2/2)], \\
\omega\tilde{Q}_{xy} &= (\gamma + \eta q^2)^{-1}\tilde{Q}_{xx} q_x q_y (S_0 + \lambda\cos 2\theta)\left\{\zeta + 2S_0^2\lambda\mathcal{A}(1 - S_0^2/2)\right\} \\
&\quad - q^2\tilde{Q}_{xy}\left\{K_Q\Gamma + (S_0 + \lambda\cos 2\theta)\zeta\cos 2\theta(2\gamma + 2\eta q^2)^{-1}\right\}, \qquad (2.19)
\end{aligned}$$

where we have used $\hat{q}\cdot\hat{r} = \cos\theta$. For $\lambda = 0$, these equations simplify to

$$\begin{aligned}
\omega\tilde{Q}_{xx} &= -\tilde{Q}_{xx}(K_Q q^2 + 2S_0^2\mathcal{A})\Gamma, \qquad (2.20)\\
\omega\tilde{Q}_{xy} &= -q^2\tilde{Q}_{xy}\left\{K_Q\Gamma + S_0\zeta\cos 2\theta(2\gamma + 2\eta q^2)^{-1}\right\} \\
&\quad + (2\gamma + 2\eta q^2)^{-1}\tilde{Q}_{xx} q^2 \sin 2\theta S_0\zeta. \qquad (2.21)
\end{aligned}$$

Eq. 2.20 shows that the longitudinal perturbations relax to zero and **Eq. 2.21** gives the growth rate of transverse perturbations $\tilde{Q}_{xy}$ as

$$\omega = -q^2\left\{S_0\zeta\cos 2\theta(2\gamma + 2\eta q^2)^{-1} + K_Q\Gamma\right\}. \qquad (2.22)$$

For $\omega < 0$, perturbations die out over time whereas for $\omega > 0$ perturbations grow, the nematic state is unstable and active turbulence develops. **Eq. 2.22** also confirms that the instability of the ordered state in extensile ($\zeta < 0$) and contractile ($\zeta > 0$) suspensions is caused by bend ($\theta = 0$) and splay ($\theta = \pi/2$) perturbations, respectively. In the limiting case of zero friction, $\gamma = 0$, the growth rate simplifies to the well-known long wavelength hydrodynamic instability of active suspensions [76]. As a result of the growth of the instabilities, the system forms *active turbulence*, a state that exhibits flows with complex spatiotemporal structures, director distortions, and topological defects.

2.3.3 Active defects

In active materials, defects have distinct features compared to their passive counterparts [40, 77]. In active nematics, hydrodynamic instabilities lead to the formation of defects with $\pm 1/2$ topological charge. This is an important feature that can only be observed in active materials, as in passive liquid crystals the elastic attraction between defects with opposite charges leads to defect annihilation, and formation of new pairs of defects can only happen under specific conditions such as sudden changes in the temperature.

Formation of defects in active systems has been observed in both numerical simulations of the nematohydrodynamic equations [40], and in experiments on active microtubule filaments [78], cell layers [26], and bacterial suspensions [79].

As shown in **Fig. 2.2**(a), $+1/2$ defects have polar symmetry which means that they can break time-reversal invariance and, in an active system, can move even in the absence of a background flow. Their direction of motion depends on the details of the stress that they exert on their surroundings and can be towards the head or the tail of the defect [80]. In the continuum models considered so far, $+1/2$ defects have always been found to move toward the head in extensile systems and toward the tail in contractile systems. $-1/2$ defects, by contrast, have three-fold symmetry (**Fig. 2.2**(a)). They produce flows, but since the director field around them does not have a polar symmetry, the flows balance at the center of defects

and do not lead to self-propulsion. Just as in passive nematics $+1/2$ and $-1/2$ pairs tend to annihilate, but in an active system, there is also energy available to create topological defect pairs which then move apart.

In recent experiments, it has been suggested that topological defects can play an important role in many life processes such as cell death and extrusion in epithelial tissues [26], formation of three-dimentional structures in bacterial suspensions [42], and establishing the direction of body formation in *Hydra* [81].

2.3.4 Active turbulence

Many active systems, in their steady state, form active turbulence, a state with complex flow patterns that include both clockwise and counterclockwise vortices with varying strengths [82]. In a steady state, the number of defects is fixed on average, and active particles collectively generate flows and vortices within the fluid medium. The flow field can be caused by defects, or by distortions in the orientation field. These patterns can resemble traditional turbulence in terms of their chaotic and disordered nature, but they are driven by the activity of the individual particles in a regime where viscous stress dominates inertia.

Active turbulence has garnered interest due to its potential to shed light on the principles governing collective behavior and emergent dynamics in active matter systems. It also raises intriguing questions about how such systems can transition to turbulence-like behavior [83] and how this behavior differs from the classical fluid turbulence driven by inertial forces [84].

Research into active turbulence is still a relatively new and evolving area of study. It has implications not only in understanding biological systems but also in the design of new materials [85, 86], propulsion mechanisms [87], and other technological advances inspired by active matter dynamics [88–90].

Since active turbulence includes formation and annihilation of defects, it only appears in systems in which the magnitude of the nematic order is not zero ($S \neq 0$). We discussed in subsection 2.3.2 that activity destabilises the nematic phase and leads to formation of active turbulence. In the following subsection, we show that

activity can induce nematic order, and then active turbulence, even when free energy favours an isotropic phase with $S = 0$. This regime has been the subject of fewer studies compared to the nematic phase, and as such, in the following subsection, we describe this instability in more detail.

2.3.5 Instabilities in the isotropic phase

We showed in **Eq. 2.3** that one can change the bulk free energy parameters to set the isotropic phase as the ground state of the free energy. In this section, we show that active flows destabilise the isotropic phase and lead to the formation of nematic order.

In an isotropic phase, the magnitude of the nematic order is small, and as a result using $\mathbf{Q} \sim 0$, the co-rotational advection term $\boldsymbol{S}$ in **Eq. 2.9** can be approximated by

$$\boldsymbol{S} \approx 2\lambda \frac{\boldsymbol{E}}{d}. \tag{2.23}$$

Using the nematohydrodynamic equations, Eqs. 2.6 - 2.13, along with the simplified co-rotational advection term $\boldsymbol{S}$, we can perform a linear stability analysis to study the stability of the isotropic phase ($S = 0$) with a static fluid, $\mathbf{u} = \mathbf{0}$.

We restrict the perturbation to the magnitude of the order parameter while assuming that the corresponding director field $\mathbf{n}$ is spatially uniform in the domain. The x axis is chosen along the director field and the wave vector $\mathbf{q}$ makes an angle θ with the x axis. Representing the Fourier transform of any fluctuating field δf as $\delta f(\mathbf{r}, t) = \int d\omega \, d\mathbf{q} \, \tilde{f}(\mathbf{q}, \omega) \, e^{i\mathbf{q}\cdot\mathbf{r}+\omega t}$, we can then obtain

$$\rho\omega^2 + q^2(\omega\beta + 2\lambda \cos^2\theta \sin^2\theta(\lambda K_Q q^2 - \zeta) + \Gamma K_Q q^2 \eta) = 0, \tag{2.24}$$

where $\beta = \eta + \rho\Gamma K_Q$. **Eq. 2.24** shows a nonlinear relation between the wavenumber q and the frequency of the perturbations ω. Here, we have retained the inertia term in the dybanics of the vlocity field. This term could lead to formation of stable flocks in suspension of self-propelling swimmers [91]. However, this effect is not important in our nematic system with zero self-propulsion velocity. In addition, in our simulations, since the Reynolds number is small, the inertia term does not play a crutial role in the flow-aligning behaviour. The system is only

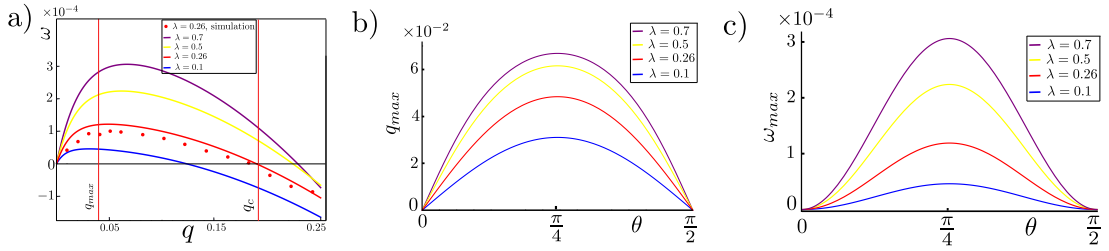

Figure 2.3: (a) Dispersion relation described by **Eq. 2.24** plotted for $\theta = \pi/4$ for different values of the flow-aligning parameter λ. The red data points are obtained for $\lambda = 0.4$ from the numerical simulations of the nematohydrodynamic equations. q_c and q_{max} show the critical wavenumber and the wavenumber associated with the maximum growth rate of perturbations for $\lambda = 0.4$, respectively. Dependence of (b) the most unstable wavenumber q_{max} and (c) the growth rate ω_{max} on the angle θ between the wavevector and the nematic director for various values of the flow-aligning parameter λ.

unstable to long wavelength perturbations when $\lambda\zeta > 0$. The critical wave number below which the instability occurs,

$$q_c = \sqrt{\frac{\lambda\zeta}{2K_Q(2\eta\gamma + \lambda^2)}}, \tag{2.25}$$

is determined by the active length scale $\sqrt{K_Q/\zeta}$, flow-aligning parameter λ, and the ratio of viscosities $\eta\Gamma$, where $1/\Gamma$ is the rotational viscosity of the nematic director. To further investigate the stability of the isotropic state, in **Fig. 2.3**(a) we plot the dispersion relation for various values of the flow-aligning parameter λ. As evident from this figure, $\omega > 0$ for a range of $|\mathbf{q}|$, indicating that the system is linearly unstable. Furthermore, the most unstable wavenumber $q_{\max}$, corresponding to the fastest growth of the perturbations, increases with increasing the flow-aligning parameter indicating that stronger shear alignment drives smaller wavelengths unstable.

Fig. 2.3(b) shows the variation of the most unstable wavenumber $q_{\max}$ and the corresponding growth rate $\omega_{\max}$ as a function of the angle between the wavevector and the director field θ. When θ approaches 0 or $\frac{\pi}{2}$ both $q_{\max}$ and $\omega_{\max}$ drop to zero indicating that there is no nematic order development along or perpendicular to the director.

In order to understand the dependence of the most unstable modes on the alignment parameter and on θ, we next explain the physical mechanism by which

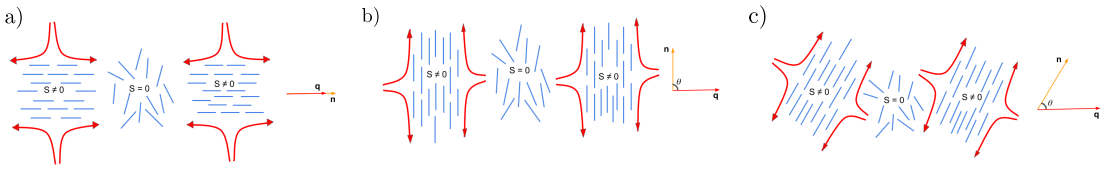

Figure 2.4: Physical mechanism for the growth of nematic order in an isotropic system of active particles. Blue solid lines indicate nematic directors and red arrows denote the activity-induced flows. (a) $\theta = 0$, (b) $\theta = \pi$, (c) $\theta = \pi/4$. In (c) the disordered region at the centre is aligned by the shear flow set up by the neighbouring ordered regions.

activity drives the development of nematic order in an isotropic system.

Fig. 2.3 indicates that the physical mechanism behind the development of the nematic order should involve the response of active particles to the extensional flow field through flow-aligning parameter λ.

A schematic of the physical mechanism involved in the creation of nematic order is shown in **Fig. 2.4**. Each active particle creates a dipolar flow field. The dipole lies along the long axis of the particle, and extensile particles with $\zeta > 0$ pull fluid in from their sides and push it out from their front and back [92]. In a perfectly isotropic arrangement of active particles, the dipolar flows generated by each particle cancel each other on sufficiently large length scales giving rise to no net flow everywhere in the system. However, if a fluctuation generates a local nematic alignment of active particles, then this results in the generation of locally shearing flow fields. In such shear flows particles align further in a manner that enhances this shear flow [93, 94]. This results in the strengthening of the nematic order creating a bootstrap effect: stronger alignment leads to stronger flows that in turn generate stronger alignment. This explains the dependence of the order development on the flow-aligning parameter λ. For larger flow-aligning parameter λ the particles more strongly align with the activity-induced flows, therefore enhancing the bootstrap effect.

Furthermore, the dependence on the angle between the fluctuation wave vector and the nematic director can be explained as follows: If the nematic order is developed parallel or perpendicular to the nematic director (**Fig. 2.4**(a), (b)) - corresponding to $\theta = 0$, and $\theta = \pi/2$, respectively - the resultant extensional

flows cancel each other, producing no shear on the isotropic region. As such, any fluctuation decays and both $q_{\max}$ and $\omega_{\max}$ drop to zero, as evident from **Fig. 2.3**(c) at $\theta = 0,\ \pi/2$. This is in contrast to the instabilities of the nematic phase, **Eq. 2.22**, in which the growth rate of perturbations is maximum for $\theta = 0$ ($\theta = \pi/2$) in extensile (contractile) systems. On the other hand, for any $0 < \theta < \pi/2$, the resultant local activity-induced extensional flows produce a shear flow on the local isotropic regions, inducing further nematic alignment in them.

2.4 Summary

In this chapter, we presented the theoretical framework that we use in the rest of this thesis. We introduced nematic liquid crystals, described the tensor order parameter $\mathbf{Q}$, and introduced topological defects in two and three dimensions.

We then described the continuum nematohydrodynamic equations that evolve the nematic tensor order parameter $\mathbf{Q}$, momentum, and active material concentration ϕ.

Finally, we summarised the mechanism for the instability of the nematic and the isotropic phases of liquid crystals due to active flows. We showed that different types of instabilities appear in these regimes. In a nematic phase, vorticity leads to the growth of bend (splay) perturbations in extensile (contractile) suspensions, and this destabilises the nematic order and leads to formation of defects and active turbulence. In an isotropic phase, however, the strain rate destabilise the isotropic phase by forming nematic order. Since the nematic order is not stable in an active suspension, a secondary instability then leads to the formation of defects and active turbulence.

Life sucks order from a sea of disorder.

James Gleick

3

+1/2 defect ordering in active nematics

Suspensions of microtubules driven by two-headed kinesin motors represent one of the most extensively studied active nematic systems in experiments [38, 95]. This system shares many common features with active nematic theories including formation of bend instabilities, active turbulence, and defect proliferation. In this experimental setup, the microtubules are frequently arranged to create a thin layer between an upper aqueous layer and a lower oil layer. Interestingly, it has been shown that increasing the viscosity of the oil layer leads to a state in which the +1/2 topological defects exhibit nematic alignment while still maintaining their ability to move [38].

Since increasing the viscosity of the oil leads to faster damping of the active flows, this raises the question of whether increasing friction with a substrate in the nematohydrodynamic equations could reproduce the nematic defect ordering observed in the experiments.

Several research papers have considered a *compressible dry system* where friction completely dominates viscous effects and dynamics of the system can be described in terms of a single equation for the nematic tensor $\mathbf{Q}$ [96–99]. These studies show long-range +1/2 defect ordering, but the ordering is *polar* rather than *nematic*. On the other hand, a study on the high friction regime of full nematohydrodynamic equations has found a static lattice of defects in which the +1/2 defects show nematic ordering [100].

In this chapter, we discuss the role of friction in ordering +1/2 defects in active nematics. We show that the type of the ordering of defects, *polar* or *nematic*, depends on the ground state of the free energy, i.e. whether the system is in an isotropic or a nematic phase without activity.

In section 3.1 we study +1/2 defects ordering in a system that forms an isotropic phase without activity, and in a regime with high frictional damping. We show that for two pairs of ±1/2 defects, the defect pair orientation that minimises the free energy depends on the respective position of the defect pairs. In a large system with many defect pairs, this leads to a global nematic ordering of +1/2 defects.

In section 3.2 we study the role of friction in a system that forms a nematic phase without activity. We show analytically that in this regime polar director structures called *arches* are the steady state solution of the nematohydrodynamic equations. The interaction between arches and +1/2 defects leads to polar ordering of +1/2 defects.

3.1 Defect ordering in the isotropic phase

In **Fig. 3.1** we show the results of the simulations of the nematohydrodynamic equations with an isotropic phase as the ground state and with high friction. The figure shows that −1/2 defects intervene between +1/2 defects, forming pairs of ±1/2 defects. The orientation of the pairs depends on their respective position. As an example, the defect pairs highlighted in the green outline have anit-parallel orientation whereas the defect pairs in the orange outline are parallel.

In what follows, we calculate the free energy associated with different configurations of two pairs of $\pm\frac{1}{2}$ defects to find the optimum orientation of the pairs with respect to each other [101].

We first study the case where the vector connecting the center of the pairs $\mathbf{R}_p = R_p\hat{R}_p$ is perpendicular to the direction of the first pair as represented in **Fig. 3.2**(a). We then write the free energy for the case where $\mathbf{R}_p$ is parallel to the direction of the first pair and compare the free energy of these configurations.

Finally, we write the general solution where $\mathbf{R}_p$ has a general orientation and is not parallel or perpendicular to the direction of the first pair.

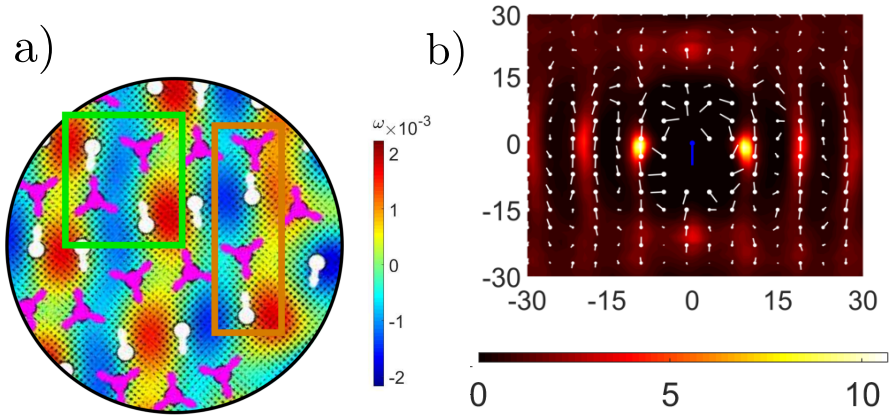

Figure 3.1: Defect ordering in the high friction regime of active nematics with isotropic ground state. a) $+1/2$ ($-1/2$) defects are shown in white (magenta). Depending on the respective position of $\pm 1/2$ defect pairs, the pairs form parallel (green outline) or anti-parallel (orange outline) alignment. The colourmap shows vorticity. b) Average orientation of $+1/2$ defects around a central $+1/2$ defect in a high friction regime. The heatmap is proportional to probability of finding a defect around a central defect.

Let us assume that the first pair is oriented along the y axis and $\mathbf{R}_p$ is along the x axis (**Fig. 3.2**(a)). The elastic free energy of the system is given by:

$$F = \int f d^2r = K \int (|\boldsymbol{\nabla} Q_{xx}|^2 + |\boldsymbol{\nabla} Q_{xy}|^2) d^2r, \tag{3.1}$$

where f is free energy density and K is the Frank elastic constant. To minimise the free energy we need to solve

$$\frac{\delta F}{\delta Q_{xy}} = \frac{\delta F}{\delta Q_{xx}} = 0, \tag{3.2}$$

which can be written as

$$\frac{\delta F}{\delta Q_{ij}} = \frac{\partial f}{\partial Q_{ij}} - \boldsymbol{\nabla} \cdot \frac{\partial f}{\partial \boldsymbol{\nabla} Q_{ij}} = 0. \tag{3.3}$$

Using the free energy density introduced in **Eq. 3.1** we have:

$$\nabla^2 Q_{xx} = \nabla^2 Q_{xy} = 0. \tag{3.4}$$

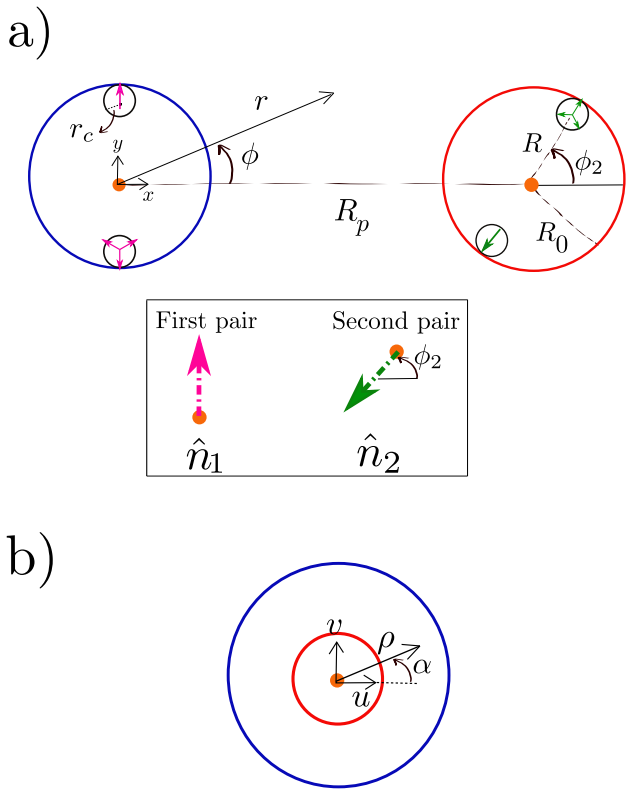

Figure 3.2: a) Two pairs of $\pm 1/2$ defects in the $z = x+iy$ plane. The centers of the pairs, represented by orange dots, are separated by a distance R_p and the distance between $\pm\frac{1}{2}$ defects in each pair is $2R$. b) Using the conformal map introduced in **Eq. 3.8** we map the geometry in the $z = x + iy$ plane to the simpler geometry in the $w = u + iv$ plane.

To find the minimum of the free energy in the presence of the defect pairs, we need to solve **Eq. 3.4** with appropriate boundary conditions on the blue and red circles in **Fig. 3.2**(a). The boundary condition on the first circle is [102]:

$$Q_{xx} = \cos^2\theta(r',\phi') - \frac{1}{2}, \tag{3.5}$$

$$Q_{xy} = \sin\theta(r',\phi')\cos\theta(r',\phi'), \tag{3.6}$$

where $\theta(r',\phi') = [\frac{1}{2}\arctan\frac{r'\cos\phi'}{r_c}]_\pi$. On the second circle, we have

$$\theta(r',\phi') = [\phi_2 + \frac{1}{2}(\arctan\frac{r'\sin\phi' - R\sin\phi_2}{r'\cos\phi' - R_p - R\cos\phi_2} + \arctan\frac{r'\sin\phi' + R\sin\phi_2}{R_p - r'\cos\phi' - R\cos\phi_2})]_\pi, \tag{3.7}$$

where θ shows the angle between the local nematic director and x axis, (r',ϕ') identifies the position on the boundaries and $[]_\pi$ accounts for the fact that θ is only defined modulo π.

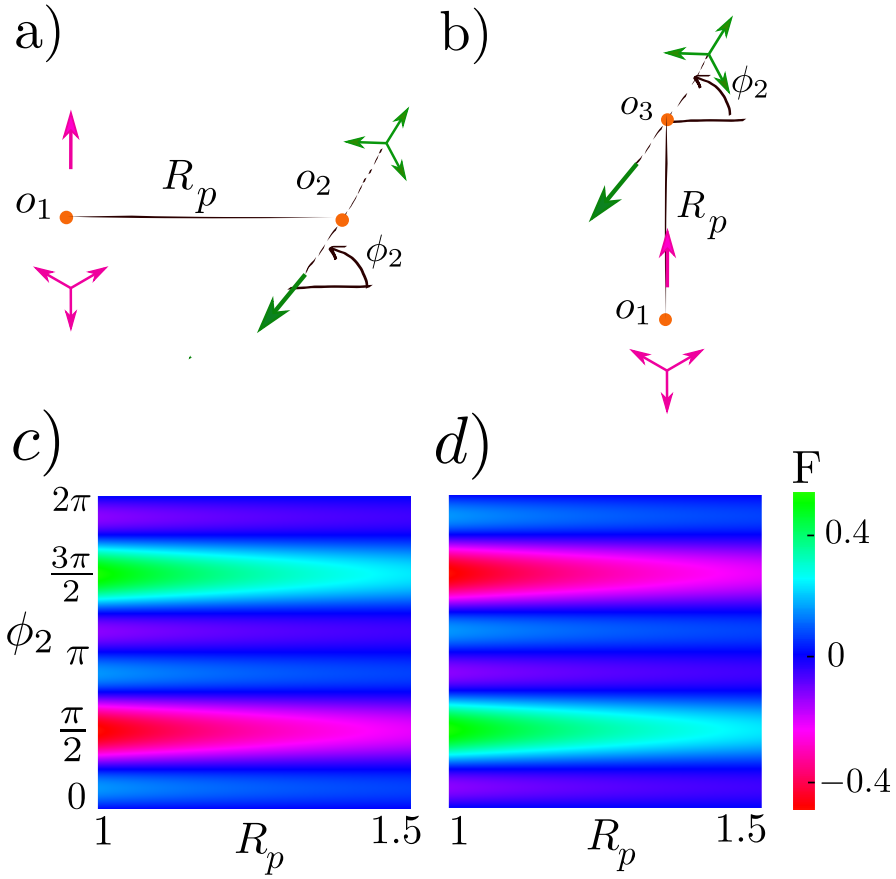

Figure 3.3: a) and b) show two different positions for the second pair. In (a) the vector connecting the two pairs is perpendicular to the direction of the first pair ($\hat{n}_1 \cdot \hat{R}_p = 0$) and in (b) it is parallel to the direction of the first pair ($\mathbf{R}_p \cdot \hat{n}_1 = 1$). c) and d) show the free energy associated with configurations represented in (a) and (b) respectively. For the configuration shown in part (a) of the figure, the free energy is minimum for the antiparallel orientation of the second pair. But for the configuration represented in part (b), the free energy is minimum for the parallel orientation of the second pair. By increasing the distance between the pairs (increasing R_p), the free energy becomes less sensitive with respect to the orientation of the second pair. Here we have used $R_0 = 0.1$ and $K = 10$.

To solve the Laplace equation with the above boundary conditions we use a conformal map from $z = x + iy$ plane to $w = u + iv$ plane in which we need to solve the Laplace equation in a simpler geometry of two concentric circles as represented in **Fig. 3.2**(b). We use the conformal map

$$w = \frac{z - \gamma R_0}{\gamma z - R_0}, \qquad \gamma = \frac{R_p + \sqrt{R_p^2 - 4R_0^2}}{2R_0}, \tag{3.8}$$

which maps the circle in the center to a circle with radius equal to one and maps the second circle to a circle of radius $a = (R_p^2 - 2R_0^2 - R_p\sqrt{R_p^2 - 4R_0^2})(2R_0^2)^{-1} <$

1. In the limit we are interested in ($r_c \ll R_0 \ll R_p$), the boundary condition on the first circle simplifies to

$$\theta(\rho'=1,\alpha') = \begin{cases} 3\pi/4 & -\frac{\pi}{2} < \alpha' < \frac{\pi}{2} \\ \pi/4 & \frac{\pi}{2} < \alpha' < \frac{3\pi}{2} \end{cases} \tag{3.9}$$

and on the second circle, we have

$$\theta(\rho'=a,\alpha') = \begin{cases} [3\pi/4+\phi_2]_\pi & \phi_2 < \alpha' < \phi_2+\pi \\ [\pi/4+\phi_2]_\pi & \phi_2-\pi < \alpha' < \phi_2 \end{cases} \tag{3.10}$$

In **Eqs. 3.9** and **3.10** α' is the angle between the vector that connects the center of the circles to their surface and the x-axis.

To solve the Laplace equation in the new geometry, we use the Green function of concentric circles. Knowing the boundary conditions at (ρ',α') on the circles, we use the Green Theorem to find $Q_{ij}(\rho,\alpha)$ in w plane:

$$\begin{aligned} Q_{ij}(\rho,\alpha) &= \frac{-1}{4\pi}\int \partial_{N'} G(\rho,\alpha;\rho',\alpha') Q_{ij}(\rho',\alpha')\rho' d\rho' d\alpha', \\ G(\rho,\alpha;\rho',\alpha') &= \frac{2\ln(\rho_</a)\ \ln(\rho_>)}{\ln(a)} \\ &+ \sum_{m=1}^{\infty} \frac{2}{m}(\frac{\rho_<}{\rho_>})^m \cos(m(\alpha-\alpha'))\frac{(1-(a/\rho_<)^{2m})(1-\rho_>^{2m})}{1-a^{2m}}, \end{aligned} \tag{3.11}$$

where **N** shows normal vector to the boundary of the circle, $\rho_< = \min(\rho,\rho')$ and $\rho_> = \max(\rho,\rho')$. Using **Eq. 3.11** we can find the nematic tensor Q_{ij} in the w plane as

$$\begin{aligned} Q_{xx}(\rho,\alpha) &= \frac{1}{2} + \frac{2(1-2\cos^2(\phi_2+\pi/4))}{\pi}\sum_{m'=0}^{\infty}(\frac{a}{\rho})^{2m'+1}\frac{(1-\rho^{4m'+2})}{(2m'+1)(1-a^{4m'+2})} \times \\ &\sin((2m'+1)(\alpha-\phi_2)), \\ Q_{xy}(\rho,\alpha) &= \sum_{m'=0}^{\infty}\frac{-2}{\pi(2m'+1)(1-a^{4m'+2})}\Bigg(\cos(2\phi_2)(\frac{a}{\rho})^{2m'+1}(1-\rho^{4m'+2}) \times \\ &\sin((2m'+1)(\alpha-\phi_2)) \\ &+(-1)^{m'}\cos((2m'+1)\alpha)\rho^{2m'+1}(1-(\frac{a}{\rho})^{4m'+2})\Bigg). \end{aligned} \tag{3.12}$$

Using **Eq. 3.12** along with **Eq. 3.1**, we then calculate the free energy associated with the alignment interaction between the pair defects:

$$F = \sum_{m'=0}^{\infty}\frac{16\,a^{1+2m'}K}{\pi(1+2m')(1-a^{4m'+2})}\Bigg(a^{1+2m'} + (-1)^{m'}\cos 2\phi_2 \sin((2m'+1)\phi_2)\Bigg). \tag{3.13}$$

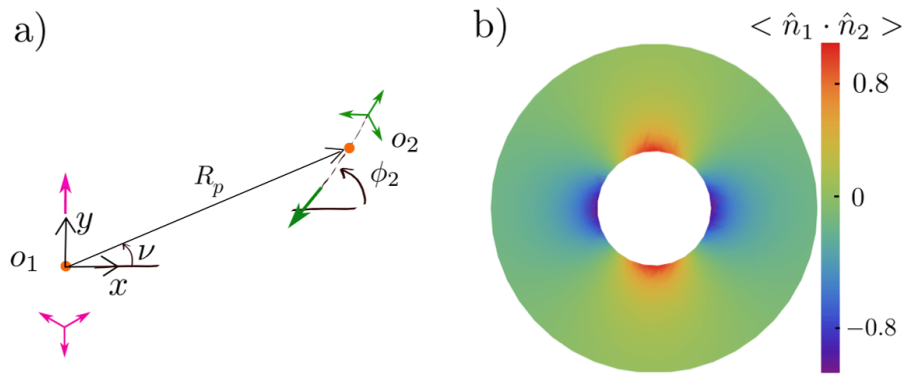

Figure 3.4: a) The general configuration of two defect pairs is represented. The first pair is in the center of the coordinate system and is oriented along $\hat{n}_1 = \hat{y}$. The second pair is positioned in a distance R_p from the first pair and is oriented along $\hat{n}_2 = (-\cos\phi_2, -\sin\phi_2)$. b) The value of $\langle \hat{n}_1 \cdot \hat{n}_2 \rangle$ is shown for different positions of the second pair in a polar plot. In the polar plot, the distance from the center shows the value of the R_p and the polar angle represents ν. For $\nu = 0$ and π (blue regions) $\langle \hat{n}_1 \cdot \hat{n}_2 \rangle$ is negative which means anti-parallel orientation is favoured. However, for $\nu = \pm\pi/2$ (red region) $\langle \hat{n}_1 \cdot \hat{n}_2 \rangle$ is positive which shows that parallel orientation is dominant.

To understand this, in **Fig. 3.3**(c) we plot the free energy F as a function of the distance between defect pairs R_p and the angle ϕ_2 which specifies the orientation of the second pair. The heatmap shows that the free energy is minimum when the second pair orients antiparallel to the first pair. This is in agreement with the result of the simulations (**Fig. 3.1** (a) and (b)).

Using the same method for the case in which $\mathbf{R}_p$ is along the y axis (shown in **Fig. 3.3**(b)), we find the free energy as:

$$F = \sum_{m'=0}^{\infty} \frac{16\, a^{1+2m'} K}{\pi(1+2m')(1-a^{4m'+2})} \left(a^{1+2m'} - (-1)^{m'} \cos 2\phi_2 \sin((2m'+1)\phi_2) \right). \tag{3.14}$$

This is presented in **Fig. 3.3**(d), and shows that the free energy is minimum when the second pair orients parallel to the first pair, in agreement with the result of the simulations (**Fig. 3.1** (a) and (b)).

Finally, using the same approach, we can find the free energy for the general configuration shown in **Fig. 3.4**(a). This reads

$$F(\nu, \phi_2, R_p) = \sum_{m'=0}^{\infty} \frac{16\, a^{1+2m'} K}{\pi(1+2m')(1-a^{4m'+2})} \left(a^{1+2m'} + (-1)^{m'} \cos 2\phi_2 \right. \tag{3.15}$$

$$\left. \times \sin((2m'+1)(\phi_2 - 2\nu)) \right). \tag{3.16}$$

Since $a \ll 1$, we can approximate the free energy as

$$F(\nu, \phi_2, R_p) \approx \kappa \cos 2\phi_2 \sin(\phi_2 - 2\nu), \tag{3.17}$$

where $\kappa = 16\, aK/(\pi(1-a^2))$. Using **Eq. 3.17** we then define $\langle \hat{n}_1 \cdot \hat{n}_2 \rangle$ to find the average direction of the second pair with respect to the first pair in different positions in space:

$$\langle \hat{n}_1 \cdot \hat{n}_2 \rangle (R_p, \nu) \;\; = \;\; -\int_0^{2\pi} \sin\phi_2 e^{-\beta F(\nu, \phi_2, R_p)} d\phi_2, \tag{3.18}$$

where we have used the Boltzmann Weighted average with the Boltzmann factor $e^{-\beta F(\nu,\phi_2,R_p)}$, and we have defined $\beta = 1/(k_B T)$.

Using **Eq. 3.18**, we have plotted the average projection of the orientation of the second pair along the first pair as a heatmap in **Fig. 3.4**(b). The heatmap shows that parallel orientation of the pairs is formed when the second pair is located along the symmetry axis of the first pair, and anti-parallel orientation when the second pair is located side-by-side to the first pair.

3.2 +1/2 defect ordering in active nematics with a nematic ground state

In this section, we study the behaviour of the active nematohydrodynamic equations in a nematic phase with high friction. Our simulations show that as the friction is increased, the system develops a memory and, the motion of +1/2 defects leaves persistent arches in the director field (**Fig. 3.5**(a)). As represented in **Fig. 3.5**(b), for an extensile +1/2 defect moving in the direction of the red arrow, the arch comprises a splay distortion along the trajectory of the defect (shown in yellow) with two neighbouring regions of bend distortion (shown in green) parallel to the trajectory. At lower values of the friction, the arches stay in the system just for a short while since the passage of defects that move in different directions destroys them. As the friction is increased to intermediate values, the distortions left by the defects extend in space and persist for longer times. These arches have been observed in agent-based simulations of active rods and self-propelling

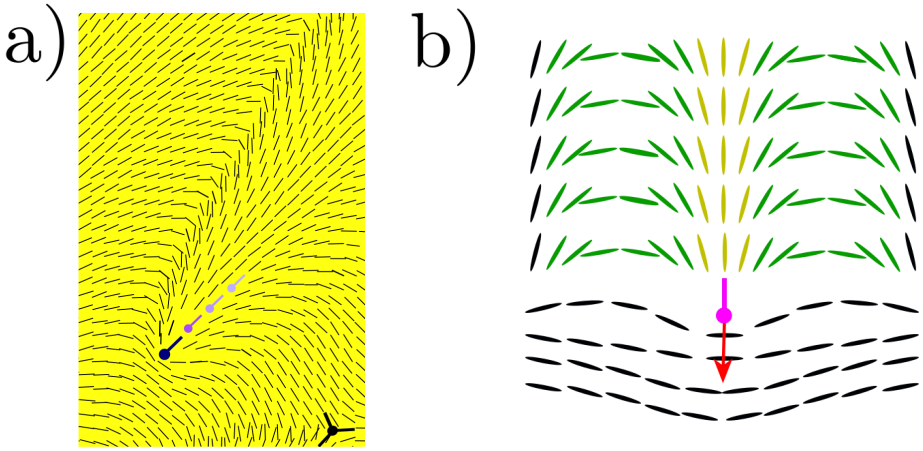

Figure 3.5: a) Arch formation in a high friction regime of the nematohydrodynamic equations with extensile activity. The trajectory of the +1/2 defect is represented by the small light blue defects. b) The arch left by an extensile +1/2 defect (shown in purple) at high friction, incorporates bend and splay distortions represented by green and yellow directors, respectively.

particles without hydrodynamic flows [103, 104], and in continuum models in regimes where viscosity is slaved to friction [97, 99]. In our simulations, the arch patterns lead to the reorientation of newly formed +1/2 defects and align them with the arch polar axis (**Fig. 3.7**(f)).

To understand the formation of the arches in the simulations, we assume that the emerging structures are invariant in the y direction and that the friction force dominates the viscous force. We also set $\lambda = 0$ since deep in the ordered phase, where $S \approx 1$, the system is in the flow-tumbling regime. Eqs. 2.12 and 2.13 can then be solved for an incompressible system in the low-Reynolds number regime to give the pressure and velocity fields

$$P = c_1 y - \frac{\zeta}{\gamma} Q_{xx}, \tag{3.19}$$

$$u_y = \frac{\zeta}{\gamma} \partial_x Q_{xy} + c_1, \quad u_x = 0. \tag{3.20}$$

Since the system is invariant in the y direction, $c_1 = 0$. Assuming that the magnitude of the nematic order is constant in space, we use **Eq. 3.20** together with **Eq. 2.6** to find the evolution of the orientation field:

$$\partial_t \theta(x,t) = \frac{\zeta S_0}{4\gamma} \partial_x^2 \sin 2\theta(x,t) + \Gamma K \partial_x^2 \theta(x,t). \tag{3.21}$$

For zero activity ($\zeta = 0$), the steady state solution of **Eq. 3.21** satisfies $\Gamma K d_x^2 \theta(x) = 0$. Therefore, for periodic boundary conditions on a box of size L so that $\mathbf{Q}(x = 0) = \mathbf{Q}(x = L)$,

$$\theta(x) = \frac{m\pi}{L} x + \pi/2, \quad m \in \text{integers}. \tag{3.22}$$

These solutions, which minimise the elastic free energy, correspond to m arches of equal width. The global minimum is $m = 0$, the nematic state, and arch solutions with $m \neq 0$, are local minima. As such, they can be observed in systems with small noise but will be destabilised by larger values of the noise.

In the presence of activity, and assuming the same boundary conditions, the steady-state director field satisfies

$$\frac{\zeta S_0}{2K\Gamma\gamma} \sin 2\theta(x) + \theta(x) = \frac{m\pi x}{L} + \frac{\pi}{2}. \tag{3.23}$$

Eq. 3.23 does not have an analytic solution, but for $|\zeta S_0| < 2K\gamma\Gamma$ it has real solutions that can be found numerically. In particular, compared to passive arches, in extensile (contractile) systems arches have larger bend (splay) deformations (see **Fig. 3.6**(a) and (b)).

Having in hand the director field, we can use **Eq. 3.20** to find the velocity field on arches. In **Fig. 3.6**(c) we compare the solution for $\bar{u}_y = u_y \ell^* / (\gamma K)$ from **Eq. 3.20**, where ℓ^* is the arch width, with the flow field of arches obtained from the numerical solution of the full nematohydrodynamic equations, showing good agreement. In finding the analytical solution of the flow field we ignored viscous forces compared to the friction force at large friction and therefore would not expect exact agreement between the analytical solution and the solution from solving the full nematohydrodynamic equations. The maximum velocity points along the polar axis of arches in both contractile and extensile systems [105]. This flow, along with the elastic interaction between arches and +1/2 defects aligns the defects with arches and leads to polar defect ordering.

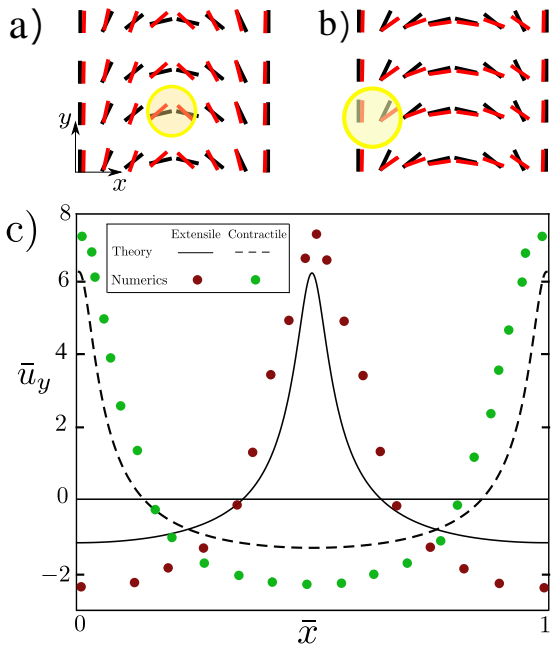

Figure 3.6: Arches: Comparison of the director configuration of arches at zero activity (black) and finite activity (red) in (a) extensile and (b) contractile systems. The yellow circles show that extensile (contractile) activity increases bend (splay) deformations in arches. c) A comparison of the analytical solutions for the velocity field around arches **Eq. 3.20** with the numerical solution of the full nematohydroynamic equations. The maximum velocity corresponds to the bend (splay) region of the arches in extensile (contractile) systems and points parallel to the polar axis of the arches in both cases.

3.3 Summary

In the previous chapter, we showed that active systems in nematic and isotropic phases form active turbulence through different mechanisms. Here, we showed that increasing friction in these two limits leads to the formation of different defect ordering [101, 105–107]. We found that, in a system with an isotropic ground state, increasing friction decreases active flows, and the elastic interaction between defects leads to the formation of the nematic ordering of defects. On the other hand, in a system that forms a nematic phase without activity, increasing friction introduces a steady state with polar symmetry in the configuration of the nematogens (arches), and the defects form polar ordering due to active and elastic interaction with these structures. These results are summarised in **Fig. 3.7**.

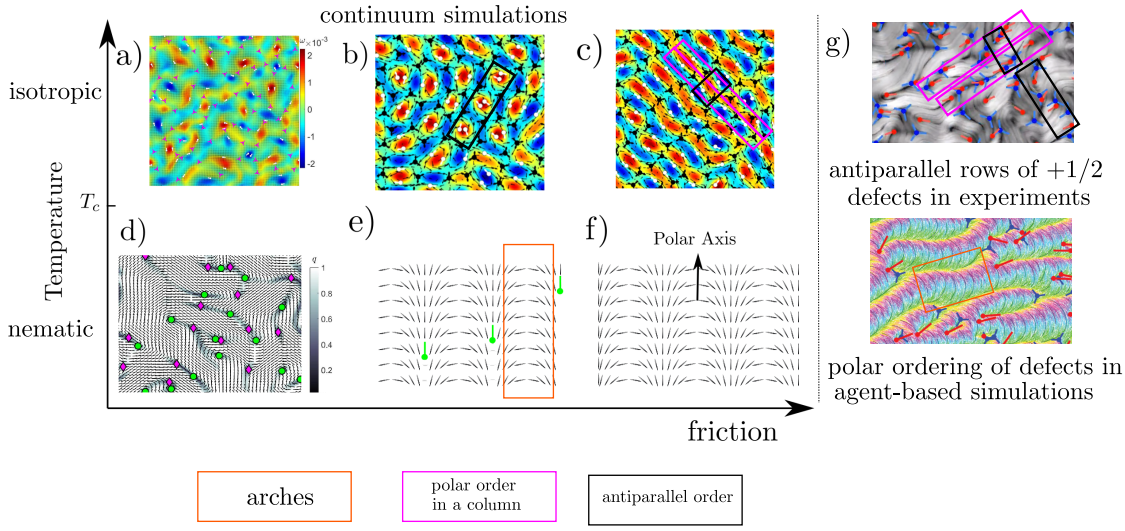

Figure 3.7: Crossover from wet to dry active nematics in the isotropic and nematic phase. (a) In a system that is in an isotropic phase without activity (high temperature, $T > T_c$), activity leads to formation of nematic order and active turbulence. (b) Increasing friction in the isotropic phase leads to the formation of a motile lattice of defects. In this regime, a rectangular lattice formed by $+1/2$ defects coexists with a hexagonal lattice formed by $-1/2$ defects. (c) Increasing friction even further, the rectangular lattice wins the competition. In the rectangular lattice, $+1/2$ defects represent polar order in one direction and nematic order in another direction [101]. In (a)-(c), the background color shows the vorticity field, and $+1/2(-1/2)$ defects are represented in white (magenta). (d) Represents active turbulence in the nematic phase ($T < T_c$), caused by long-range hydrodynamic instabilities of the nematic state. (e) In this regime, by increasing friction, the system obtains a memory and keeps the arch patterns left on $+1/2$ defects trails. The arches align motile $+1/2$ defects with them and lead to formation of polar ordering of defects. (f) At very high values of friction, the arch state "coexists" with the nematic phase [104, 105]. In (d)-(f) grey shows the director field, and $+1/2$ $(-1/2)$ defects are shown in green (magenta). g) Top: In agreement with our free energy minimisation and simulations in the isotropic phase ($T > T_c$), the formation of columns of $+1/2$ defects with polar ordering has been observed in experiments (magenta outline). Defects in adjacent columns have antiparallel ordering (black outline). Bottom: Agent-based simulations of growing rods in a nematic phase ($T > T_c$) show arches (orange outline) and polar ordering of $+1/2$ defects. This is in agreement with our continuum simulations with a nematic ground state.

If you don't like bacteria, you're on the wrong planet.

Stewart Brand

4

Geometrical control of interface patterning underlies active matter invasion

4.1 Introduction

Interaction between active materials and the boundaries of geometrical confinement is key to many emergent phenomena in active systems. For living active matter consisting of animal cells or motile bacteria, the confinement boundary is often a deformable interface, and it has been unclear how activity-induced interface dynamics might lead to morphogenesis and pattern formation. In this chapter, we use numerical simulations of the nematohydrodynamic equations to understand the morphological pattern that emerges at the interface of bacterial droplets. These patterns are characterised by periodically-spaced interfacial protrusions; behind the interfacial protrusions, bacterial swimmers self-organise into multicellular clusters displaying $+1/2$ nematic defects.

We show that to be able to understand these patterns, one needs to modify the nematohydrodynamic equations to account for the fact that in the experiments, the magnitude of the nematic order decreases towards the center of the droplet. We do this by considering a dynamical equation for the magnitude of the nematic

order that sets the ground state of the bulk free energy. This enables us to understand the director patterns, velocity patterns, and the fractal-type patterns that form in the experiments [79].

In agreement with the experiments, we find that this interface patterning is geometrically controlled by the local curvature of the interface, a phenomenon we denote as collective curvature sensing. Using our model, we reveal that collective curvature sensing arises from enhanced active stresses near high-curvature regions, with the active length scale setting the characteristic distance between the interfacial protrusions.

In section 4.2 we describe the experimental observations and the patterns that form in the experiments. In section 4.3 we introduce our model, which is a modification of the nematohydrodynamic equations to account for the features observed in the experiment. In section 4.4 we present the results of the simulations, and in section 4.5 we discuss the results and applications.

4.2 Experimental observations

The experiments we introduce in this section are performed by Haoran Xu, under the supervision of Yilin Wu in The Chinese University of Hong Kong. The experimental system is a quasi-2D circular drop containing a suspension of *Proteus mirabilis* grown on an agar substrate. *P. mirabilis* is a rod-shaped bacterium ($\sim$4 μm in length and 0.8 μm in width), widely distributed in the natural environment [108]. In the experiments, initially, the interface between the active drop and the cell-free space is smooth. As time evolves, the interface gradually deforms, and the active drop develops an ordered morphological pattern at the interface (**Fig. 4.1**(a) and (b)). This is characterised by periodically-spaced protrusions along the interface, with an inter-protrusion separation of 65$\pm$9 μm (**Fig. 4.1**(c)). Behind the interfacial protrusions, bacterial swimmers self-organise into multicellular clusters, commensurate with the protrusions. The orientation field of cells in each cluster displays a +1/2 nematic defect with the polarity vector pointing perpendicular to the interface and towards the colony center (**Fig. 4.1**(b)). Meanwhile, the collective

velocity field of cells adjacent to the interface self-organises into a vortex lattice, with neighboring domains of opposite vorticity (**Fig. 4.1**(b), lower). The vortices are primarily extended perpendicular to the interface, and the domain size is, on average, half of the inter-protrusion separation (**Fig. 4.1**(b), lower).

To examine whether the interface morphological pattern and bacterial self-organisation is driven by bacterial motility, the experimentalists optically deactivate the flagellar motility of cells at the invasion interface. During motility deactivation, the interfacial protrusions gradually smoothes out and cells near the edge become aligned parallel to the interface. Meanwhile, all the multicellular clusters as well as the vortex structure of the cellular collective velocity field near the interface disappear. After activating the flagellar motility again, cell motility recovers and the interfacial protrusions re-emerge. As the growth of most cells in the active drop is not affected during motility deactivation (note that only cells at the edge are deactivated), this observation shows that active stress due to flagellar motility is necessary to form the interface morphological pattern and cellular self-organisation, while the effect of cell mass growth alone cannot account for the phenomenon [109–112]. On the other hand, bacterial suspension drops consisting of cells that are washed and deposited on fresh substrates develop the same interfacial morphology; this fact rules out the contribution of Marangoni instability [113], chemotaxis [109], or intercellular chemical signaling [114] to the phenomena.

4.2.1 Hierarchical transition from interfacial protrusions to creeping branches

In the experiments, after the emergence of the interfacial pattern, some protrusions of the active suspension drop start to expand continuously at a speed of several $\mu m/\mathrm{s}$ (up to $\sim 10\mu m/\mathrm{s}$) in the form of creeping branches (**Fig. 4.2**(a)). The first creeping branches later undergo the same protrusion-to-branch transition process (**Fig. 4.2**(a)): Protrusions develop at the interface between the creeping branches and the open space, and some of these protrusions break out as secondary creeping branches. The secondary creeping branches again repeat this process to give rise

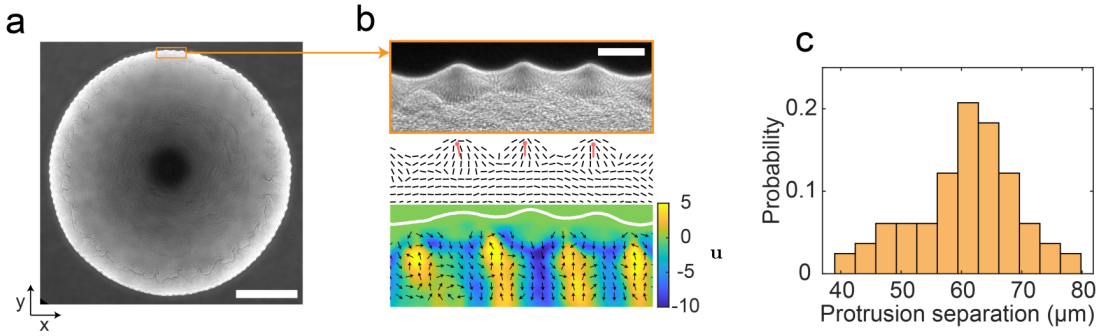

Figure 4.1: Ordered interfacial protrusions and bacterial self-organization near an active fluid interface. (a) Representative phase-contrast image of a P. mirabilis active suspension drop with ordered interfacial protrusions. The droplet is nearly two-dimensional, with its height reaching $10\mu m$ at the center. Scale bar, 500 μm. (b) Upper: enlarged view of the box in panel a. Middle: orientation field of cells in the upper panel. Red marks represent the direction of $+1/2$ defects, with the dot indicating the defect core. Lower: colourmap showing the averaged velocity field at the region shown in the upper panel. Arrows in the figure represent velocity direction while the colourmap at the right indicates the radial velocity component (unit: μm/s). A positive value indicates moving outwards toward the interface while a negative value indicates moving inwards away from the interface. Scale bar, 50 μm. (c) Distribution of the nearest separation of interfacial protrusions.

to new creeping branches at the next level. The protrusion-to-branch transition continues recursively in a hierarchical manner, with the creeping branches at all levels of hierarchy having a conserved initial width of $\sim 20-30\mu m$ (**Fig. 4.2**(a)). Interestingly, the width of protrusions ($\sim 20-30$ μm; defined as the full width at half maximum of the protrusion profile) is comparable to the initial branch width and also conserved across all levels of hierarchal creeping branches (see **Fig. 4.1**(b), **Fig. 4.2**(a)), even on the last-level branches which have a width of $\sim 20\mu m$. This fact suggests that the protrusion width is controlled by some intrinsic length scale, and the characteristic protrusion width sets the initial or the minimal width of creeping branches. We note that once a creeping branch has formed, cell mass growth can help the formation of higher-level branching by supplying more cell mass and widening the branch widths. Also, two creeping branches colliding with each other would merge into one. Due to branch widening and merging, a general trend is that earlier branches become wider than later ones.

The recursive and hierarchical transition process gives rise to a striking self-similar pattern (**Fig. 4.2**(b)). The fractal-like branching pattern of the active

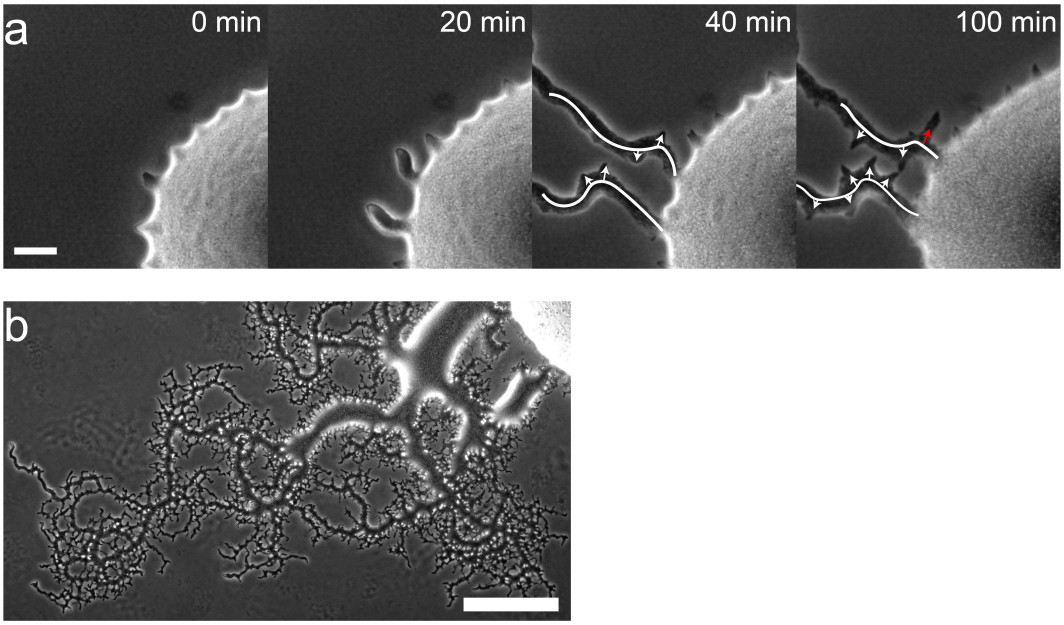

Figure 4.2: Hierarchical transition from interfacial protrusions to creeping branches. (a) Image sequence showing the transition from interfacial protrusions to creeping branches. Scale bar, 50 μm. t= 0 min is chosen at the onset of the protrusion-to-branch transition. White arrows on the $t = 40$ min and 100 min images represent the protrusions formed on the first branches, and the red arrow at t=100 min indicates a position where a secondary creeping branch is forming. (b) A self-similar pattern forms at larger times. The brighter region at the upper-right corner is the edge of the active suspension drop. Scale bar, 500 μm.

suspension drop is driven by defect-mediated active stresses, which is in contrast to the fractal-like branching patterns of bacterial colonies due to reaction-diffusion processes involving the coupling between cell mass growth and nutrient or chemoattractant fields [115, 116].

4.2.2 Interface curvature controls protrusion amplitude

In experiments with active suspension drops of an anisotropic shape, the first creeping branches are more likely to emanate from higher-curvature regions (**Fig. 4.3**(a)). Investigating the behavior of interfacial protrusions in active suspension drops with different shapes shows that the amplitude of the interfacial protrusions is positively correlated with the baseline curvature of the interface (i.e., the local curvature computed by smoothing out interfacial protrusions). For instance, the protrusion

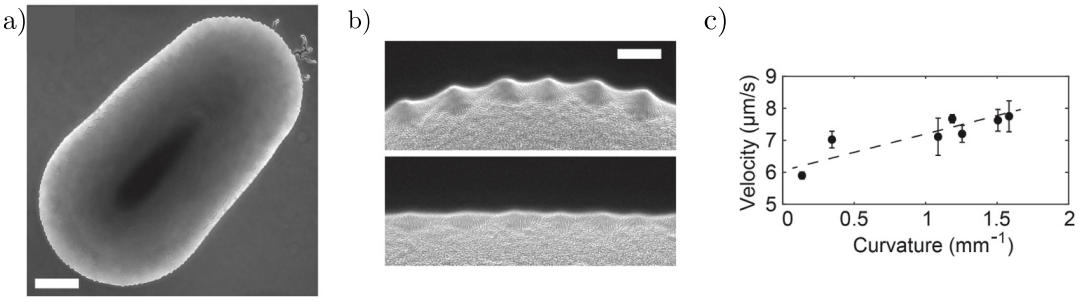

Figure 4.3: Curvature dependence of protrusion amplitude and protrusion-to-branch transition probability. (a) Phase-contrast image of an elongated P. mirabilis suspension drop with creeping branches appearing only at the pole at the upper right corner, where the baseline curvature is relatively high. Scale bar, 500 μm. (b) Enlarged view of the pole (upper) and the lateral side (lower) regions in panel a. Scale bar 50 μm. (c) Collective speed of cells behind the interface of active suspension drops (ranging from $\sim$ 20 to $\sim 50\mu m$ from the boundary) plotted against baseline curvature.

amplitude near the poles of an elongated drop (regions of higher curvature) is significantly greater than elsewhere while the inter-protrusion separation remains the same. These results show that the bacterial cells respond to mesoscale curvature (on a length scale much larger than single cell size) of the interface in a collective manner to drive the dynamics of interfacial protrusions. Here *collective* means that the change in the shape of the interface is caused by the collective interactions of many bacteria, rather than single cells; this is in contrast to curvotaxis of migrating cells where single cells respond to cell-scale curvature variations [117]. Therefore we denote the phenomenon as collective curvature sensing.

The motility deactivation experiment described above suggests that the protrusion amplitude is related to the magnitude of the active stress generated by the cells. Therefore, the collective curvature sensing may result from active stress heterogeneity in the active suspension drop. **Fig. 4.3**(c) shows that bacteria have a higher collective speed behind the boundary regions with larger curvature while the cell density is almost homogeneous (**Fig. 4.3**(c)).

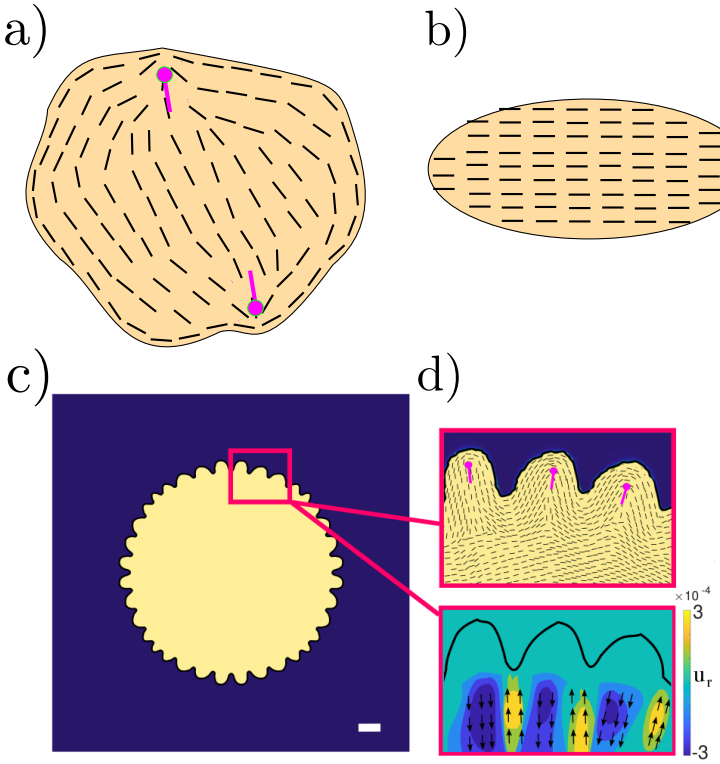

Figure 4.4: a) In active nematohydrodynamic equations, when the active length scale $c\sqrt{K_Q/\zeta}$ is small compared to the droplet radius, defects form and change the shape of the interface. The pattern formed at the interface is random, as it depends on where in bulk the defects first form. b) When the active length scale is large compared to the droplet radius, extensile droplets elongate along the direction of the nematic order. c) We modified the active nematohydrodynamic equations to account for experimental features such as parallel anchoring and the decrease of the nematic order towards the center of the droplet. We showed that the modified equations lead to formation of periodic patterns at the interface of an originally circular droplet. The scale bar is 15 lattice Boltzmann units. d) Shows a close-up view of the director orientation (top), and average velocity (bottom) at the interface.

4.3 Model and numerical simulations

The experiments suggest that the interfacial patterning is likely driven by active stresses produced by motile bacteria in the suspension drop. Active material droplets have been the subject of several numerical studies [28, 42, 59, 118]. In these studies, activity is shown to lead to interface deformation, formation of arms [28, 42], or droplet elongation [59, 118] (see **Fig. 4.4**(a) and (b)). In these studies the droplet deformations do not show any periodic patterns, and instead appear at random positions along the interface.

These show that there must be some features of the experiments that are missing in these studies which are based on the solution of the nematohydrodynamic equations. Looking at the experiments in more detail, we found that, the strength of the nematic order decays from the edge to the center of the droplet. In addition, we found that in the experiments the director field was initially parallel to the interface, even when the extensile activity was turned off. As a result, guided by the experiments, we construct a free energy that captures these observations. The modified free energy reads

$$f = \frac{\mathcal{A}}{2}(\mathcal{J}\phi - \mathbf{Q}:\mathbf{Q}/2)^2 + a\boldsymbol{\nabla}\phi\cdot\ \mathbf{Q}\ \cdot\boldsymbol{\nabla}\phi. \tag{4.1}$$

The first term in the free energy sets the magnitude of the nematic order inside the droplet to be equal to $\sqrt{\mathcal{J}}$, where $\mathcal{J}$ is a field that varies in time and space. To account for the fact that the magnitude of the order decreases towards the centre of the droplet, and since the position of the droplet and its interface is not fixed, we consider the following dynamics for this field,

$$\partial_t\mathcal{J} = D_s\nabla^2\mathcal{J} - k_s\phi, \tag{4.2}$$

and we set $\mathcal{J} = 1$ outside the drop where $\phi < 0.5$. This dynamics results in the magnitude of the order, and as a result the magnitude of the active stress, decaying towards the center of the drop. In the experiments, the centre of the drop forms a gel-like structure due to the expression of matrix. This leads to a lower motility compared to the region around the bacterial edge. In the model, inside the drop, the magnitude of the nematic order is related to the field $\mathcal{J}$ through the relation $S^2 = \mathcal{J}$, and outside the drop S is equal to zero.

The second term in **Eq. 4.1** is an anchoring free energy that favours parallel anchoring of the director at the interface for $a > 0$.

4.3.1 Parameters and measurements in numerical simulations

We choose the parameters of the simulation so that they lead to active turbulence in the bulk when the magnitude of the order is constant in space $S = 1$. These are

$\rho = 40$, $\Gamma = 0.3$, $\zeta = 0.01$, $\eta = 20/3$, $\gamma = 0.3$, $K_Q = 0.005$, $K_\phi = 0.01$, $\mathcal{A} = 0.001$, $A = 0.1$, $\Gamma_\phi = 0.1$, $\lambda = 0$. For the anchoring term, we choose a negative value $a = -0.005$ that leads to parallel anchoring. In the dynamics of $\mathcal{J}$, we choose the values $k_s = 0.0002$, and $D_s = 0.1$, that lead to smooth decay of the magnitude of the order in a length scale ~ 20 lattice Boltzmann units. These parameters are important in the behaviour that we observe in the simulations as when the length-scale over which the nematic order drops is very large, interfacial patterns become more random and are not periodic anymore. This is because defects that form at bulk can change the shape of the interface [28]. The size of the simulation box and the total time of the simulation are $L = 450$ and $t_{tot} = 5 \times 10^5$ in lattice Boltzmann units, respectively, and the radius of the drop is $r_0 = 150$. The key parameters of the simulations that determine the period of the protrusion pattern are elasticity K_Q and activity ζ. We showed that the period of the pattern is proportional to the length-scale $\sqrt{K_Q/\zeta}$. In addition, in our system the Reynolds number Re is small and we expect the behaviour of the system to be independent of ρ as long as $Re \ll 0.1$. We also found the same behaviour for the formation of patterns and the amplitude of the protrusions without surface anchoring $a = 0$. The period of the pattern is also independent of the surface anchoring term. In addition, parameter Γ only rescales the free energy parameters. Changing the friction coefficient γ changes the time scale over which the protrusions form and elongate. However, friction is not necesary for the formation of any of the patterns and behaviour we observed here. Finally, the surface tension coefficient K_ϕ sets how effective active flows are on deforming the shape of the interface. For very large surface tension, the active flows cannot change the shape of the interface and defects disappear at the interface without changing the shape of the droplet. The simulations are initialised with the director parallel to the interface and with a uniform angular noise in the interval $[0, 3\pi] \times 10^{-2}$.

To calculate the director and the average velocity field at the interface (**Fig. 4.3**(d)), we fix the edge of the drop once the protrusions and the defects form and average the flow in the vicinity of wide enough protrusions.

To perform simulations in an ellipse, we choose the long and the short axis to be equal to $r_2 = 150$ and $r_1 = 85$, respectively. The initial noise is uniformly distributed in the interval $[0, \pi] \times 10^{-3}$. All the other parameters are the same as the circular droplet.

4.4 Results

Our simulations show that at early times a bend instability forms around the drop, thus initiating protrusions at approximately regular positions around the interface (**Fig. 4.4**(c), and (d)). This instability is related to the instability of extensile active fluids, which when in contact with an interface, leads to interface deformation. The director configuration within the protrusions leads to outwards radial flow which in turn increases the definition of the protrusions and results in a director field resembling a $+1/2$ topological defect within each protrusion, as observed in the experiments (compare **Fig. 4.4**(d), top and **Fig. 4.1**(b), middle). Note also the alternating planar (between the protrusions) and perpendicular (under the protrusions) director field at the edge of the main drop.

To understand the velocity lattice observed in the experiments, we then mimick the very low velocity of the bacteria within the protrusions by reducing the activity to zero within the protrusions and by fixing the director orientation and the interface shape within the protrusions. The alternating director field at the drop edge acts as boundary conditions to stabilise a flow-vortex lattice with the same structure as in the experiments (compare **Fig. 4.4**(d), bottom and **Fig. 4.1**(b), bottom). This is a persistent state until we re-introduce a small activity within the protrusions. They then grow and eventually active material escapes from the protrusions, as the creeping branches did in the experiments.

The agreement between the phenomena in experiments and continuum modeling supports the notion that the bacterial suspension drop can be described as an active drop whose dynamics is driven by cell motility. Our simulations suggest that the pattern in experiments is rooted in the bend instability. Since the distance between the bend instability patterns (or equivalently defects) in simulations scales with

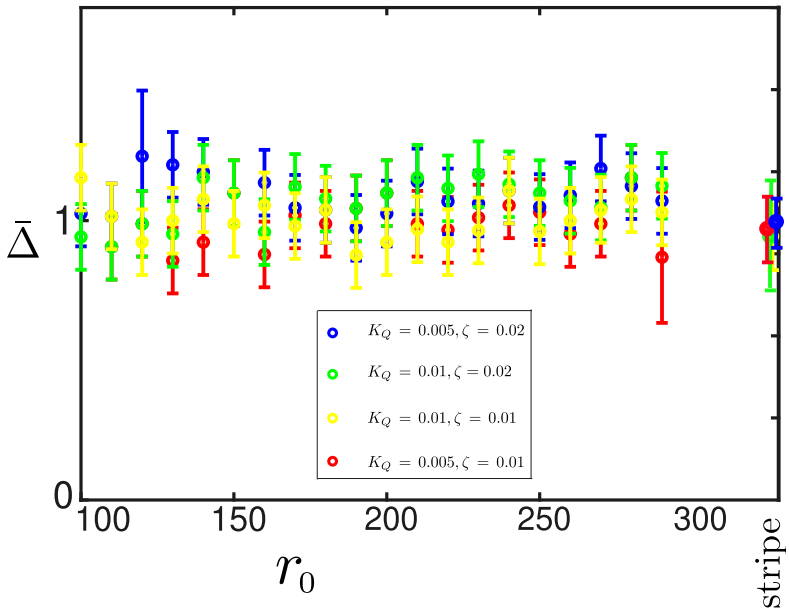

Figure 4.5: The distance between adjacent protrusions (rescaled with active length-scale $c_0\sqrt{K_Q/\zeta}$) as a function of drop radius r_0. The data shows that the distance between adjacent protrusions does not depend on the droplet radius (or equivalently interface curvature). The colour of the data points indicates different active length scales. The collapse of data in different colours shows that the distance between the protrusions is set by the active length scale. The distance between the protrusions in simulations with a stripe-shaped geometry with a width equal to 20 also collapses to a similar value when rescaled with active length scale (right-most part of the plot), showing that the average distance between protrusions in creeping branches, which have zero curvature, is also set by the active length scale.

active length-scale, we suggest that the period of the pattern is set by the active length scale $c_0\sqrt{K_Q/\zeta}$, where K_Q is the Frank elastic constant, ζ is the activity coefficient, and c_0 is a dimensionless coefficient that can be found by measuring the average distance between defects in large-scale simulations in bulk.

To test this, we perform simulations with different elastic constants and activities. Our simulations show that when rescaled with the active length scale, the distance between the protrusions (or protrusion width, which is roughly half of the protrusion separation) collapses on the same line (see **Fig. 4.5**). Using numerical simulations with droplets with various interface curvature shows that the period of the pattern does not depend on system size or geometry but is set by the active length scale (**Fig. 4.5**). This is also in agreement with the experiments as in the experiments

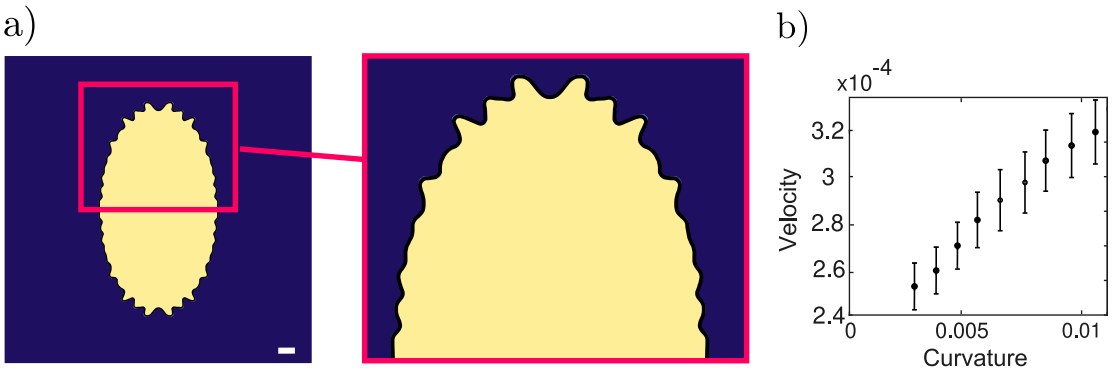

Figure 4.6: (a) Formation of protrusions in an elliptical droplet. The scale bar is 15 lattice Boltzmann units. The protrusions first start growing in regions with higher curvature (poles). (b) Average velocity at the interface of the elliptical droplet as a function of the curvature, before the formation of defects.

the period is not affected by the curvature, and rather appears to be set by an intrinsic length scale in the bacterial suspension.

To explain collective curvature sensing as found in the experiment, we then perform simulations of an elliptical active drop. The results are shown in **Fig. 4.6**. In agreement with the experiment, the protrusions first start growing in the regions of higher curvature (**Fig. 4.6**(a)), with the velocity near the interface of the elliptical drop proportional to curvature (**Fig. 4.6**(b)). This result can be understood as follows in the framework of our continuum model. The active force is proportional to the divergence of the nematic tensor $\mathbf{Q}$, and is increased by the bend distortion imposed on the director field by a curved interface. This is due to the parallel alignment of the director with the interface, promoted by both the anchoring term in the free energy and the extensile stress [59]. Since the director is aligned with a curved surface, it deviates from the nematic alignment and forms a bend that produces flows. Finally, looking at the dynamics of the interface at large times, shows that, similarly to the experiment, when branches become elongated enough, they undergo another bend instability and form new branches (**Fig. 4.7**(a) and (b)). Although the numerical resolution and lack of cell growth in the model prevent us from reproducing the large number of consecutive protrusion-to-branch transitions observed experimentally, our results show that the fractal-like pattern is created by consecutive bend instabilities due to active flows.

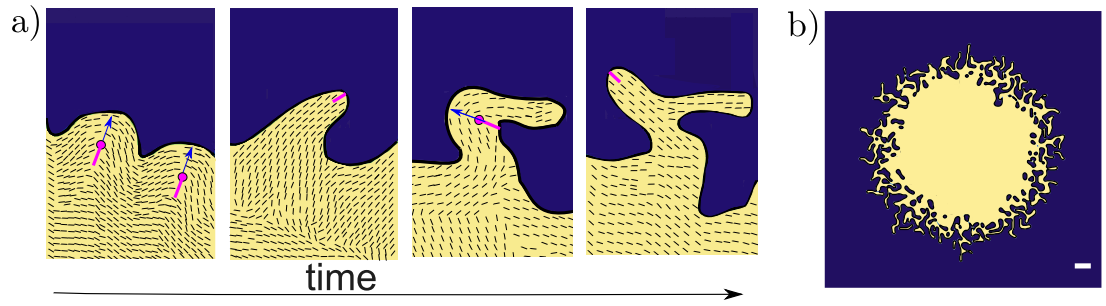

Figure 4.7: (a) As time passes, +1/2 defects move and form branches (elongated arms with nematic order). The elongated arms then undergo a bend instability and form another arm. (b) At very large times, all the arms have undergone bend instabilities, forming a pattern with many branches.

4.5 Summary

Taken together, we found a unique mode of active matter invasion mediated by the interaction between activity-induced flows and deformable interfaces. We modified the nematohydrodynamic equations according to features in *Proteus mirabilis* bacterial droplets, and recovered the patterns that form at the bacterial interface, including regularly-spaced interfacial protrusions; and transformation of the protrusions into creeping branches in a hierarchical, self-similar manner. We showed that the pattern is initiated by bend instabilities, and that enhanced active forces near high-curvature regions result in curvature-dependent protrusion dynamics which we term collective curvature sensing.

Self-organised pattern formation is a hallmark of living systems and a promising route to engineer functionalities of living materials. Ranging from bacterial colony development [116, 119] to animal embryogenesis [120], the formation of biological spatial patterns generally requires a complex interplay of genetic regulation, intercellular communication, and mechanical feedback [18, 121, 122]. By contrast, the ordered protrusion and branching pattern reported here relies on purely physical interactions between activity-induced flows and deformable interfaces. In particular, the phenomenon of collective curvature sensing shows that interface geometry may play an important role in active matter morphogenesis. It suggests a novel

strategy, i.e., designing curvature cues at the interface of active fluids, to guide and manipulate pattern formation in active materials.

Make everything as simple as possible, but not simpler.

Albert Einstein

5 Continuum approach for cell monalyers

5.1 Introduction

Epithelial tissue, which lines the surfaces of many organs and body cavities, comprises tightly packed cells, often just one cell thick. Confluent cell layers, plated on a substrate, provide a model system for the collective motion of epithelial cells and have been widely studied as a simple model of collective cell mechanics. Different modes of movement have been documented. The cells can remain in a glassy state with small fluctuations, but no relative motion [30, 123], or they can flock, all moving together in the same direction [124–128]. The flock is termed either liquid or solid, depending on whether the relative positions of the cells change as they move [129–132].

An isolated cell moves by forming lamellopodia which at a mesoscopic level can be described by a fluctuating polar force (**Fig. 5.1**(a)), however, many aspects of the dynamics of cell layers can strongly resemble the active turbulence observed in active nematics. This is characterised by velocity and vorticity correlations that extend over several cells and by the existence of $\pm 1/2$ topological defects [26, 133]. Further evidence of active nematic dynamics in cell monolayers is provided by their behaviour in confinement [134, 135].

Although cell monolayers share these features with theories of active nematics, there is now experimental evidence that some of the behaviour of cell monolayers cannot be explained by these theories. For example, active nematic theories suggest that a collection of isotropic cells cannot move, and the direction of the motion of defects in active nematic theories is fixed. These are in contrast with experiments that have observed the motion of isotropic cells [136, 137] and inconsistency between the direction of the motion of different $+1/2$ defects [133, 138]. Moreover, the balance between the role of actin within a cell changing its shape and actin at the cell membrane pulling on its neighbours is not clear.

In this chapter, we start from microscopic interaction between neighbouring cells and find the dynamics of the anisotropy, area, and orientation of a cell due to interaction with its neighbours. We then construct a continuum model for the dynamics of the fields associated to nematic tensor, anisotropy, and area of the confluent cell monolayers. We then solve the continuum model numerically to predict the effect of physical properties such as inter-cellular adhesion, and short-range and long-range active forces on the dynamics.

In section 5.2 we start from a microscopic model for a cell, and find the dynamics of the anisotropy in the shape of the cell, cell orientation, and cell area due to the forces exerted by the filaments inside the cell and due to interaction with neighbouring cells and active flows.

Having found the dynamics of cell anisotropy, area, and orientation, in section 5.3 we construct continuum equations that describe the dynamics of the fields associated with these quantities in the monolayer.

To understand the behaviour of the monolayer, in section 5.4 we perform linear stability analysis and numerical simulations of the continuum model. The results uncover formation of new phases in the monolayer, including jammed phases of isotropic cells, a nematic phase, a capped-line phase in which cells orient parallel to their close neighbours and perpendicular to the neighbours on a larger scale, and active turbulence with elongated cells.

Finally, in section 5.5 we generalise the model to account for the fact that active filaments inside the cells can have different properties such as different elastic constants and different responses to the flows compared to the cell membrane, and this introduces new phases in the monolayer. These include collective motion of isotropic cells, reversal in the direction of the motion of defects, and misalignment in the orientation of the defects in the filament field and defects in the cell shape field.

We finish the chapter with a summary in section 5.6.

5.2 Microscopic dynamics of a cell in a monolayer

To study the dynamics of a cell in a monolayer, we use a phase field $\varphi^{(i)}$ which shows the shape of the cell i. The phase field is equal to one ($\varphi^{(i)} = 1$) deep inside the cell and it smoothly goes to zero ($\varphi^{(i)} = 0$) outside the cell. We assume that cell i at position $\mathbf{r}_i$, orientation θ_i and long and short axes $l^i_\parallel$ and $l^i_\perp$ is represented by an anisotropic Gaussian field

$$\varphi^{(i)}(\mathbf{r}, \mathbf{r}_i, \mathbf{q}^i) = e^{-(\frac{\mathbf{r}-\mathbf{r}_i}{2})\cdot(\frac{\mathbf{I}+\mathbf{q}^i}{(\ell^i_\parallel)^2}+\frac{\mathbf{I}-\mathbf{q}^i}{(\ell^i_\perp)^2})\cdot(\frac{\mathbf{r}-\mathbf{r}_i}{2})}, \tag{5.1}$$

where $\mathbf{q}^i = (2\mathbf{d}^i\mathbf{d}^i - \mathbf{I})$ shows the nematic tensor of the cell, with $q^i_{11} = -q^i_{22} = \cos 2\theta_i$, and $q^i_{12} = q^i_{21} = \sin 2\theta_i$. The Gaussian representation (**Eq. 5.1**) is advantageous as it allows us to calculate the interaction between the cells analytically. This has been used in Ref. [139] to find the repulsive interaction between hard bacteria. The inset in **Fig. 5.1**(b) shows a schematic of the cell which has an elliptical shape.

Similar to the phase field model for cells in a monolayer [47], we assume that the dynamics of the cell phase field $\varphi^{(i)}$ is given by

$$\partial_t \varphi^{(i)}(\mathbf{x}) + \mathbf{v}^{(i)}(\mathbf{x}) \cdot \boldsymbol{\nabla} \varphi^{(i)}(\mathbf{x}) = -\beta \frac{\delta f}{\delta \varphi^{(i)}(\mathbf{x})}, \tag{5.2}$$

where $\mathbf{v}^{(i)}$ is the active velocity at the position of the cell, f is the free energy density, and the term on the RHS describes the relaxation dynamics of the cells to a free-energy minimum at a rate β.

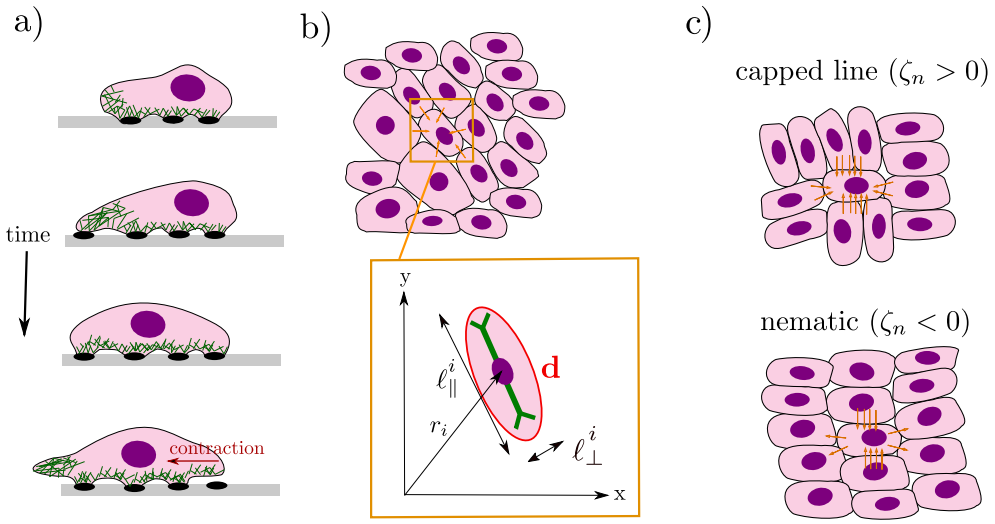

Figure 5.1: a) A cell moves by forming lamellopodia which at a mesoscopic level can be described by a fluctuating polar force. b) The formation of lamellopodia is suppressed in a confluent monolayer. The orange arrows show the contractile force exerted on cell i by its neighbours. The inset shows a cell that is described by a Gaussian field (**Eq. 5.1**), where $l^i_\parallel$ and $l^i_\perp$ show its long and short axes, respectively. Actin filaments inside the cell are shown by green. The filaments lead to self-interaction. c) Schematic representation of the active short-range force (orange arrows) in systems with extensile (top) and contractile (bottom) activities. Short-range activity elongates the cells in both cases.

In our model, we assume that active velocity originates from frictional interaction between neighbouring cells, the interaction between the filaments inside the cell with the cell (self-interaction), and active long-range flows.

The phase field introduced in **Eq. 5.1** has three pieces of information about the cell. These are cell orientation, and the lengths of the long and short axes of the cell. We can use the length of the axes of the cell to define the area and anisotropy of the cell as $A_i = \pi \ell^i_\perp \ell^i_\parallel$ and $\epsilon^i = (\ell^i_\parallel / \ell^i_\perp) - 1$, respectively.

In what follows we describe the evolution of the cell in the monolayer, by looking at the dynamics of the orientation tensor $\mathbf{q}^i$, the anisotropy in the shape of the cell ϵ^i, and the area of the cell A_i.

To find the dynamics of these quantities it is helpful to define the shape of the cell by a deformation tensor that reads

$$\begin{aligned} \boldsymbol{\mathcal{D}}^{(i)} &= -\int d\mathbf{x} \left\{ \boldsymbol{\nabla}\varphi^{(i)} \boldsymbol{\nabla}\varphi^{(i)^T} - \frac{\mathbf{I}}{2} \mathrm{Tr}(\boldsymbol{\nabla}\varphi^{(i)} \boldsymbol{\nabla}\varphi^{(i)^T}) \right\} \\ &= \sqrt{(\mathcal{D}^{(i)}_{xx})^2 + (\mathcal{D}^{(i)}_{xy})^2}\ (\mathbf{d}^{(i)} \mathbf{d}^{(i)^T} - \mathbf{d}^{(i)}_\perp \mathbf{d}^{(i)^T}_\perp), \end{aligned} \tag{5.3}$$

where $\mathbf{d}^{(i)}$ and $\mathbf{d}_{\perp}^{(i)}$ are unit vectors that show the orientation along and perpendicular to the elongation axis of the cell, respectively. This tensor is equal to zero for circular cells.

5.2.1 Neighbour-neighbour interaction

To look at the effect of the neighbour-neighbour interaction in the dynamics, we use **Eq. 5.3**, to find the dynamics of the shape tensor that reads

$$\partial_t \boldsymbol{\mathcal{D}}^{(i)} = -\partial_t \int d\mathbf{x} \left\{ \boldsymbol{\nabla}\varphi^{(i)} \boldsymbol{\nabla}\varphi^{(i)} - \frac{\mathbf{I}}{2} \mathrm{Tr}(\boldsymbol{\nabla}\varphi^{(i)} \boldsymbol{\nabla}\varphi^{(i)}) \right\}. \tag{5.4}$$

Eq. 5.4 shows that to find the dynamics of the shape tensor we need to calculate integrals of the form

$$\mathcal{J}_{mn}^{(i)} = -\int d\mathbf{x} \left\{ \nabla_n \varphi^{(i)} \nabla_m \partial_t \varphi^{(i)} \right\}. \tag{5.5}$$

We assume that the frictional velocity due to neighbour-neighbour interaction is given by $\frac{1}{f_0}\mathbf{f}_a^{(i)}$, where f_0 is a friction coefficient between the neighbouring cells, and $\mathbf{f}_a^{(i)}$ is the active force exerted on cell i by its neighbours. We can now use **Eq. 5.2**, to find the time derivative of $\nabla_m \varphi^{(i)}$ that reads

$$\nabla_m \partial_t \varphi^{(i)} \approx -\nabla_m \left\{ \frac{\mathbf{f}_a^i}{f_0} \cdot \boldsymbol{\nabla}\varphi^{(i)} \right\}, \tag{5.6}$$

where we have ignored the effect of passive terms. We can now use the active stress exerted on cell i due to its neighbours, $\boldsymbol{\sigma}_n = -\zeta_n \sum_{j\neq i} \boldsymbol{\mathcal{D}}^{(j)} \varphi^{(j)}$, to find the active force exerted on the cell. This reads

$$\begin{aligned} \mathbf{f}_{\mathrm{a}}^i(\mathbf{x}) = \boldsymbol{\nabla} \cdot \boldsymbol{\sigma}_n &= -\zeta_{\mathrm{n}} \sum_{j\neq i} \mathbf{D}^{(j)} \cdot \boldsymbol{\nabla}\varphi^{(j)}(\mathbf{x}) \\ &\approx \zeta_{\mathrm{n}} \sum_{j\neq i} \mathbf{D}^{(j)} \cdot \boldsymbol{\nabla}\varphi^{(i)}(\mathbf{x}), \end{aligned} \tag{5.7}$$

where in the last step, we have used the approximation $\boldsymbol{\nabla}\varphi^{(j)} \approx -\boldsymbol{\nabla}\varphi^{(i)}$. This approximation is only valid when the cell monolayer is confluent.

The shape tensor can be written as $\boldsymbol{\mathcal{D}}^{(i)} = \pi \mathbf{q}^{(i)} \epsilon^{(i)} (\epsilon^{(i)} + 2)/(4\epsilon^{(i)} + 4)$. At a linear order and for small cell anisotropy $\epsilon^{(i)}$ this simplifies to $\boldsymbol{\mathcal{D}}^{(i)} \approx \pi \mathbf{q}^{(i)} \epsilon^{(i)}/2$.

We can then use a mean-field approximation to approximate the average effect of the neighbouring cells on the force

$$\mathbf{f}_{\mathrm{a}}^{i}(\mathbf{x}) = \frac{\zeta_{\mathrm{n}}\mathcal{A}\pi}{2}\bar{\mathbf{D}}\cdot\boldsymbol{\nabla}\varphi^{(i)}(\mathbf{x}), \tag{5.8}$$

where $\bar{\mathbf{D}} = \mathcal{L}\mathbf{Q} + \frac{r_0^2}{2}\mathcal{L}\nabla^2\mathbf{Q}$ shows the average shape tensor of the neighbours with r_0 a typical length-scale corresponding to the distance between the neighbours, and anisotropy field defined as $\mathcal{L} = \langle\epsilon^{(i)}\rangle$. Here, we have assumed $\langle\epsilon^{(i)}\mathbf{q}^{(i)}\rangle = \langle\epsilon^{(i)}\rangle\langle\mathbf{q}^{(i)}\rangle$, and that spatial variation of the anisotropy field is smaller than that of the orientation field. Here, $\langle\rangle$ shows the average over cells distribution function, and $\mathcal{L}$ and $\mathbf{Q}$ are fields related to anisotropy and nematic tensor, respectively. Using Eqs. 5.5, 5.6, and 5.8 we can calculate $\mathcal{J}_{nm}$, and as a result $\partial_t\boldsymbol{\mathcal{D}}^{(i)}$ which reads

$$\partial_t\boldsymbol{\mathcal{D}}^{(i)} = \frac{-4\pi^3\zeta_{\mathrm{n}}}{27f_0}\bar{\mathbf{D}}. \tag{5.9}$$

In contrast to the conventional description of liquid crystals, where each particle is described by its orientation, here, an extra degree of freedom, i.e. shape anisotropy, appears in the dynamics. Using the dynamics of the shape tensor, we can find the dynamics of cell orientation $\mathbf{q}^{(i)}$ and cell anisotropy $\epsilon^{(i)}$. These read

$$\partial_t\mathbf{q}^{(i)} = \frac{8\pi^2\zeta_{\mathrm{n}}}{27f_0}(\frac{1}{2}\mathbf{q}^{(i)}\mathbf{q}^{(i)} : \bar{\mathbf{Q}} - \bar{\mathbf{Q}}), \tag{5.10}$$

$$\partial_t\epsilon^{(i)} = \frac{-4\pi^2\zeta_{\mathrm{n}}}{27f_0}\mathbf{q}^{(i)} : \bar{\mathbf{D}}, \tag{5.11}$$

where $\bar{\mathbf{Q}} = \mathbf{Q} + \frac{r_0^2}{2}\nabla^2\mathbf{Q}$, and we have assumed that cells anisotropy changes in space slower than cell orientation. Finally, we find the dynamics of the area field due to the active neighbour-neighbour interaction. This reads

$$\begin{aligned}\partial_t\mathcal{A}^{(i)} &= \frac{1}{2}\int d\mathbf{x}\partial_t\varphi^{(i)}\\ &= -\int d\mathbf{x}\frac{\mathbf{f}_a^i}{2\Gamma}\cdot\boldsymbol{\nabla}\varphi^{(i)}\\ &= \frac{\zeta_{\mathrm{n}}\pi\mathcal{A}}{4f_0}\boldsymbol{\mathcal{D}}^{(i)} : \bar{\mathbf{D}} \approx \frac{\pi^2\zeta_{\mathrm{n}}\mathcal{A}}{8f_0}\epsilon^{(i)}\mathbf{q}^{(i)} : \bar{\mathbf{D}},\end{aligned} \tag{5.12}$$

where in the last step, we have used an expansion for small $\epsilon^{(i)}$.

5.2.2 Self interaction

Active filaments in the cell exert active stress on the cell. We assume that this stress is proportional to the cell shape tensor and is given by $\boldsymbol{\sigma}_{self} = -\zeta_{self}\boldsymbol{\mathcal{D}}^{(i)}\varphi^{(i)}$, where $\zeta_{self} > 0$ ($\zeta_{self} < 0$) for extensile (contractile) inner cellular activity. Using the active stress we can find the active force on the cell as

$$\mathbf{f}_{\mathrm{a}}^{i}(\mathbf{x}) = \boldsymbol{\nabla} \cdot \boldsymbol{\sigma}_{self} = -\zeta_{\mathrm{self}}\boldsymbol{\mathcal{D}}^{(i)} \cdot \boldsymbol{\nabla}\varphi^{(i)}(\mathbf{x}). \tag{5.13}$$

Using **Eq. 5.13**, we can then find the dynamics of the shape tensor associated with cell i. This reads

$$\partial_t \boldsymbol{\mathcal{D}}^{(i)} = \frac{4\pi^2\zeta_{\mathrm{self}}}{27 f_0 A^i}\boldsymbol{\mathcal{D}}^{(i)}. \tag{5.14}$$

Contracting **Eq. 5.14** with $\mathbf{q}^i$ the dynamics of the anisotropy can be found as

$$\partial_t \epsilon^{(i)} = \frac{4\pi^3\zeta_{\mathrm{self}}}{27 f_0 A^i}\epsilon^{(i)}. \tag{5.15}$$

Eq. 5.15 shows that extensile (contractile) inner cellular activity makes it easier (more difficult) for the cells to elongate. This is in contrast to the neighbour-neighbour interaction force introduced in **Eq. 5.11** which decreases (increases) the cost of elongation in contractile (extensile) systems.

5.2.3 Active long-range flows

Having found the effect of the active neighbour-neighbour and self-interaction in the dynamics of the cell, we can now find the effect of the long-range flows on the dynamics of the cell elongation and the cell area. To find the effect of the long-range flows in the shape tensor we need to find

$$\partial_t \nabla_m \varphi^{(i)} = -\nabla_m(\mathbf{v} \cdot \boldsymbol{\nabla}\varphi^{(i)}) = -\nabla_m v_p \nabla_p \varphi^{(i)} - v_p \nabla_p \nabla_m \varphi^{(i)}. \tag{5.16}$$

Approximating the velocity and its gradient on the cell by the average of the velocity $\mathbf{u}$ and average gradient $\boldsymbol{\nabla}\mathbf{u}$, $\mathcal{J}_{mn}^{(i)}$ reads

$$\mathcal{J}_{mn}^{(i)} \approx \nabla_m u_p \int d\mathbf{x} \nabla_n \varphi^{(i)} \nabla_p \varphi^{(i)} + u_p \nabla_p \int d\mathbf{x} \nabla_n \varphi^{(i)} \nabla_m \varphi^{(i)}. \tag{5.17}$$

Calculating the integrals then enables us to find the dynamics of the shape tensor as

$$\partial_t \boldsymbol{\mathcal{D}}^{(i)} = -\mathbf{u}\cdot\boldsymbol{\nabla}\boldsymbol{\mathcal{D}}^{(i)} + \frac{\pi(1+[\epsilon^{(i)}+1]^2)}{2\epsilon^{(i)}+2}\mathbf{E} + \boldsymbol{\Omega}\cdot\boldsymbol{\mathcal{D}}^{(i)} - \boldsymbol{\mathcal{D}}^{(i)}\cdot\boldsymbol{\Omega}. \tag{5.18}$$

Contracting **Eq. 5.18** with $\mathbf{q}^i$ we can then find the dynamics of the anisotropy field due to the flows, which reads

$$\partial_t \epsilon^{(i)} = -\mathbf{u}\cdot\boldsymbol{\nabla}\epsilon^{(i)} + (\epsilon^{(i)}+1)\mathbf{E}:\mathbf{q}^{(i)}. \tag{5.19}$$

We can also find the effect of the velocity on the dynamics of the cell area which reads

$$\begin{aligned}\partial_t A^{(i)} &= \frac{1}{2}\int d\mathbf{x}\,\partial_t\varphi^{(i)} \\ &\approx -\nabla\cdot\mathbf{u}A^{(i)} - \frac{\mathbf{u}}{2}\cdot\boldsymbol{\nabla}\int d\mathbf{x}\varphi^{(i)} \\ &= -\mathbf{u}\cdot\boldsymbol{\nabla}A^{(i)},\end{aligned} \tag{5.20}$$

where in the second line we have approximated the velocity with the average velocity.

5.3 Continuum description of the monolayer

We assume that the dynamics of the flows is given by the Navier-Stokes equation with a low Reynolds number. We also assume that the dynamics of the nematic tensor $\mathbf{Q}$ due to the long-range flows is given by the Beris-Edwards equation introduced in chapter 2. Having known the relevant variables, in this section, we introduce the dynamics of the fields related to cell area, anisotropy, and nematic tensor. We define fields related to these variables as

$$\mathcal{A} = \sum_i \delta(\mathbf{r}-\mathbf{r}_i)\,\epsilon^{(i)} = \int A\,\psi\,d\theta\,dAd\epsilon, \tag{5.21}$$

$$\mathcal{L} = \sum_i \delta(\mathbf{r}-\mathbf{r}_i)\,A^{(i)} = \int \psi\,\epsilon\;d\theta\,dAd\epsilon \tag{5.22}$$

$$\mathbf{Q} = \sum_i \delta(\mathbf{r}-\mathbf{r}_i)\,\mathbf{q}^{(i)} = \int \mathbf{q}\,\psi\,d\theta\,dAd\epsilon. \tag{5.23}$$

where $\mathcal{L}$, and $\mathcal{A}$ are fields describing anisotropy in the shape of the cells and the area of the cells, and $\psi(\mathbf{r},t,\epsilon,A,\mathbf{q})$ is the single particle probability distribution function. The dynamics of the distribution function reads

$$\partial_t\psi(\mathbf{r},t,\epsilon,A,\mathbf{q}) = -\boldsymbol{\nabla}_r(\dot{r}\psi) - \boldsymbol{\nabla}_A(\dot{A}\psi) - \boldsymbol{\nabla}_\theta(\dot{\theta}\psi) - \boldsymbol{\nabla}_\epsilon(\dot{\epsilon}\psi). \tag{5.24}$$

We can then use the dynamics of the cell orientation, shape anisotropy, and area of the cell (**Eqs. 5.10- 5.12**, and **5.19- 5.24**), to find the dynamics of the fields related to these variables. The dynamical equations for the fields $\mathcal{X} = \{\mathbf{Q}, \mathcal{L}, \mathcal{A}\}$ read

$$\partial_t \mathcal{X} = \dot{\mathcal{X}}^f + \dot{\mathcal{X}}^I + \dot{\mathcal{X}}^s + \dot{\mathcal{X}}^u, \tag{5.25}$$

where $\mathcal{X}^f = -\Gamma_x \frac{\delta F}{\delta \mathcal{X}}$ shows relaxation to the minimum of the free energy with diffusivity Γ_x, $\mathcal{X}^I$ shows the effect of the active neighbour-neighbour interaction, $\dot{\mathcal{X}}^s$ shows the effect of active self-interaction, and $\mathcal{X}^u$ shows the effect of long-range flows on the evolution of the fields. The dynamics of the new terms read

$$\dot{\mathbf{Q}}^I = -\frac{4\pi^2 \zeta_n}{27 f_0} \bar{\mathbf{Q}}, \tag{5.26}$$

$$\dot{\mathcal{A}}^u = -\mathbf{u} \cdot \boldsymbol{\nabla} \mathcal{A}, \tag{5.27}$$

$$\dot{\mathcal{A}}^I = \frac{\pi^2 \mathcal{A} \zeta_n}{8 f_0} \mathcal{L}\mathbf{Q} : \bar{\mathbf{D}}, \tag{5.28}$$

$$\dot{\mathcal{L}}^u = -\mathbf{u} \cdot \boldsymbol{\nabla} \mathcal{L} + (\mathcal{L} + 1)\mathbf{Q} : \mathbf{E}, \tag{5.29}$$

$$\dot{\mathcal{L}}^I = -\frac{4\pi^2 \zeta_n}{27 f_0} \mathbf{Q} : \bar{\mathbf{D}}, \tag{5.30}$$

$$\dot{\mathcal{L}}^s = \frac{4\pi^3 \zeta_{\text{self}}}{27 f_0 A^i} \mathcal{L}, \tag{5.31}$$

where we have ignored higher-order orientational moments, and used $\langle \mathbf{q}^{(i)} \, \epsilon^{(i)} \rangle \approx \langle \mathbf{q}^{(i)} \rangle \langle \epsilon^{(i)} \rangle$. In the following subsections, we study the dynamics of these fields.

5.3.1 Dynamics of the orientation

As shown in **Eq. 5.26** active neighbour-neighbour interaction changes the critical isotropic to nematic transition temperature through the first term in $\bar{\mathbf{Q}} = \mathbf{Q} + \frac{r_0^2}{2} \nabla^2 \mathbf{Q}$. In systems with extensile (contractile) short-range interaction, ζ_n is positive (negative) and as a result, extensile (contractile) short-range interaction decreases (increases) the critical isotropic to nematic temperature. The active short-range interaction also introduces an elastic constant in the dynamics of the orientation field through the second term in $\bar{\mathbf{Q}}$. The elastic constant is negative (positive) in the extensile (contractile) systems and as a result, extensile short-range interaction favours perpendicular (parallel) alignment of the neighbours.

5.3.2 Dynamics of the area

Eq. 5.28 shows that anisotropic cells ($\mathcal{L} \neq 0$) change their area due to the force exerted by the neighbouring cells. The area change depends on the respective orientation of the neighbours. For elongated nematically aligned cells ($\mathbf{Q} : \bar{\mathbf{D}} > 0$), the area of the cells increases (decreases) due to extensile (contractile) short-range interaction. The opposite holds for elongated cells that are oriented perpendicularly (see **Fig. 5.1**(d)). We should note that in our model, we assume that cells are almost incompressible by penalising area changes in the free energy, and as a result our model only accounts for small changes in the area such that the dynamics of the other fields are not affected by the area change.

5.3.3 Dynamics of the cell anisotropy

Eq. 5.29 shows that strain rate changes the anisotropy in the shape of the cells. In systems with extensile (contractile) fluid activity, flows point outwards (inwards) along the elongation axis, and as a result $\mathbf{E} : \mathbf{Q}$ is positive and flows increase (decreases) cell elongation.

Eq. 5.30 shows that the dynamics of the anisotropy field $\mathcal{L}$ is also affected by the neighbour-neighbour interaction. Similar to the area change, the change in the elongation depends on the orientation of the neighbouring cells (through the term $\mathbf{Q} : \bar{\mathbf{D}}$), and the sign of the activity. For nematically aligned cells, the active short-range interaction elongates the cells in contractile systems and suppresses the elongation of the cells in extensile systems. This is shown in **Fig. 5.1**(d). On the other hand, in phases where the cells are perpendicular to their neighbours, $\mathbf{Q} : \bar{\mathbf{D}}$ is negative, and the elongation increases (decreases) by increasing extensile (contractile) activity. We will see later in simulations that cells orient perpendicular to their neighbours in extensile systems as they form an anti-aligned state.

Finally, **Eq. 5.31** shows that active self-interaction leads to cell elongation in systems with extensile self-activity, and decreases cell elongation in systems with contractile self-activity.

5.3.4 Free energy

To complete the set of equations for the dynamical fields $\mathcal{X}$, we need a free energy for the monolayer. Here, we introduce the free energy of the monolayer phenomenologically by keeping the lower-order terms in the fields and their gradient. The free energy density reads:

$$f = -\frac{C}{2}(1+\xi Q_{ij}Q_{ij}/2)^2 + \frac{K_Q}{2}\nabla_m Q_{ij}\nabla_m Q_{ij} + \frac{K_{\mathcal{A}}}{2}\nabla_m \mathcal{A}\nabla_m \mathcal{A} + \frac{K_{\mathcal{L}}}{2}\nabla_m \mathcal{L}\nabla_m \mathcal{L} + \frac{C_{\mathcal{L}}}{2}(\mathcal{L}-\mathcal{L}_0)^2 + \frac{C'_{\mathcal{L}}}{4}(\mathcal{L}-\mathcal{L}_0)^4 + \frac{C'_{\mathcal{A}}}{4}(\mathcal{A}_0-\mathcal{A})^4 + \frac{C_{\mathcal{A}}}{2}(\mathcal{A}_0-\mathcal{A})^2. \tag{5.32}$$

In **Eq. 5.32**, the first and the second terms show the Landau-de Gennes bulk free energy density and the elastic free energy density arising from spatial inhomogeneities in the nematic tensor. The third and fourth terms lead to the relaxation of the inhomogeneities in the area and anisotropy of the cells. Here, we choose $\mathcal{L}_0 = 0$, so that the terms with coefficient $C_{\mathcal{L}}$ and $C'_{\mathcal{L}}$ favour relaxation of the shape of the cells to an isotropic shape with $\mathcal{L} = 0$. Finally, the terms with coefficient $C_{\mathcal{A}}$ and $C'_{\mathcal{A}}$ show the relaxation of the area of the cells to the equilibrium value $\mathcal{A} = \mathcal{A}_0$.

In addition to the terms introduced in the free energy in **Eq. 5.32**, cells may feel an adhesion with their neighbouring cells. In the phase field model, adhesion enters through the following term in the free energy

$$\mathcal{F}_{\text{adh}} = \sum_i \sum_{j\neq i} \mathcal{W} \int d\mathbf{x}\, \nabla\varphi^{(i)} \cdot \nabla\varphi^{(j)}. \tag{5.33}$$

Using **Eq. 5.1** and **Eq. 5.33** one can show that in a continuum description, the adhesion adds a term $-\mathcal{W}\mathcal{L}^2/2$ to the free energy density, where $\mathcal{W}$ shows the strength of adhesion. This term is similar to the term with the coefficient $C_{\mathcal{L}}$ in **Eq. 5.32**, except it has a negative sign. This means that adhesion facilitates the elongation of the cells, and as such we can define an effective parameter in the free energy $C_{\mathcal{L}}^{eff} = C_{\mathcal{L}} - \mathcal{W}$ that can have a negative sign. This is in agreement with the simulations of the phase field model [140].

5.4 Linear stability analysis and phase diagram

To understand the behaviour of the cell monolayer, we first use the continuum equations to perform a linear stability analysis around a quiescent, isotropic phase with circular cells ($\mathcal{L} = 0 + \delta\mathcal{L}, \mathbf{u} = 0 + \delta\mathbf{u}, \mathbf{Q} = 0 + \delta\mathbf{Q}$), where $\delta\mathcal{L}, \delta\mathrm{u}, \delta\mathbf{Q} \ll 1$ are small perturbations around the steady state. Since the effect of the active self-interaction is clear, we assume that collective neighbour effects are stronger and set $\zeta_s = 0$, and study the effect of the neighbour-neighbour interaction and the active long-range flows in the stability of the system. We also assume that the flow-aligning parameter is related to the shape anisotropy by $\lambda = \frac{(\mathcal{L}+1)^2-1}{(\mathcal{L}+1)^2+1}$ [141]. Under these assumptions, the linear dynamics read

$$\partial_t \delta\mathbf{Q} = -(\Gamma C + \frac{4\pi^2\zeta_n}{27 f_0})\delta\mathbf{Q} + (\Gamma K - \frac{2\pi^2\zeta_n r_0^2}{27 f_0})\nabla^2\delta\mathbf{Q}, \tag{5.34}$$

$$\partial_t \delta\mathcal{L} = -C_\ell \delta\mathcal{L} - K_\ell \nabla^2 \delta\mathcal{L}. \tag{5.35}$$

Eqs. 5.34 and **5.35** show that in contrast to the instability of the elongated active particles in a disordered phase studied in chapter 2, long-range flows do not enter the dynamics of the fields at a linear order. The active neighbour-neighbour interaction, however, can destabilise the isotropic phase. The condition for the instability in contractile layers is given by $\zeta_n < -27\Gamma f_0 C/(4\pi^2) = \zeta_{crit}^{cont}$, and in extensile layers it is set by $\zeta_n > 27\Gamma f_0 K_Q/(2r_0^2\pi^2) = \zeta_{crit}^{ext}$.

The linear stability analysis predicts that a phase with isotropic cells becomes unstable for large extensile or large contractile short-range activities. The mechanism for the instability is different in extensile and contractile systems: contractile neighbour-neighbour activity increases the isotropic to the nematic transition temperature and introduces order to the system, while extensile short-range activity renders the elastic constant negative, and orients cells perpendicular to their neighbours. The perpendicular cells then elongate due to the extensile short-range interaction (**Fig. 5.1**(d), top). Since the mechanism of the instability is different in extensile and contractile systems, in contrast to traditional active nematic theories, the critical values of activity needed for the formation of order

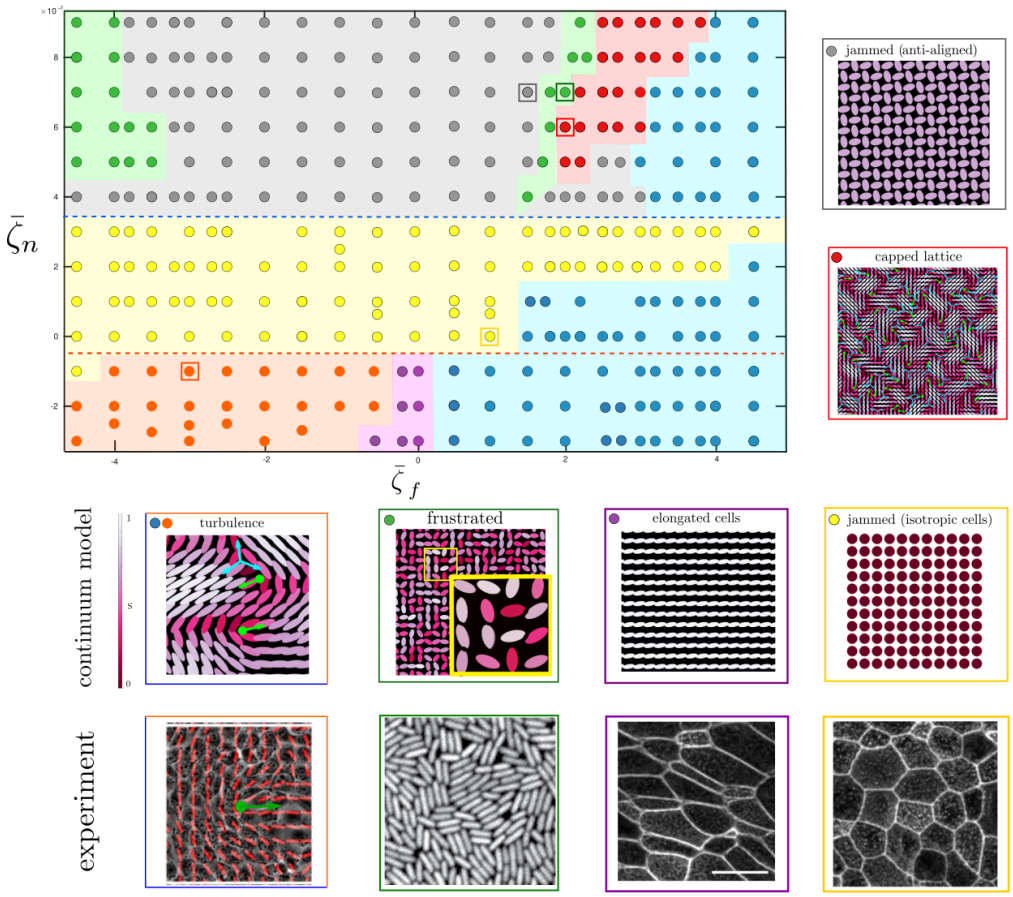

Figure 5.2: Phase diagram of the system, as a function of the renormalised active short-range interaction ($\bar{\zeta}_n^{ext} = \zeta_n/K_Q$ and $\bar{\zeta}_n^{cont}/C$) and active long-range interaction $\bar{\zeta}_f = \zeta/K_Q$. The phase diagram is plotted for two different values of elastic constant $K_Q = 0.01$ and 0.02, and two different values $C = 0.001$ and $C = 0.002$. The fluid activity is varied in the interval $-0.45 \leq \zeta \leq 0.45$, and the neighbour-neighbour activity in the interval $-0.003 \leq \zeta_n \leq 0.005$. The blue (orange) dashed lines show the boundary between the inert and the active phase predicted by a linear stability analysis of an isotropic phase with extensile (contractile) short-range interactions. The wavy background colour shows a regime where the linear stability analysis predicts a stable isotropic phase, but the non-linear strain rate term leads to cell elongation and active turbulence. At the bottom and right, different phases that appear in the phase diagram and similar phases observed in experiments are shown. The colour of the outline matches the data points in the phase diagram. In the continuum model the colour-bar represents the magnitude of the nematic order. The first and the second experimental snapshots are adapted from [133] and [142] respectively, and the last two snapshots are adapted from [143].

are also different in extensile and contractile systems. Note that in the phase diagram in **Fig. 5.2** the y-axis is rescaled differently in extensile ($\bar{\zeta}_n > 0$) and contractile ($\bar{\zeta}_n < 0$) systems. This is because the threshold of the instability is different in extensile and contractile systems.

To study the dynamics of the system, we then solve the continuum equations **5.25**- **5.31** numerically using the following sets of parameters: $\Gamma = 1.25$, $\xi = \Delta = 1$, $C = 0.001$, $C_{\mathcal{L}} = 0.0001$, $\zeta_s = 0$, $\rho = 40$, $r_0^2 = 2$. The initial condition in all the simulations is a quiescent phase $\mathbf{u} = 0$, with circular cells with a random uniform noise in the interval $0 < \mathcal{L} < 10^{-5}$. The direction of the order is also chosen from a random uniform number in the interval $(0, \pi)$. Simulations are performed in a 100×100 box with periodic boundary conditions and over a total time of 200000 (Lattice Boltzmann units).

The linear stability analysis revealed that critical short-range activity for the start of the instability of circular and mis-aligned cells is different in extensile and contractile systems. In system with extensile short-range activity the critical activity is proportional to ζ_n/K_Q, and in contractile systems it is proportional to ζ_n/C. As such, in presenting the numerical simulations, we choose y axis of the phase diagram in **Fig. 5.2** as $\bar{\zeta}_n = \zeta_n/K_Q$ and $\bar{\zeta}_n = \zeta_n/C$ in systems with extensile and contractile short-range activity, respectively. For the x axis, we choose the ratio between active fluid activity and the elastic constant (ζ/K_Q). Although active fluid activity does not appear in the dynamics of the system at a linear level, when the nematic order is formed, this leads to formation of the flows and defects. In addition, we observed in the simulations that, active fluid activity leads to cell elongation and nematic order at a non-linear level even without short-range activity, which is another reason we use this number as the x axis of the phase diagram.

In the phase diagram the horizontal blue and orange dashed lines show the critical value of the short-range extensile and contractile activities predicted by the linear stability analysis.

Without short-range activity and for small fluid activity, the isotropic phase is stable (the yellow region in the phase diagram). In this regime, cells maintain their circular shape and stay in a jammed state (yellow outline in **Fig. 5.2**).

For small fluid activity, large enough contractile neighbour-neighbour activity $(\zeta_n > \zeta_{crit}^{cont})$ leads to a nematic phase with elongated cells (purple outline). Here, since the velocity is small (small fluid activity), the nematic phase is stable and

does not lead to active turbulence. Increasing contractile fluid activity then leads to active turbulence with defects moving towards their tail.

For small fluid activity and for large extensile neighbour-neighbour activity ($\zeta_n > \zeta_{crit}^{ext}$), an anti-aligned phase appears where the cells orient perpendicular to their neighbours and elongate. This has a length scale that is set by the numerical lattice grid. We expect that in an agent based model, this length appears as a larger length compared to a single agent length. The anti-aligned phase is shown in a grey outline in **Fig. 5.2**.

Increasing extensile fluid activity then leads to a frustrated state where cells have both parallel and antiparallel neighbours (green outline in **Fig. 5.2**). This is similar to the capped-line phase observed in simulations of a monolayer of cells with extensile activity [140]. In the capped-line phase cells tend to align locally, at the scale of a few cells, and on a larger scale the average orientation is perpendicular to the neighbours (**Fig. 5.2**). Increasing the extensile flows even more leads to a capped lattice state where regions of aligned cells orient perpendicularly to their neighbouring regions (red outline in **Fig. 5.2**).

We should note that the mechanism for the formation of order and active turbulence in our system composed of isotropic cells, is based on active neighbour-neighbour interactions and at a linear level, is not caused by shear flow.

In our system, active shear flow only leads to instabilities when extensile flows are large, and at a non-linear level (wavy background in **Fig. 5.2**). In this regime, large extensile shear flows elongate the cells, make the flow-aligning parameter positive, introduce nematic order, and lead to active turbulence.

5.5 Misalignment between cell shape and stress

A bacterium exerts stress on the fluid due to its flagella which are, with a good approximation, along its body elongation axis. An important difference between a eukaryotic cell such as an MDCK cell and a bacterium is that the cell exerts stress on its surroundings by its active filaments and that the direction of the active filaments inside the cell is not necessarily along the direction of the cell elongation.

In the previous section, we assumed that the direction of the active stress (filaments) relaxes to the direction of cell elongation instantaneously. In this section, we relax this assumption and study the dynamics of monolayers in which the direction of the filaments is decoupled from the direction of the cell elongation.

In subsection 5.5.1, we study a tissue in which active filaments are in a nematic phase, but cells have an isotropic shape and are in an isotropic phase. This case is relevant in systems in which cells are circular without activity, for example in MDCK cells, and can change their shape due to active stress. We show that the response to the strain rate can change the behaviour of the tissue from contractile to extensile. This manifests in the direction of the motion of $+1/2$ defects.

In subsection 5.5.2, we study cells that have an elongated shape and consider both cells and filaments to be in a nematic phase. This could be relevant for example, in experiments on fibroblast cells that have an elongated shape and in which excluded volume interaction leads to formation of a nematic phase. We show that the defects in the cell elongation and in the active filaments appear in different positions when the elastic constant of the filaments and the cells are different. We then show that, when filaments undergo a gelation transition, the average velocity of the $+1/2$ defects in the cell shape goes to zero over time. This suggests a mechanism for observing non-motile $+1/2$ defects in the cell shape in experiments.

5.5.1 Living tissues with isotropic cells

In this subsection, we assume that cell elongation and filament direction are decoupled and introduce the dynamics of the fields associated with the cell nematic tensor and the filament nematic tensor. The dynamics of the cell elongation field remains the same as before. We assume that the effect of the active flows and the free energy on the cell orientation is given by the Beris-Edwards equation and reads

$$\begin{aligned}\partial_t \mathbf{Q} =& \Gamma C \mathbf{Q}(1 + \xi \mathbf{Q} : \mathbf{Q}) + \Gamma K \nabla^2 \mathbf{Q} - \mathbf{u} \cdot \boldsymbol{\nabla} \mathbf{Q} + \lambda(\mathbf{E} + \mathbf{E} \cdot \mathbf{Q} + \mathbf{Q} \cdot \mathbf{E}) \\ &+ \boldsymbol{\Omega} \cdot \mathbf{Q} - \mathbf{Q} \cdot \boldsymbol{\Omega},\end{aligned} \tag{5.36}$$

where the first term with $\xi > 0$ and $C < 0$ leads to the formation of an isotropic phase, the second term accounts for the elasticity of the cells, the third term shows the advection of the cells by the flows, the fourth term shows the rotation of the cells under the strain rate, and the last two terms show the rotation of the cells due to vorticity.

The dynamics of the filaments is also affected by the velocity field ($\dot{\mathbf{Q}}_a^u$) and by the free energy ($\dot{\mathbf{Q}}_a^f$) and is given by

$$\partial_t \mathbf{Q}_a = \dot{\mathbf{Q}}_a^u + \dot{\mathbf{Q}}_a^f, \tag{5.37}$$

$$\dot{\mathbf{Q}}_a^f = \Gamma_a C_a \mathbf{Q}_a (1 - 3\mathbf{Q}_a : \mathbf{Q}_a) + \Gamma_a K_f \nabla^2 \mathbf{Q}_a, \tag{5.38}$$

The first term in **Eq. 5.38** leads to formation of a nematic phase in active filaments for $C_a > 0$. The second term accounts for the elasticity of the active filaments.

We now find the change in the orientation of the active filaments by the flows ($\dot{\mathbf{Q}}_a^u$). We assume that the filaments rotate with the same angular velocity as the cells, $\dot{\theta}_c = \dot{\theta}_a$, where θ_c (θ_a) shows the angle, measured counterclockwise, between the cell (filament) orientation and x axis. As a result, vorticity enters the dynamics of the filaments as

$$\dot{\mathbf{Q}}_a^{u_1} = \mathbf{\Omega} \cdot \mathbf{Q}_a - \mathbf{Q}_a \cdot \mathbf{\Omega}, \tag{5.39}$$

where the superscript u_1 shows the effect of the vorticity. The effect of strain rate is more complicated as the amount of rotation due to strain rate depends on the cell orientation. A cell with flow-aligning parameter λ and director $\mathbf{d} = (\cos\phi_1, \sin\phi_1)$ rotates due to the strain rate as $\dot{\mathbf{d}} = \lambda(\mathbf{I} - \mathbf{dd}) \cdot \mathbf{E} \cdot \mathbf{d}$ [144]. This is equivalent to an angular velocity $\dot{\theta}_c = \lambda(E_{xy} \cos 2\phi_1 - E_{xx} \sin 2\phi_1)$ for the cell. Assuming that the filaments inside the cell rotate with the same angular velocity as the cells ($\dot{\theta}_c = \dot{\theta}_a$), we can find the dynamics of the nematic tensor field for the filament as

$$\partial_t \mathbf{Q}_a^{u_2} = -2\lambda(E_{xy} \cos 2\phi_1 - E_{xx} \sin 2\phi_1) \boldsymbol{\epsilon} \cdot \mathbf{Q}_a, \tag{5.40}$$

where $\boldsymbol{\epsilon}$ is the Levi-Civita tensor in two dimensions, and the superscript u_2 shows the effect of the strain rate on the dynamics of the filaments.

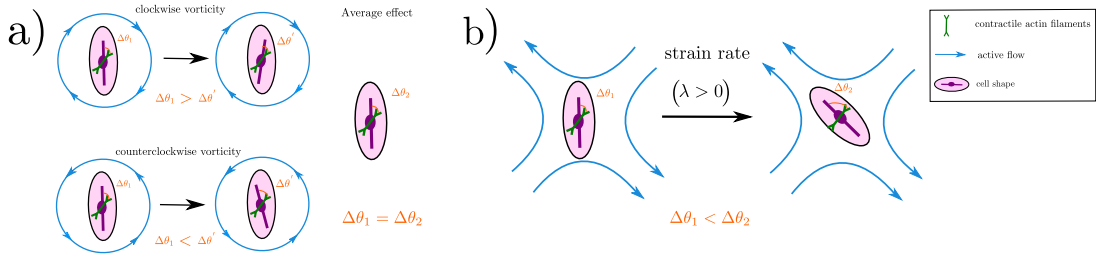

Figure 5.3: The effect of active contractile flows in the dynamics of the cell and filament orientation. When the passive part of the dynamics in the cell orientation is weaker than in the filaments ($\Gamma K < \Gamma_a K_f$), active flows, on average, are more effective in changing the orientation of cells compared to the filaments and could lead to the misalignment of cells and filaments. In this case, as shown in part (a), vorticity on average does not change the respective orientation of the cells and filaments. This is because clockwise and counterclockwise vorticities cancel the rotation of the cells with respect to the filaments. b) In a contractile (extensile) system, strain rate favours configurations in which cells align perpendicular (parallel) to the filaments.

We then perform numerical simulations to study the behaviour of the system for the following set of parameters: $\Gamma_a = 3.2$, $\zeta_n = 0$, $C_a = 0.0004$. The total time of the simulation is 5×10^5, and the system size is equal to 250×250. Other parameters are the same as section 5.4. Note that we have chosen $\Gamma_a = 3.2 > \Gamma = 1.25$ which leads to stronger elasticity in filaments compared to the cells. Figure 5.4(a) shows the phase diagram of the system. The y axis (x axis) shows the ratio of activity to cell (filament) elastic constant. For very large filament elastic constants (cyan data points), filaments stay aligned, the magnitude of active flows is zero and cells stay isotropic and non-motile. Decreasing filaments' elastic constant leads to the formation of defects in filaments, which leads to the motion of isotropic cells (black data points). Decreasing filaments' elasticity more (orange data points) leads to stronger flows that elongate cells, and form defects in the cell shape. In this region of the phase diagram, active flows are not strong enough to align or anti-align the cell shape with the filaments, and as such the position of the defects in the cell shape does not coincide with the position of the defects in the filaments.

Fig. 5.4(b) shows the magnitude of the flows in different phases in the phase diagram. As expected, the magnitude of the flow is smallest for small activity to filament elastic constant ratios. The area with small flow corresponds to the jammed phase in the phase diagram in **Fig. 5.4**(a).

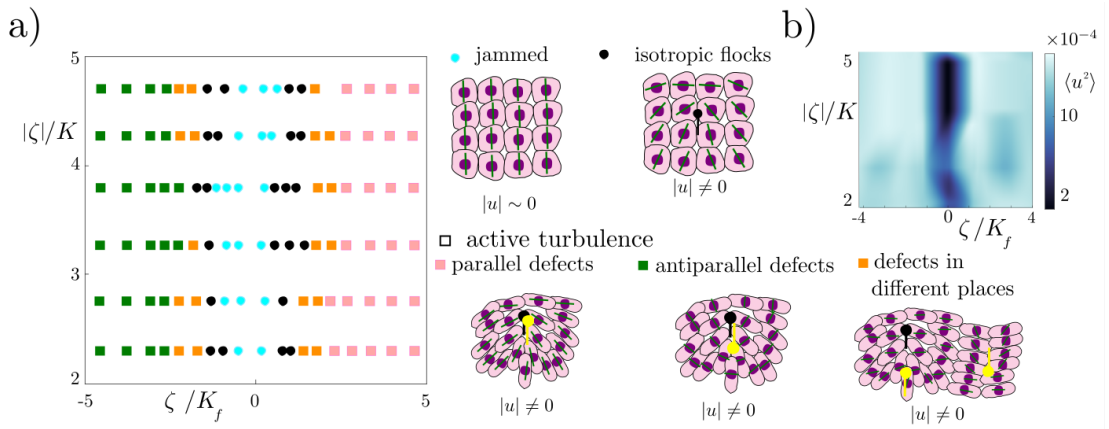

Figure 5.4: a) Phase diagram of a cell monolayer in which the dynamics of the cell orientation and filament orientation is decoupled, as a function of the ratio of activity ζ to the elastic constant of the cells K and elastic constant of the filaments K_f. The phase diagram shows a jammed phase of isotropic cells, a phase with motile isotopic cells, and active turbulence with elongated cells. In the active turbulence phase with large flows, the direction of the defects in the filaments is parallel (antiparallel) to the defects in the cell elongation in extensile (contractile) systems. As a result, defects move towards their head in both extensile and contractile layers. In the active turbulence phase with intermediate values of activity, the position of defects in the filaments and in the cell orientation does not coincide. b) Confirms that the magnitude of the velocity is zero in the jammed phase and becomes non-zero by increasing the ratio $|\zeta|/K_f$.

As we decrease the filament elastic constant even more, active flows become larger and are able to align or antialign the cells to the filaments. As a result, the position of the defects in the stress and in the cell elongation coincides. In this regime, cells are elongated and the flow-aligning parameter $\lambda = \frac{(\mathcal{L}+1)^2-1}{(\mathcal{L}+1)^2+1}$ is positive. To understand the different alignments of the cells with respect to the filaments in extensile and contractile systems, we can write the strain rate tensor created by a filament at the position of the cell as $\mathbf{E} = c'\zeta\mathbf{q}_a$, where $\mathbf{q}_a = (2\mathbf{hh} - \mathbf{I})$ is the filament nematic tensor, and $c' > 0$ is a constant. Using the relation for the strain rate, the angular velocity of the cell can be written as

$$\dot{\theta}_c = \lambda c'\zeta(\mathbf{q}_a \cdot \mathbf{d}) \cdot (\hat{z} \times \mathbf{d}) = \lambda c'\zeta((\hat{z} \times \mathbf{d}) \cdot \mathbf{h})(\mathbf{d} \cdot \mathbf{h}). \tag{5.41}$$

The cell angular velocity becomes zero for $\mathbf{h} \parallel \mathbf{d}$ or $\mathbf{h} \perp \mathbf{d}$. Assuming that passive dynamics of the filaments is stronger than the cells ($\Gamma K < \Gamma_a K_f$), filaments effectively rotate under the flows more slowly. One can then use **Eq. 5.41** to show that in a contractile system with a positive flow-aligning parameter, the

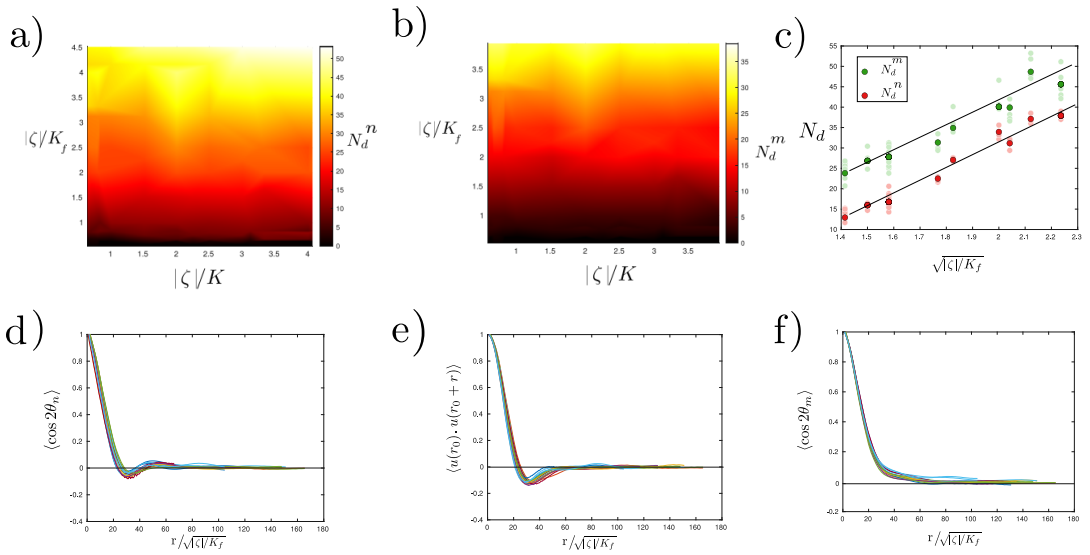

Figure 5.5: a) and b) show the number of defects as a function of $|\zeta|/K$ and $|\zeta|/K_f$ in the cell shape and in the active filaments, respectively. In both cases, the number of defects increases with increasing the ratio of activity to filaments elastic constant $|\zeta|/K_f$, and remains roughly constant with changing the ratio of activity to cell elastic constant $|\zeta|/K$. c) The number of defects in cell shape and in the filaments scales linearly with $\sqrt{|\zeta|/K}$. d)-f) The correlation in cell orientation, velocity, and active filament orientation scale with active filament lengthscale $(\zeta/K)^{1/2}$ and all data collapse when the distance is rescaled by active filament lengthscale. In c)-f) we varied the activity and the elastic constants in the intervals $0.03 < |\zeta| < 0.05$ and $0.01 < K_f, K < 0.08$.

solution $\mathbf{h} \perp \mathbf{d}$ is stable under small deviations of the cell orientation, and the solution $\mathbf{h} \parallel \mathbf{d}$ is not stable. In an extensile system with a positive flow aligning parameter, however, the former solution ($\mathbf{h} \parallel \mathbf{d}$) is stable. This confirms that for large extensile (contractile) flows, cells align parallel (anti-parallel) to the filaments and as a result, the position of defects in the cells and in the filaments coincide. In this regime, defects in cell shape are parallel (anti-parallel) to defects in the filaments in extensile (contractile) systems.

We then look at the number of defects in the cell shape and in the filaments. **Fig. 5.5**(a) and (b) show that the number of defects in the cell shape and in the filaments increases by decreasing filament elasticity and is not affected much by the cell elastic constant. This suggests that, when the flows are large enough to form defects in the filaments, they can also align cells respective to the filaments so that the cells form defects, independent of their elasticity. In the active nematic

theories considered so far, the distinction between the elasticity of cells and filaments has not been made. We suggest that, when studying cell layers, one needs to be more careful about defining the elastic constants. In agreement with this result, **Fig. 5.5**(c) shows that the number of defects in cell shape and filaments increases linearly with the active length scale of the filaments.

Finally, in **Fig. 5.5**(d)-(f) we show the correlation in cell shape orientation, velocity, and filament orientation scales with the active length scale of the filaments. These are in agreement with the graphs presented in **Fig. 5.5**(a)-(c).

5.5.2 Living tissues with elongated cells

In cell monolayers such as fibroblasts, it has been observed that some $+1/2$ defects do not move, or their direction of motion is not persistent and changes between moving towards head and tail. This observation is in contrast with active nematic theories where $+1/2$ defects always have a non-zero self-propulsion velocity either along their head or along their tail. In what follows, we use two examples to show that decoupling the dynamics of the active filaments and cell elongation can explain this controversy. In the first example, we consider a case in which the elasticity of the filaments is different from the cells and show that this leads to different positions of defects in the cell monolayer and in the active filaments.

In the second example, we study a case in which the filaments inside the cells undergo a gelation transition over time and show that this decreases the average velocity of defects in cell shape to zero over time.

Example 1: Distance between defects in cell elongation and stress

In this example, we study the average distance between defects in cell elongation and in filaments as a function of the elastic constant of the filaments. Here, we assume that cells are elongated and use $\mathcal{L}_0 = 1.3$. We also assume that they are in a nematic phase and set $\xi = -1$, $C_{\mathcal{L}} = C_a = C = 0.001$, $\zeta_f = -0.08$, $K_Q = 0.008$. The total time of the simulation is 9×10^5, and the system size is equal to 150×150.

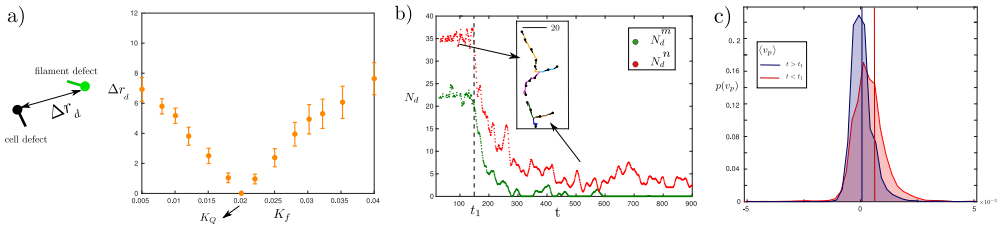

Figure 5.6: a) The average distance between defects in cell elongation and the closest defect in filaments. Defects in cell elongation and in filaments are not in the same place when the elastic constant of cells and filaments are different. For an equal elastic constant, the defects form in the same place, and $\Delta r = 0$. b) The number of defects in the active filaments and in cell shape over time in a system in which filament's elastic constant increases exponentially after a time $t > t_1$. The inset shows the trajectories of three different $+1/2$ defects before (top, $t < t_1$) and after (bottom, $t > t_1$) filament gelation. The scale bar shows 20 lattice grids. c) Velocity distribution along the symmetry axis of $+1/2$ defects. The red (blue) vertical lines show the average velocity at $+1/2$ defects towards their head before (after) gelation.

The result is shown in **Fig. 5.6**(a). The figure shows that when the elastic constants of the cell and the filaments are different, defects in cell elongation and in filaments appear in different places. The distance goes to zero as the difference between the elastic constants decreases (**Fig. 5.6**(a), orange). This shows that in the presence of activity, the difference between the passive properties of the cells and the filaments decouples the position of defects in the cell monolayer. As a result, depending on the orientation of the active stress around defects in cell shape, the defect can move towards its head or tail. This suggests a mechanism for understanding the non-persistent direction of the motion of the defects in cell monolayers.

Example 2: Filament gelation

We now consider an active cell monolayer in which the filaments start forming a gel after a time t_1. To model this, we consider the elastic constant of the filaments to exponentially increase over time for $t > t_1$ as $K_f(t > t_1) = K_{f0}(10 - 9\exp(-(t - t_1)/\tau))$. Here, we use $K_{f0} = 0.01$, $t_1 = 1.5 \times 10^5$, $\tau = 2 \times 10^5$. Other sets of parameters are the same as Example 1.

Fig. 5.6(b) shows the number of defects in the filaments and in the cell monolayer as a function of time. The inset shows the trajectories of three defects for $t < t_1$

and $t > t_1$. The motion of defects slows down after the gelation starts ($t > t_1$).

Fig. 5.6(c) shows the distribution of the velocity at $+1/2$ defects along their symmetry axis before (red) and after (blue) the start of the gelation. The average velocity is shown by a vertical line where the colour matches the colour of the histogram. The graph shows that the average self-propulsion velocity of $+1/2$ defects goes to zero as time passes after the gelation.

5.6 Summary

We introduced a continuum approach for cell monolayers and showed that circular cells can elongate, and exhibit nematic ordering and active turbulence due to active short-range and long-range interactions. The transition from an inert isotropic phase to a flowing phase with non-zero elongation is set by the active short-range interactions and there is a threshold for the short-range activity above which the isotropic phase becomes unstable, the cells elongate, and they become motile. This is in contrast to wet active nematic instabilities where a hydrodynamic long-range instability initiates flows at an activity threshold that goes to zero as system size goes to infinity [145]. In particular, in contrast to the isotropic phase of elongated rods in wet active systems, in a monolayer of isotropic cells, long-range flows cannot lead to instability at a linear level and the threshold for activity is different in extensile and contractile systems. In extensile systems, the threshold is set by the elastic constant, and in contractile systems, it is set by the free energy cost of forming a nematic phase. As a result, short-range extensile activity in a monolayer of isotropic cells leads to the formation of an anti-aligned phase. Increasing the flows leads to the formation of a capped lattice structure similar to experiments on bacterial rods and simulations of a phase-field model [140, 146]. Short-range contractile activity, on the other hand, leads to the formation of a nematic phase with elongated cells.

Finally, by decoupling the dynamics of active filaments from cell elongation, we showed that defects in cell shape do not necessarily coincide with or have the same orientation as defects in filaments. As a result, to be able to describe the direction of the motion of defects in cell monolayers, one also needs to look at

the orientation of active filaments. This decoupling could explain the non-motile defects observed in cell monolayers and the inconsistency in the direction of the motion of defects in cell monolayers.

Most things break, including hearts. The lessons of life amount not to wisdom, but to scar tissue and callus.

Wallace Stegner

6

Stress-shape misalignment in confluent cell layers

6.1 Introduction

In this chapter, we study the relationship between cell shape and cell-generated stresses in confluent cell layers. We first analyse experimental data on cell shape orientation and cell-generated contractile forces in MDCK colonies and report the emergence of correlated, dynamic domains in which misalignment between the directors defined by cell shape and by contractile forces reaches up to 90^o [147]. To understand this misalignment, we then use the continuum model that we developed in chapter 5 to decouple the orientation of cell-generated active stresses from the orientation of the cell shapes. This challenges the prevailing understanding that cells throughout a tissue create either contractile or extensile stress. Our continuum model reproduces the temporal and spatial correlations and misalignment angle observed in our experiments and emphasises the key role of flows in driving the misalignment.

In section 6.2 we introduce the experiments on MDCK cells, analyse the experimental data to find the nematic tensors associated with cell elongation and cell contractile stress, and present the results. In section 6.3 we introduce the continuum model, compare the results of our simulations with experiments, and

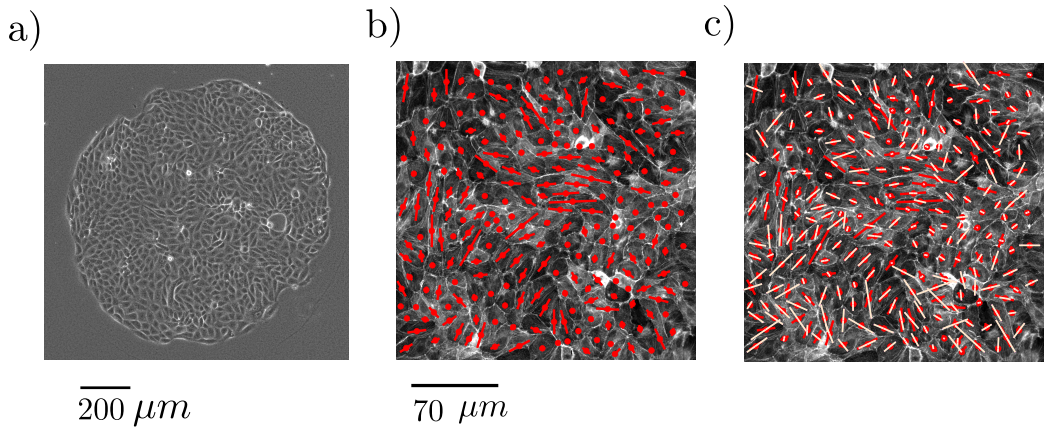

Figure 6.1: (a) Example of an MDCK island used in the experiments. (b) Example of a typical experiment measuring the long axis of cell shape orientation, **n**, (red lines) in an MDCK monolayer. (c) A typical set of results from experiments measuring the orientation of maximum contractile stress **m** (white lines) overlaid on the orientations of cell shape, **n** (red lines). In (b)-(c) the lengths of the red (white) lines are proportional to the deviation of the cell aspect ratio from unity (magnitude of the contractile stress).

show that the continuum model can capture the spatiotemporal correlations of the cell and stress orientation and the misalignment angle distribution. In section 6.4, we study the behaviour of LP9 cells in experiments and compare them with our simulations. We explain that the LP9 cells have a fixed elongated shape, that their dynamics is much slower than the MDCK cells, and that they only form very small extensile regions. We summarise our results in section 6.5.

6.2 Experiments on MDCK

The experiments are performed by Molly McCord, and Jun Zhang under the supervision of Jacob Notbohm, at the University of Wisconsin-Madison. The experimental system consists of confluent MDCK islands of diameter 1 mm (**Fig. 6.1**(a)). The experiments are performed over the course of 12 hours in 11 MDCK tissue samples, taking data every 15 minutes. Monolayer Stress Microscopy is used to measure the stress tensor $\boldsymbol{\sigma}$.

6.2.1 Analysing experimental data

We start by defining the cell shape orientation in the tissue by assigning each cell a director (headless vector) **n** which lies along the long axis of the anisotropic cell shape as shown in **Fig. 6.1**(b) [48]. The stress matrix measured in experiments has three independent components σ_{xx}, σ_{xy} and σ_{yy}. It has a non-zero trace, and we first make it traceless by adding a constant c to the diagonal elements, so that $\sigma_{yy} + \sigma_{xx} + 2c = 0$. In our model, we assume that the tissue is incompressible. As a result, an isotropic stress can be absorbed into the pressure and would not change our result. In general, tissues can be compressible if, for example, cells can change their height in the third direction. In our experiments, the area of the island is fixed and cells do not change their area in the two-dimentional plane.

To find the orientation of the contractile stress, we find the two mutually perpendicular axes which are parallel to the orientations of positive and negative principal stress. These axes can be found by a rotation of the stress matrix through an angle θ_p such that the shear stress σ_{xy} becomes zero. We note that there are two directions over which the shear stress becomes zero, θ_p and $\theta_p + \pi/2$. We define the orientation of contractile cell-generated stress to be along the orientation of the positive stress (pointing outwards). Having found the cell shape and stress orientation for each cell, we define θ as the misalignment angle between the local cell shape orientation **n** and the principal axis of contractile stress **m** in the tissue (**Fig. 6.3**(a)).

To find the position of defects, we need to find continuum fields for the nematic tensor associated with cells and the contractile stress. **Fig. 6.2** summarises the process of defining smooth director fields and identifying the position and orientation of defects. First, we map cell positions and orientations onto a square lattice with a lattice constant $dl = L/\sqrt{N}$, where L and N are the system length and number of the cells in the snapshot, respectively. To find the orientation of the cells on a lattice, we map each cell to the closest lattice site. The result is shown in **Fig. 6.2**(b). In the original lattice built by the cells, the lattice spacing is large and that makes it impossible to find the position and orientation of the defects accurately. As a

result, we need to find the cell orientation on a lattice with a smaller mesh size. We construct this lattice by linear interpolation between lattice points (**Fig. 6.2**(c)). Using the interpolated director field, we can then use a defect finding algorithm to find the position and orientation of ±1/2 defects (**Fig. 6.2**(d)).

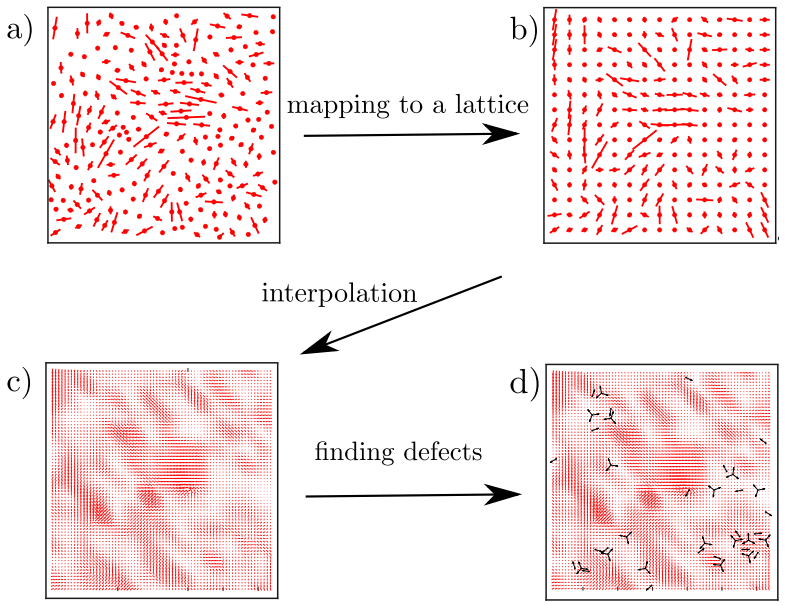

Figure 6.2: Construction of the director fields for cell orientation and contractile stress: a) Cell position and orientation, as shown in **Fig. 6.1**. b) Cell position and orientation after mapping to a lattice. The lattice unit is equal to $dl = L/\sqrt{N}$, where L is the linear snapshot size and N is the number of cells in the snapshot. c) Linear interpolation is used to find the director field on a lattice with a smaller mesh. This step is required to find the position and orientation of defects correctly. d) Using the director on the new lattice, we then use the defect-identifying algorithm introduced in Ref. [148] to find the direction and orientation of ±1/2 defects.

6.2.2 Experimental results

The distribution of θ is shown in **Fig. 6.3**(b). While most cells create contractile stress along their cell shape axis ($\theta \approx 0$), there is a large number of cells in which the axis of contractile stress is significantly misaligned with respect to shape orientation. If the misalignment angle reaches $\theta \approx 90°$, cells create contractile stresses perpendicular to the cell shape orientation, thereby pulling inward not along their long shape axis but rather along their short shape axis. In the following, we will refer to cells with large misalignment ($\theta > 45°$) as *extensile* and cells with

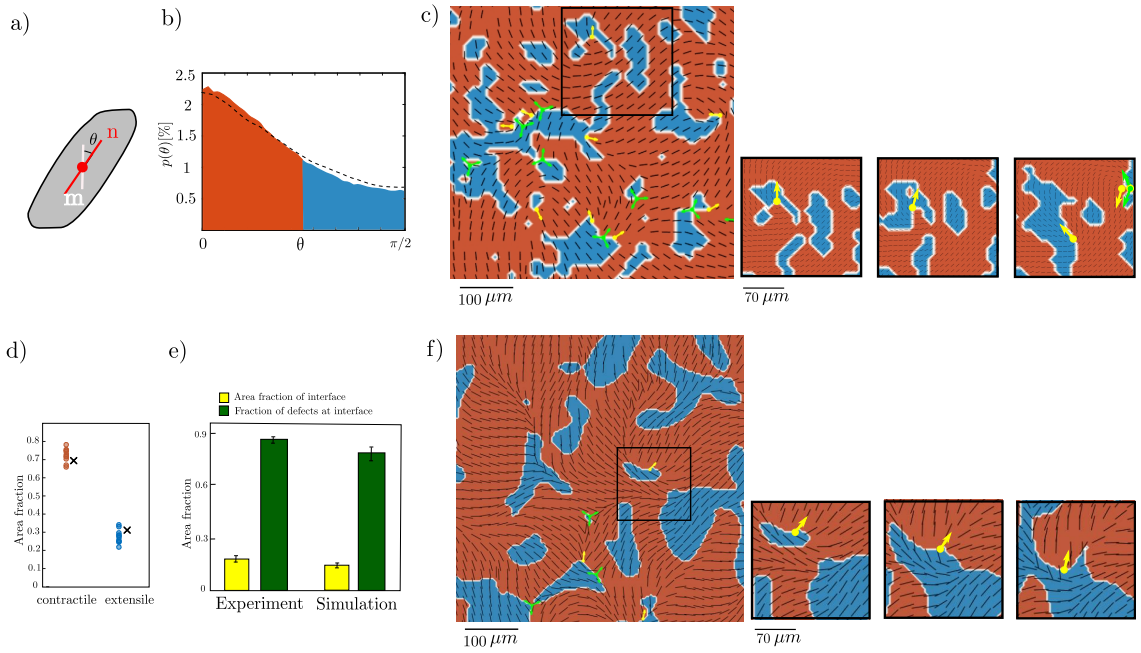

Figure 6.3: (a) Definition of the misalignment angle θ between the shape orientation axis **n**, and the principal axis of contractile stress **m**. (b) Distribution of the misalignment angle θ. Red/blue colouring denotes contractile ($\theta < 45^o$)/extensile ($\theta > 45^o$) values. The distribution contains data from 11 independent MDCK islands and all time points. The black dotted line shows the result from the simulation. (c) left: Tissue snapshot with the cell orientation field **n** shown as black lines on top of a colour map distinguishing contractile (red) and extensile (blue) regions. Topological defects in the cell orientation are indicated by yellow (+1/2) and green (−1/2) symbols. Right: Snapshots of a region of the same tissue taken 15 minutes apart showing the evolution of extensile clusters. The time axis is from left to right. (d) Experimental time average of the area fraction of contractile (red) and extensile (blue) cells for 11 different cell islands. The crosses show the results from simulations. (e) Defects are preferentially found in the vicinity of boundaries between extensile and contractile regions. (f) Snapshot from simulations with the cell orientation field **n** shown as black lines on top of a colour map distinguishing contractile (red) and extensile (blue) regions. Topological defects in the cell orientation are indicated by yellow arrow (+1/2) and green trefoil (−1/2) symbols. The time axis is from left to right.

small misalignment ($\theta < 45°$) as *contractile*, and we distinguish these ranges of θ as blue and red in **Fig. 6.3**(b). We now investigate the spatial and temporal correlation of the shape and the stress orientations in the MDCK monolayers. **Fig. 6.3**(c), left shows a tissue snapshot where the cell shape orientation field **n** is shown as black lines and the color map again indicates whether θ is greater (extensile, blue) or less (contractile, red) than 45°. **Fig. 6.3**(c), right shows the time evolution of a region of the tissue with snapshots taken at 15-minute intervals. It is evident that the

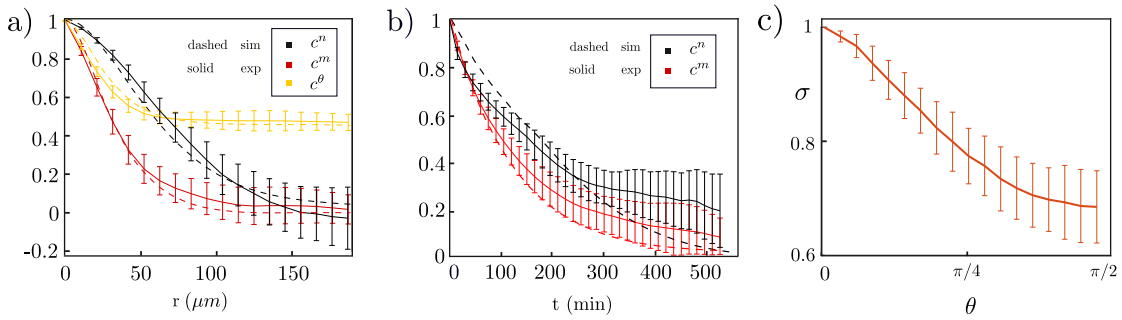

Figure 6.4: (a) Decay of the spatial correlation functions, $C^x(r) = \langle \cos 2[\psi_x(r+r_0,t_0) - \psi_x(r_0,t_0)]\rangle_{t_0,r_0}$, where ψ_x represents shape director angle $C^{\mathbf{n}}$, stress angle $C^{\mathbf{m}}$, or the mismatch angle C^{θ}. (Comparison of the simulation and the experiment assumes $10LB$ spatial units $\sim 44\mu m$.) (b) Decay of the time correlation functions, $C^x(t) = \langle \cos 2[\psi_x(r_0,t+t_0) - \psi_x(r_0,t_0)]\rangle_{t_0,r_0}$, where ψ represents shape director angle $C^{\mathbf{n}}$ or the stress angle $C^{\mathbf{m}}$. (Comparison of the simulation and the experiment assumes $100LB$ time units $\sim$ 10min.) (c) Magnitude of the stress σ as a function of the misalignment angle θ. The magnitude of the stress is re-scaled with its maximum value in each experiment before averaging. In all plots, the error bars show the standard deviation over 11 experiments.

misalignment angle forms evolving spatio-temporal patterns where extensile cells form small, dynamic clusters in a mostly contractile background. The extensile clusters grow, shrink, and coalesce over time. The time-averaged area fraction of extensile cells is $27 \pm 4\%$ (**Fig. 6.3**(d)). To further quantify the spatial patterns we calculated the spatial and time correlation functions of the cell shape orientation, the cell stress orientation, and the mismatch angle θ. These are defined as

$$C^x(r) = \langle \cos 2[\psi_x(r+r_0,t_0) - \psi_x(r_0,t_0)]\rangle_{t_0,r_0},$$
$$C^x(t) = \langle \cos 2[\psi_x(r_0,t+t_0) - \psi_x(r_0,t_0)]\rangle_{t_0,r_0}, \tag{6.1}$$

where ψ_x represents the shape director angle, stress angle, or the mismatch angle θ, and $\langle \ldots \rangle_{r_0,t_0}$ denotes an average over space (a circle of diameter $312\mu m$ in the centre of the island to avoid edge effects) and time. The spatial correlations, shown in **Fig. 6.4**(a), indicate a length-scale $\sim 50\mu m$ for the cell stress orientation, and a longer length scale $\sim 100\mu m$ for the cell shape orientation. From the time correlation functions, in **Fig. 6.4**(b), we identify a time-scale for the decay of the extensile patches $\sim$ 300 minutes.

Many cells contain bundles of actomyosin, termed stress fibres, that tend to form along the long axes of cells and are the primary source of contractile stresses [149].

Since the spatial correlation of the cell shape and stress orientation are different, we suggest that the regions of large misalignment angle are due to active flows disturbing the natural alignment of the stress fibres with the long axis of the cell due to different responses of the shape axis $\mathbf{n}$ and the stress axes $\mathbf{m}$ to flows.

Our interpretation leads to the prediction that in the extensile regions the stress fibres will be in the process of re-forming to realign with the new direction of cell elongation, and are therefore less efficient in producing contraction. In **Fig. 6.4**(c) we plot the magnitude of the contractile stress as a function of θ showing a clear decrease. Moreover, to check our interpretation visually we look at the fluorescent imaging of actin fibres in a selection of samples (**Fig. 6.5**). As shown in the figure, it is rarely possible to visually ascertain an unambiguous direction of the stress fibres in cells with large θ whereas stress fibres are much clearer in cases when they are aligned along the long axis of the cell.

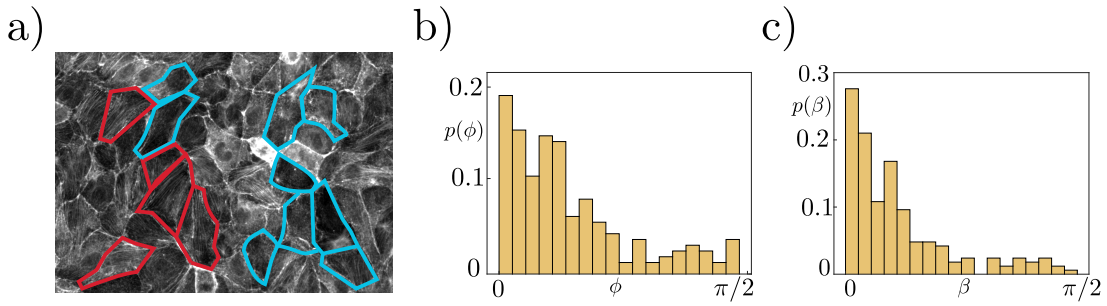

Figure 6.5: (a) Enlarged snapshot of the tissue in Fig. 1 where blue (red) contours specify extensile (contractile) cells. In general, the actin is clearer in the contractile cells, where shape, the principal axis of contractile stress, and the actin tend to be aligned. (b) Probability distribution of the angle between actin and the principal axis of contractile stress ϕ in cells where the actin was clear enough to enable a measurement. (c) Probability distribution of the angle between actin and the direction of cell shape elongation in cells β where the actin was clear enough to enable a measurement.

6.3 Continuum Model

To understand the formation of extensile areas in contractile tissues, we describe the shape of the cells and the stress using nematic order parameters $\mathbf{Q}^n = S^n(\mathbf{n}\otimes\mathbf{n}-\mathbf{I}/2)$ and $\mathbf{Q}^m = S^m(\mathbf{m}\otimes\mathbf{m}-\mathbf{I}/2)$, respectively [48], where S^n (S^m), shows the magnitude of the nematic order in cell shape (stress). We assume that the flows are created by

contractile active forces that act along the direction of stress fibres $\mathbf{m}$. The active flows advect the cells, and the vorticity of the flows rotates both the shape and the stress director fields. This description allows for a finite misalignment angle $\theta = \cos^{-1}(\mathbf{n}\cdot\mathbf{m})$ between the elongation axis of cell shape and the axis along which contractile forces are generated by stress fibres (see **Fig. 6.3**(a)).

We assume that in equilibrium the cell monolayer is governed by the following free energy density:

$$f = \frac{C}{2}(1-3\boldsymbol{Q}^n:\boldsymbol{Q}^n)^2 + \frac{C}{2}(1-3\boldsymbol{Q}^m:\boldsymbol{Q}^m)^2 + \frac{K_n}{2}|\boldsymbol{\nabla}\boldsymbol{Q}^n|^2 + \frac{K_m}{2}|\boldsymbol{\nabla}\boldsymbol{Q}^m|^2 + \frac{J}{2}(1-3\boldsymbol{Q}^n:\boldsymbol{Q}^m)^2. \tag{6.2}$$

In the absence of activity, the first and the second terms lead to a phase with nematic order in cell shape and cell stress. The third and the fourth terms penalise gradients in the shape and stress orientations, respectively. These are motivated by the observations of nematic ordering in both $\mathbf{n}$ and $\mathbf{m}$ in the experiments. The final term tends to align shape and stress orientations.

The shape orientation, $\mathbf{n}$, and the stress orientation, $\mathbf{m}$, also change in response to active flows. Since they have different elastic constants, they respond differently to the active flows which can lead to a mismatch between their directions. The dynamics of the nematic tensors is governed by [150]

$$(\partial_t + \mathbf{u}\cdot\boldsymbol{\nabla})\,\boldsymbol{Q}^n = -\boldsymbol{\Omega}_n^{'}\cdot\boldsymbol{Q}^n + \boldsymbol{Q}^n\cdot\boldsymbol{\Omega}_n^{'} + \Gamma\boldsymbol{H}^n, \tag{6.3}$$

$$(\partial_t + \mathbf{u}\cdot\boldsymbol{\nabla})\,\boldsymbol{Q}^m = -\boldsymbol{\Omega}_m^{'}\cdot\boldsymbol{Q}^m + \boldsymbol{Q}^m\cdot\boldsymbol{\Omega}_m^{'} + \Gamma\boldsymbol{H}^m, \tag{6.4}$$

where Γ is the rotational diffusivity, $\boldsymbol{\Omega}_m^{'} = \boldsymbol{\Omega} + \Delta_m$, $\boldsymbol{\Omega}_n^{'} = \boldsymbol{\Omega} + \Delta_n$, $\boldsymbol{\Omega} = (\boldsymbol{\nabla}\mathbf{u}^T - \boldsymbol{\nabla}\mathbf{u})/2$ is the fluid vorticity, $\Delta_{m/n}$ is a uniform noise in the rotation, the molecular field $\boldsymbol{H}^x = -(\frac{\delta f}{\delta \boldsymbol{Q}^x} - \frac{\boldsymbol{I}}{2}\,\mathrm{Tr}\frac{\delta f}{\delta \boldsymbol{Q}^x})$ shows the relaxation of the orientational order to the minimum of the free energy. In chapter 5 we showed that a positive flow-aligning parameter leads to perpendicular alignment of cell elongation with respect to the stress in contractile systems. Here, we have set the flow-aligning parameter equal to zero. As a result, any misalignment between cell elongation and the stress comes from different responses of the cell and the filaments to the vorticity due

to their different elastic constants, which we find by mapping spatial correlations in the experiments and in our simulations.

We further assume that the flows observed in confluent cell monolayers can be well approximated by Navier-Stokes equation [55, 150].

The simulations are performed in a 200×200 box with periodic boundary conditions over 120000 lattice-Boltzmann time-steps, and data is collected every 300 time-steps. The measurements are performed in a steady state when the mean number of defects and the fraction of the extensile area do not change over time. The initial orientation of both $\mathbf{n}$ and $\mathbf{m}$ is random, and the magnitude of the order is $(S^n)^2 = (S^m)^2 = 2/3$. We choose values of parameters that lead to an active fluid in a low Reynolds number regime: $\rho = 40, \eta = 20/3$. Other parameter values are: $\Gamma = 0.4, K_m = 0.005, C = 0.001, \zeta = -0.03, K_n = 0.065, J = 0.008$, and Δ_n and Δ_m are uniform random numbers in the interval $[-0.001, 0.001]$.

The results of the simulations is independent of ρ as long as Reynolds number Re is small ($Re \ll 0.1$). Changing viscousity η changes the active time scale and as such affects the time correlation. However, for any value of the viscousity that leads to a low Reynold number, it is possible to find an activity ζ that matches the time correlation functions in experiments and simulations. Parameter Γ only rescales the passive free energy parameters, and as such can be observed in other parameters without changing the results. In addition, the results of the simulations is independent of the parameter C, as long as it is large enough to lead to a nematic order. Having set these parameters, we can find values for the elastic constants K_m and K_n by matching the spacial correlation functions in simulations and experiments. Finally, parameter J can be varied to match the distribution function of the angle θ in experiments and simulations.

6.3.1 Comparision between simulations and experiments

The experimental spatial correlation functions show that the nematic order of the shape director $\mathbf{n}$ has a longer length scale than that of the stress director $\mathbf{m}$ which we model by choosing different elastic constants in the free energy ($K_m < K_n$).

This also means that the shape and the stress directors respond in different ways to the vortical flows leading to misalignment between **m** and **n**. In the continuum simulations, we have the freedom to choose a length and time scale, and we do this by matching the length and time scales of the correlation functions (**Eq. 6.1**) between simulation and experiment, as shown in Figs. 6.4(a) and 6.4(b).

We compare the simulation results to the experiments in **Fig. 6.3**. In agreement with the experiments, spatially correlated domains of extensile cells in a contractile background emerge in the simulations (**Fig. 6.3**(f)). We also obtain a quantitative match to the probability distribution for the misalignment angle θ if we use a realignment time scale of 25 minutes (**Fig. 6.3**(b)).

Active turbulence is also characterised by topological defects and we noticed that topological defects in the cell orientation field tend to sit at the interfaces between extensile and contractile domains. This is illustrated in Figs. 6.3(c) (experiment) and 6.3(f) (simulations) where $+1/2$ defects are indicated by a yellow arrow and $-1/2$ defects by a green trefoil. To quantify the results, we consider the points that are at a distance smaller than $r < 5.2\mu m$ (equal to the grid size after interpolation) from the interface as the *interface domain* while the rest of the tissue is defined as the *bulk domain*. A spatial and temporal average shows that interface domains make up about $18 \pm 2\%$ of the tissue area fraction in the experiments, and about $15 \pm 3\%$ of the area fraction in simulations. However, about $86 \pm 2\%$ ($86 \pm 5\%$) of defects lie within interface domains in experiments (simulations). These results are shown in **Fig. 6.3**(e).

6.4 LP9 cells

We now study the behaviour of the human mesothelial cell line LP-9 (**Fig. 6.6**(a)). These cells, which have an elongated morphology with a high aspect ratio, show a behaviour that contrasts with the MDCK islands. A very small number of topological defects are present at the beginning of the experiments. These persist and remain in approximately the same position throughout the experiments (40 hours) and no new defects are created, indicating that the cell layer is behaving

primarily as a passive nematic, with any active flows not sufficiently strong to create defects or substantially change the cell orientation. There is, however, still a population of extensile cells with $\theta > 45°$, but it is far smaller than in the MDCK monolayers. The extensile cells form small (3.4% of the area of the tissue) clusters (**Fig. 6.6**(b)) adjacent to the defects in the cell shape director field and persist within the time scale of the experiment.

We set up the LP-9 simulations such that nematic order only forms inside a circular region with radius $R = 80$. The free energy in this region is again given

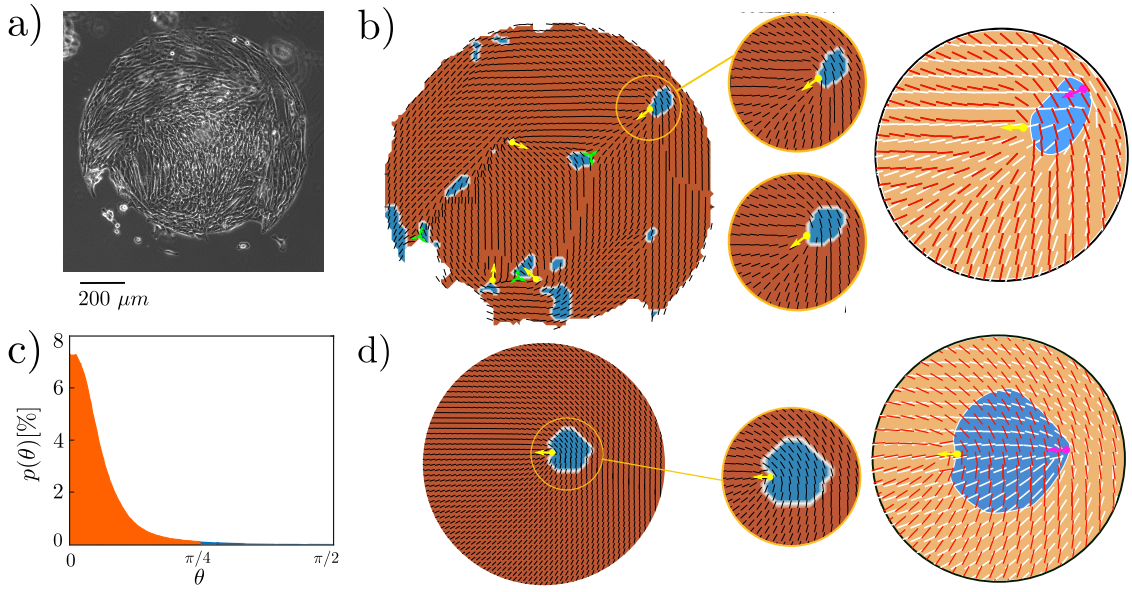

Figure 6.6: (a) Snapshot of an LP-9 island. (b) left: Tissue snapshot with the cell shape orientation field **n** shown as black lines on top of a colour map distinguishing contractile (red) and extensile (blue) regions. Topological defects in the cell shape orientation are indicated by yellow (+1/2) and green (−1/2) symbols. Middle: Snapshots of a region of the same tissue taken 40 minutes apart showing that the extensile cluster remains fixed. The time axis is from top to bottom. Right: Close-up view of the same tissue. Cell shape orientation is shown in red and stress orientation is white. The colourmap shows the extensible (blue) and contractile (orange) regions (smoothed). The defect in the cell shape (stress) orientation is shown in yellow (magenta). (c) Distribution of the misalignment angle θ. Red/blue colouring denotes contractile ($\theta < 45^o$)/extensile ($\theta > 45^o$) values. The LP-9 cells predominantly form contractile regions (compare Fig. 2b for MDCK cells). (d) Left: Snapshot from simulations with the cell shape orientation **n** shown as black lines on top of a colour map distinguishing contractile (red) and extensile (blue) regions. The +1/2 defect in the cell shape is indicated by a yellow arrow. Right: Close-up view of the same tissue. Cell shape orientation is shown in red and stress orientation is white. The colourmap shows the extensible (blue) and contractile (orange) regions (smoothed). The defect in the cell shape (stress) orientation is shown in yellow (magenta).

by **Eq. 6.2**, but the bulk free energy outside the circle is

$$f_{bulk} = \frac{C'}{2}(\boldsymbol{Q}^n : \boldsymbol{Q}^n)^2 + \frac{C'}{2}(\boldsymbol{Q}^m : \boldsymbol{Q}^m)^2, \tag{6.5}$$

which sets the magnitude of the order to be zero. We impose a defect in the shape director **n** at the centre of the inner region by setting the director angle with the x axis to be equal to $\phi/2$, where ϕ is the polar angle in the co-ordinate system centered at the defect core. We do not allow **n** to vary in time; **m** relaxes towards the minimum of the free energy. We use the same parameter values as for the MDCK cells except $K_m = 0.02, K_n = 0.01, \zeta = 0, \Delta_m = \Delta_n = 0$. The LP9 cells are less motile and do not show any dynamics (including formation and annihilation of defects, and self-propulsion of defects) over the experiments. As a result we set the activity to zero here. Here, we only compare the simulation results qualitatively with the experiments. The elastic constants and the alignment parameter can be changed together to lead to a similar result (formation of an extensile patch around the central defec).

As shown in **Fig. 6.6**(c), an extensile region indeed forms next to the defect in cell shape **n**. This dynamical steady state is a result of the balance between the elastic energy, which favours nematic alignment of the stress directors **m**, and the term which encourages **m** to align with **n**. The exact size and position of the extensile region relative to the defect varies, depending on the initial condition for **m**, indicating the existence of metastable solutions.

6.5 Summary

We analysed experimental data on MDCK and LP9 cells to find the cells' shape and stress orientation in these layers. Our results on MDCK cells show that active flows and the different elastic properties of cell shapes and active stress filaments lead to long-lived extensile regions in contractile monolayers. In contrast with the MDCK cells, a very small number of topological defects and small extensile regions exist in the LP9 cells.

We showed that the generalised form of active nematohydrodynamic equations that decouples cell shape and stress orientation captures the distribution of the misalignment angle between cell and stress, and the spatiotemporal correlations in the orientation of cells and the stress.

I call our world Flatland, not because we call it so, but to make its nature clearer to you, my happy readers, who are privileged to live in Space.

Edwin A. Abbott

7

Active extensile stress promotes 3D director orientations and flows

7.1 Introduction

As we discussed in previous chapters, the hydrodynamic instabilities in active nematics lead to the growth of deformations in the nematic orientation field, giving rise to formation and separation of point-like topological defects of opposite charges in two dimensions. In three-dimensional active nematics, the dynamics of defects is more complex. Here, the previously two-dimensional point-like defects extend into the third dimension, giving rise to disclination lines. In addition, in three dimensions, the director field around defects has more freedom and can form new types of defects compared to two-dimensional systems. Recent research has embarked on categorising 3D active nematics, uncovering the emergence of contorting disclination lines driven by active forces and capable of undergoing twist deformations [44, 151, 152].

In this chapter, we study the differences between 2D and 3D active nematics by performing numerical simulations of the nematohydrodynamic equations and linear stability analysis. We first consider an active two-dimensional layer, with periodic boundary conditions in all three directions, where the director can acquire a 3D orientation. We refer to this setup as a quasi-2D system and present the results in section 7.2. Studying the behaviour of the quasi-2D system could be

helpful in shedding light on the behaviour of active nematic systems in 3D, and in understanding the growth of 2D layers into three dimensions [33, 153–157].

We show that extensile and contractile materials demonstrate remarkably different behaviours in this setting. While extensile systems form twist type defects and promote three-dimensional flows, contractile systems form wedge-type defects and two-dimensional flows.

Having understood the behaviour of the quasi-2D system, in section 7.3 we use linear stability analysis to study the growth of twist perturbations in fully three-dimensional active nematics, and show that twist perturbations grow in extensile systems and get suppressed in contractile systems. In agreement with the result of the linear stability analysis, simulations of active turbulence in three dimensions favour formation of twist type defects in extensile systems and wedge type defects in contractile systems. Finally, we perform simulations of initially two-dimensional droplets embedded in three dimensions and show that extensile droplets grow to the third dimension whereas contractile droplets grow in two dimensions.

We finish the chapter by summarising our findings in section 7.4.

7.2 Quasi-2D system

In subsection 7.2.1, we use linear stability analysis to study the stability of the nematic phase in the quasi-2D system. We then perform numerical simulations and study the dynamics of the quasi-2D system, in subsection 7.2.2.

7.2.1 Linear stability analysis

To study the behaviour of extensile and contractile systems in the quasi-2D setup, we perform a linear stability analysis of the nematohydrodynamic equations around the fully-aligned in-plane nematic phase. We consider the active nematic layer to be in the x-y plane with $3D$ director field and study the growth rate of in-plane and out-of-plane director perturbations deep in the nematic phase where $S \approx 1$. Without loss of generality, we consider the direction of the nematic order to be along the x axis. We also assume a zero Reynolds number regime which

allows us to use the Stokes equation instead of the Navier-Stokes equation. In agreement with the periodic boundary condition in the simulations, we assume that the system is invariant along the z direction. Decomposing any fluctuating field as $\delta f(\mathbf{r},t) = \int d\mathbf{q}\, d\omega \tilde{f}(\mathbf{q},\omega)\, e^{i\mathbf{q}\cdot\mathbf{r}+\omega t}$, we can find the closed form for the evolution of the perturbations in the director field, which read:

$$\omega\tilde{Q}_{xy} = \frac{\zeta}{2\eta}\tilde{Q}_{xy}\left\{2B\cos^2 2\theta + 3\sin^2\theta\cos 2\theta\right\} - K_Q\Gamma q^2\tilde{Q}_{xy}, \tag{7.1}$$

$$\omega\tilde{Q}_{xz} = \frac{\zeta}{2\eta}B\left\{2\cos^2\theta\tilde{Q}_{xz} + \sin 2\theta\tilde{Q}_{yz}\right\} - \Gamma K_Q q^2\tilde{Q}_{xz}, \tag{7.2}$$

$$\omega\tilde{Q}_{yz} = \frac{-\lambda\zeta}{12\eta}\left\{2\sin^2\theta\tilde{Q}_{yz} + \sin 2\theta\tilde{Q}_{xz}\right\} - \Gamma K_Q q^2\tilde{Q}_{yz}, \tag{7.3}$$

$$4B = \frac{7}{3}\lambda + 3.$$

Eq. 7.1 is decoupled from **Eq. 7.2** and **Eq. 7.3**, and gives the growth rate of the in-plane perturbations $\omega_{in} = \Re(\omega)$. **Eq. 7.2** and **Eq. 7.3** are coupled and lead to a quadratic equation for the growth rate of the out-of-plane perturbations $\omega_{out} = \Re(\omega)$. Note that, at a linear level, the dynamics of the components $\tilde{Q}_{xx}$, $\tilde{Q}_{yy}$, $\tilde{Q}_{zz}$ is not affected by the velocity field and any perturbation in their dynamics is suppressed by the free energy. Since the onset of instability is given by the real part of $\omega > 0$, it is enough to consider the larger solution and, in the long-wavelength limit, the growth rates of the perturbations can be written as

$$\omega_{in} = \frac{\zeta}{4\eta}\cos 2\theta\left\{\frac{7}{3}\lambda\cos 2\theta + 3\right\} - K_Q\Gamma q^2, \tag{7.4}$$

$$\omega_{out} = \frac{\zeta}{4\eta}\left\{-\frac{2}{3}\lambda + 3\cos^2\theta(1+\lambda)\right\} - K_Q\Gamma q^2. \tag{7.5}$$

In the case of zero flow-aligning parameter, the growth rates simplify to

$$\omega_{out} = \frac{3\zeta}{4\eta}\cos^2\theta, \;\; \omega_{in} = \frac{3\zeta}{4\eta}\cos 2\theta. \tag{7.6}$$

The in-plane component ω_{in} shows the well-known instability of 2D active nematics to bend (splay) perturbations in extensile (contractile) systems [158]. By contrast, the growth rate of the out-of-plane component ω_{out} does not change sign for different values of θ and is positive (negative) for extensile (contractile) systems. Thus the out-of-plane component only grows in extensile systems.

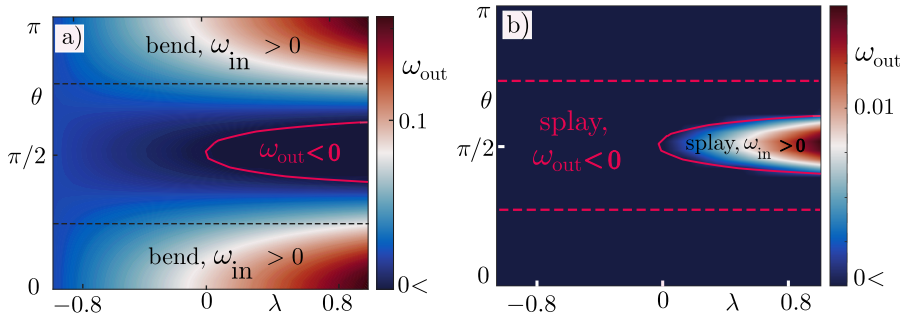

Figure 7.1: a) Results of linear stability analysis as a function of the tumbling parameter λ for an extensile system. The out-of-plane component of the perturbation grows for all values of the tumbling parameter. The solid lines show places in which $\omega_{out} = 0$. These lines separate the region in which ω_{out} is positive (out-of-plane perturbations grow) from regions where ω_{out} is negative (out-of-plane perturbations die). The dashed lines separate splay perturbations ($\pi/4 < \theta < 3\pi/4$) from bend perturbations ($\theta < \pi/4$ and $\theta > 3\pi/4$). b) Results of linear stability analysis as a function of the tumbling parameter λ for a contractile system. The out-of-plane component of the perturbation only grows for large positive values of the tumbling parameter and for a specific interval in θ.

We now study the role of the flow-aligning parameter λ in the growth of the perturbations. In agreement with 2D active nematic systems, **Eq. 7.4** shows that increasing the tumbling parameter increases the growth rate of bend perturbations in extensile systems and decreases the growth rate of splay perturbations in contractile systems [141, 159]. The role of the tumbling parameter in the growth rate of out-of-plane perturbations is more complex, and as such, we represent this in **Fig. 7.1**(a) and (b) for extensile and contractile systems, respectively.

Fig. 7.1(a) shows that in extensile systems, in the regimes where bend perturbations grow, the out-of-plane perturbations always grow ($\omega_{out} > 0$) independent of the value of the tumbling parameter λ.

Fig. 7.1(b) shows that in contractile systems the growth rate of the out-of-plane component of the perturbation is negative in most regions of the phase space except for large positive values of the tumbling parameter, in which $\omega_{out} > 0$ for a specific range of θ.

To summarise, linear stability analysis of the quasi-2D system around a state with in-plane nematic order shows that extensile and contractile systems behave differently when director perturbations perpendicular to the layer are allowed: while extensile

systems promote the growth of both in-plane and out-of-plane perturbations, contractile systems only lead to the growth of director perturbations inside the plane.

7.2.2 Numerical simulation of quasi-2D system

In this subsection, we use numerical simulations of the nematohydrodynamic equations to study the dynamics of the quasi-2D system.

We consider the quasi-2D system to be in the x-y plane, and start the simulations with a director that is along the x axis, along with a small 3D perturbation. The in-plane and out-of-plane perturbations are defined as $\delta\phi_{in} = 2\pi\chi_{in}$ and $\delta\phi_{out} = (\pi/2)\chi_{out}$, respectively. Both in-plane (χ_{in}) and out-of-plane noise (χ_{out}) are taken from a uniform distribution over the interval $[-1/10, 1/10]$. Out-of-plane noise was not added in previous studies which considered 2D behaviour of active systems [63, 66, 160, 161].

In the simulations, the density is taken as constant $\rho = 1$ and we choose values of the parameters which reproduce active turbulence in a 2D system: $\Gamma = 0.7$, $K = 0.01$, $\eta = 2/3$, $\lambda = 0$, $\mathcal{A} = 0$, $\mathcal{B} = -0.3$, $\mathcal{C} = 0.3$, $-0.02 < \zeta < 0.02$ and the system size is 200×200.

In **Fig. 7.2** we compare the behaviour of an extensile system with activity $\zeta > 0$ with that of a contractile system with $\zeta < 0$. The figure shows that contractile stresses suppress perturbations of the director field in the direction perpendicular to the layer, leading to the usual 2D active dynamics (**Fig. 7.2**(a), inset). In extensile systems, however, the director has non-zero out-of-plane components except within dynamic, elongated domains (**Fig. 7.2**(a)).

This behaviour is quantified in **Fig. 7.2**(b) where we plot the area fraction of the regions where the director points out of the plane, as a function of activity, showing that this quantity remains zero for the contractile case, but increases with activity in extensile systems. Here, we consider lattice sites in which the director makes an angle more than 10° with the 2D layer as an out-of-plane site, and define the area fraction Φ as the ratio of out-of-plane sites to the total number of the sites in the system.

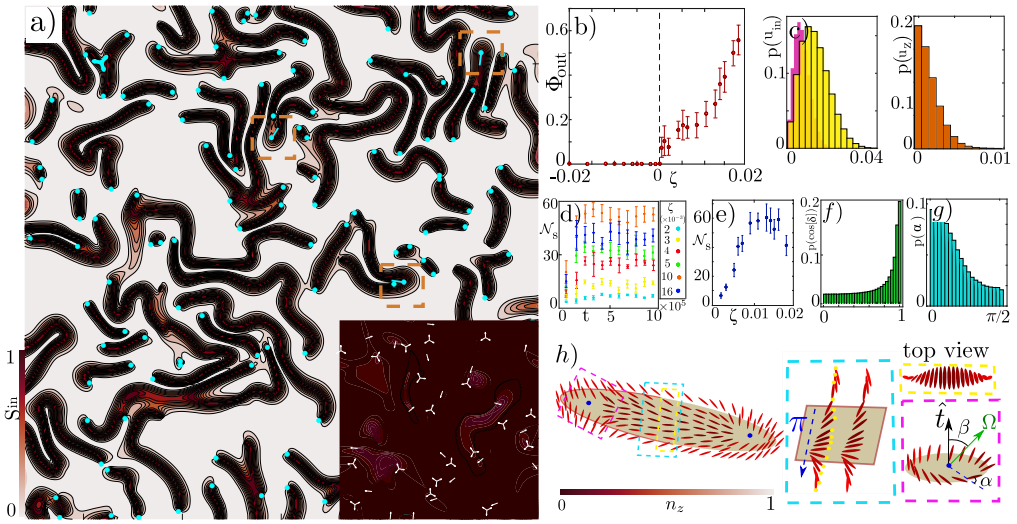

Figure 7.2: Snapshots from simulations of 2D active nematics layers. Colour denotes the magnitude of the in-plane order ($S_{in} = [1 - n_z^2]^{1/2}$) from in-plane (black) to out-of-plane (white): a) extensile stress, defects in cyan. 3D twist-type defects are represented by circles. Inset: contractile stress, 2D $\pm 1/2$ topological defects are shown in white. b) Area fraction of regions with out-of-plane director as a function of activity. The average is taken in the steady state every 2×10^4 timesteps, over 10 datapoints. c) In-plane, $u_{\rm in}$, and out-of-plane, u_z, speed for contractile (yellow, $u_z = 0$) and extensile (pink, orange) driving. d) Variation of the number of snakes $\mathcal{N}_s$ with time. The average is taken over 5 data points in a 10^5 time-step interval. e) Number of snakes as a function of activity at steady state. The average is taken in the steady state every 2×10^4 timesteps, over 10 datapoints. f) Distribution of the angle between the director and the tangent to the boundary of snakes. The histogram peaks at $\cos(\delta) = 1$, indicating parallel alignment of the director with the boundary. g) Distribution of the angle α in extensile systems. h) Director in a snake. Cyan outline: moving along the blue dashed arrow, crossing the width of a snake, the director twists by π. Yellow outline: top view of the director across the width of a snake. Magenta outline: 3D twist-type defects are commonly found at the ends of the snakes. The blue circle shows the core of the defect, $\hat{t}$ represents the normal to the layer, and the blue dashed line connects the center of the twist-type defect to the position with an in-plane director. α is the angle between this line and the local director. The director rotates out of the plane around the rotation vector Ω to form the twist defect.

Histograms of the corresponding in-plane and out-of-plane flow fields are shown in **Fig. 7.2**(c). In contractile systems flows remain in the x-y plane whereas in the extensile case, the flow develops substantial components along z which act to drive the director into the third dimension.

We now study the elongated domains where the director field remains in the x-y plane. These initially form in regions of splay distortion where the flow fields along the z axis are insufficiently strong to push the director field out of the plane.

For convenience, we will refer to the in-plane domains as *snakes*. These are twist walls, also called π-walls, in the liquid crystal literature.

To study the statistical properties of the snakes in the simulations, we need to define them more quantitatively. We consider lattice sites in which the director makes an angle less than 10° with the 2D layer as an in-plane site. To find the number of snakes, we attribute a value 1 (0) to in-plane (out-of-plane) sites. We define the boundary of the snakes as in-plane sites which have at least one out-of-plane neighbouring site. A snake is then defined as connected sites with a value 1.

After a transient phase, the average number of snakes fluctuates around a constant value (**Fig. 7.2**(d)) which first increases and then decreases with increasing activity (**Fig. 7.2**(e)). This reflects a balance between snakes elongating and then breaking up, and the possibility that local flows will be sufficiently strong to destroy a snake by pushing the director out of the x-y plane.

To understand how the snakes lengthen and divide we study their director and flow fields. We first measure $\cos\delta$, the angle between the orientation of the director at the boundary of a snake and the local tangent to the boundary. The histogram of $\cos\delta$, shown in **Fig. 7.2**(f) peaks at $\cos\delta = 1$, showing that the director inside a snake tends to align parallel to its elongation direction.

Therefore, along the boundaries of a snake the director rotates through $\pi/2$ to match the surrounding vertical director configuration (**Fig. 7.2**(h)) and as a result, looking at a cross-section across the width of a snake, the director twists by π (cyan and yellow outlines in **Fig. 7.2**(h)). At the ends of the snake, this results in twist defects with the director configuration shown in the magenta outline in **Fig. 7.2**(h).

An angle that characterises twist defects is α, the angle between the line which connects the center of the defect to the position of the in-plane director and the direction of the in-plane director itself (magenta outline in **Fig. 7.2**(h)). It has been shown that tangential twist is more predominant in extensile defect loops [151]. However, for the point-like defects in our quasi-2D system, **Fig. 7.2**(g) shows that α has a peak at $\alpha = 0$, indicating that the twist-type defects are predominantly radial.

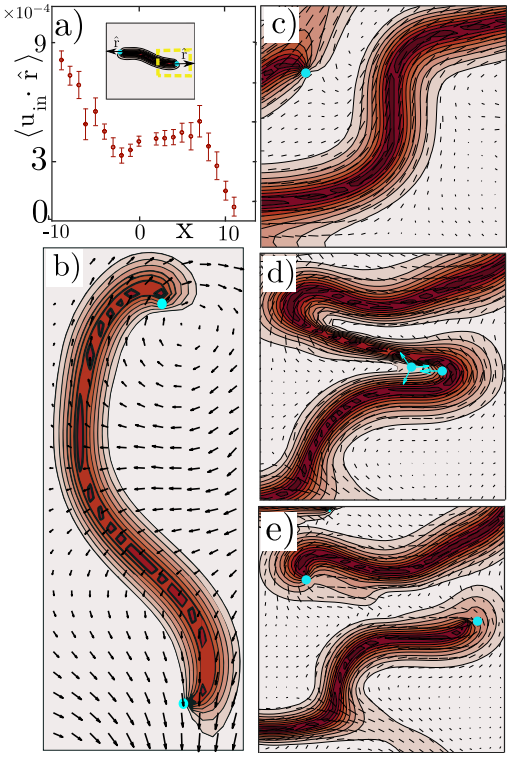

Figure 7.3: a) Average flow along the direction of the elongation of snakes (measured at the ends, i.e., within the yellow box). The origin corresponds to the blue dot and $x > 0$ always corresponds to the outside of the snake. $\langle \mathbf{u}_{in} \cdot \hat{r} \rangle > 0$, indicating that active flows elongate the snakes. b) Flows around a snake. c)-e) Evolution of a snake. Elongated snakes undergo a bend instability and form defects. The director then moves to the third direction dividing the snake into two with twist-type defects at their ends.

We are now in a position to understand the dynamics of a snake. The stresses which result from the twist defects set up flows that act to elongate the snakes and to align the director field inside them. To find the average flow at the end of the snakes, we take $\hat{r}$ (introduced in **Fig. 7.3**(a)) to be along the local direction of the elongation of the snakes, pointing outwards, and average the flow over the 10 lattice sites next to the end and in the direction of $\pm\hat{r}$. We ignore snakes smaller than 20 lattice units, as small snakes usually shrink and form vertical regions. **Fig. 7.3**(a) shows the average flow at the end of the snakes. The average is taken over the flows at the end of different snakes every 10^4 timesteps over a 2×10^5 interval. **Fig. 7.3**(b) shows the flows around a snake.

The ensuing evolution is illustrated in Figs. 7.3(c)-(e). Since the system is extensile and the director is parallel to their length, the elongated snakes

undergo a bend instability. The growth of a bend deformation is equivalent to the formation of a pair of two-dimensional, $\pm 1/2$ defects (orange outlines in **Fig. 7.2**(a) and **Fig. 7.3**(c)-(e)). In agreement with **Eq. 7.6**, that bend deformations are unstable to director perturbations perpendicular to the layer and, due to the large bend deformations at the position of the defects, the director rotates out of the plane and the snake splits into two smaller snakes terminated by twist director configurations (**Fig. 7.2**(h)).

7.3 Relation to 3D active turbulence

In this section, we show that the behavior that we have identified in the quasi-2D system persists in three dimensions.

To compare defect type distribution in 3D with our quasi-2D system, we perform simulations in fully three-dimensional systems where the simulation box is also three dimensional ($120 \times 120 \times 120$ LB units) and there is a periodic boundary condition on all three directions. Figures 7.4(a) and 7.4(b) compare the distribution of the twist angle β for the quasi-2D system to the simulations of the full 3D active turbulence keeping the activity the same and considering both extensile and contractile systems. The figure shows that similar behaviour is observed in both 2D and 3D: in contractile systems defects are predominantly two-dimensional, whereas, in the extensile system, there is a clear preference for introducing twist defects. To understand the formation

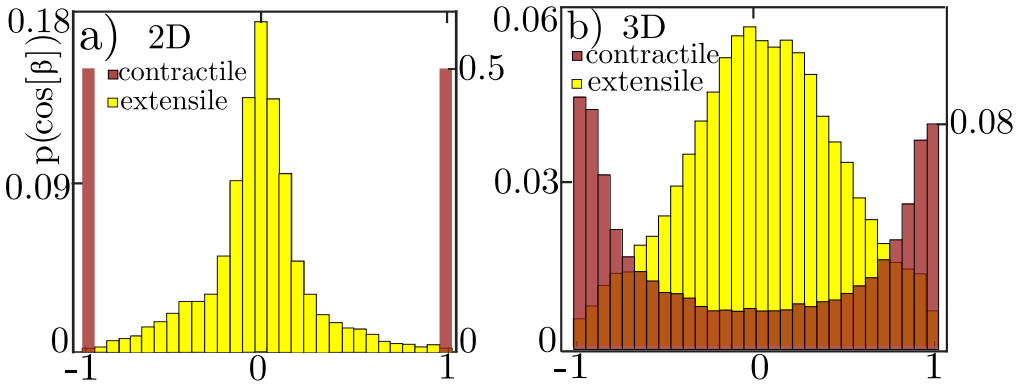

Figure 7.4: Twist angle β in (a) 2D, (b) 3D. In extensile systems, most defects are twist-type ($\beta = \pi/2$) while in contractile systems most defects are wedge-type ($\beta = 0, \pi$). Right/left axis shows $p(\cos[\beta])$ in the contractile/extensile system.

of twist perturbations in 3D, in the following subsection, we perform linear stability analysis and study the growth of twist perturbations in three dimesnions.

7.3.1 Evolution of twist perturbations in 3D active turbulence

To further understand the distinct behaviour of extensile and contractile systems, we now study the evolution of twist perturbations in 3D systems deep in the nematic phase where $S \approx 1$. Twist perturbations are defined as $\epsilon_{ikl} Q_{ij} \partial_k Q_{lj}$ [162], where ϵ_{ikl} is the Levi-Civita symbol. Without loss of generality, we consider the direction of the nematic order to be along the x axis, and use the nematohydrodynamic equations to find the dynamics of the perturbations in the zero Reynolds number regime. Considering an ordered phase along the x axis means that to study the evolution of twist perturbations at linear order, we need to study the evolution of $\partial_y \delta Q_{zx} - \partial_z \delta Q_{yx}$. In the ordered phase and at the linear level the dynamics of δQ_{yx} and δQ_{zx} are given by

$$\partial_t \delta Q_{yx} = \frac{7\lambda}{6} E_{yx} + \frac{3}{2}\Omega_{yx} + \Gamma K \nabla^2 \delta Q_{yx}, \tag{7.7}$$

$$\partial_t \delta Q_{zx} = \frac{7\lambda}{6} E_{zx} + \frac{3}{2}\Omega_{zx} + \Gamma K \nabla^2 \delta Q_{zx}. \tag{7.8}$$

After substituting the components of the strain rate tensor $\boldsymbol{E}$ and vorticity tensor $\boldsymbol{\Omega}$ into Eqs. 7.7, and 7.8 and subtracting these equations, the dynamics of the twist reads

$$\partial_t(\partial_y \delta Q_{zx} - \partial_z \delta Q_{yx}) = (\frac{3}{4} + \frac{7\lambda}{12})(\partial_y \partial_x \delta u_z - \partial_x \partial_z \delta u_y) + K\Gamma \nabla^2 (\partial_y \delta Q_{zx} - \partial_z \delta Q_{yx}). \tag{7.9}$$

We can then find the velocity field from the Stokes equation in Fourier space, and substitute it into **Eq. 7.9**. This gives a closed form for the growth rate of the twist perturbation

$$\omega_{twist} = \frac{\zeta}{4\eta}(3 + \frac{7\lambda}{3}) \cos^2\theta - \Gamma K q^2, \tag{7.10}$$

where we have defined $\mathbf{q} \cdot \hat{x} = q \cos\theta$. The first term in the growth rate is an active term proportional to the activity coefficient ζ. This term is positive (negative) for

extensile (contractile) systems. As a result, extensile (contractile) activity promotes (suppresses) twist perturbations. The second term is a passive term and shows that the elastic constant tends to suppress the twist deformations. The twist perturbations grow when $\zeta(3+7\lambda/3)q^2\cos^2\theta/(4\eta) > \Gamma K q^4$. This shows that at a linear level, twist deformations can be formed only in extensile systems.

7.3.2 Active growing droplets

To more explicitly investigate the role of active extensile and contractile flows on 3D growth, we performed 3D simulations on an initially planar, $2D$ growing drop embedded in a 3D passive fluid. Stabilising this setting is hard numerically as surface tension tends to form a 3D spherical droplet. Here, we choose values of surface tension K_ϕ, and elastic constant K_Q that do not lead to the formation of a spherical droplet in the time scale of the simulation.

The growth is introduced by increasing the concentration of active material by a rate k_d. Here, we ignore the effect of the growth in producing incompressible flows, assuming that those are smaller than active flows. 3D views of the drop at $\bar{t} = t\zeta/\eta = 210$ (where η is viscosity) are shown in Figs. 7.5(a) and (b) for contractile and extensile systems, respectively. The black outline shows the boundary of the drop in the initial 2D plane and the out-of-plane concentration is represented in green. The red background colour shows the speed perpendicular to the layer, $|u_z|$. In the contractile system, the out-of-layer velocity is negligible and the growth is mainly in the plane. By contrast, the extensile drop has non-zero velocity perpendicular to the layer and grows into the third dimension. This behaviour is confirmed more quantitatively in **Fig. 7.5**(c) which shows the evolution of $\mathcal{N}^*$, the difference between the number of out-of-plane particles in an active growing system and in a passive growing system. $\mathcal{N}^*$ is defined as $N^a_{out} - N^p_{out}$, where N^a_{out} and N^p_{out} are the number of out-of-plane particles in an active and a passive growing system, respectively. We find these numbers by multiplying the concentration in each out-of-plane grid by the grid volume (which is equal to one in our system), and then summing over the number of particles in different grids. $\mathcal{N}^*$ is positive

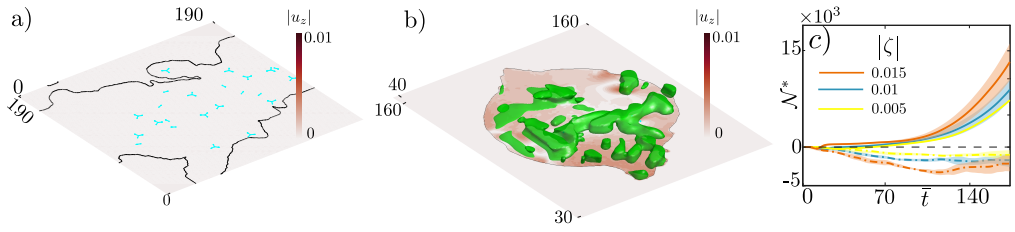

Figure 7.5: 3D views of a growing drop with (a) contractile, (b) extensile activities. Defects are represented in cyan, green shows the out-of-plane concentration and the red shading indicates out-of-plane speed. (Note (b) is a close-up). (c) The difference in the number of out-of-plane particles in an active growing system ($\zeta \neq 0$) and in a passive growing system ($\zeta = 0$) for extensile (solid lines) and contractile (dashed-dotted lines) activity. The semi-transparent colours show error bars calculated using the standard deviation from five simulations.

(negative) in extensile (contractile) systems showing that extensile (contractile) flows promote (suppress) growth to the third direction.

7.4 Summary

To summarise, in an extensile (contractile) system there is a positive (negative) feedback between out-of-plane flows and out-of-plane director orientation and as a result, out-of-plane perturbations grow (are suppressed) in extensile (contractile) systems. The transition from 2D to 3D director orientation is often a vital step in biological processes. Biofilm formation can be initiated by cells turning to point perpendicular to a substrate [33, 153, 163, 164] which leads to a planar-to-bulk transition [165]. This has been described in terms of mechanical instabilities due to cell divisions which cause extensile stresses [165–167] and the mechanism we describe here supports this interpretation.

Fully-developed 3D active turbulence is characterised by motile disclination lines that form closed loops that can appear, grow, shrink, and disappear [53, 151, 152]. Experiments and simulations have shown that twist (wedge) type defects are more common in extensile (contractile) systems which can be explained by our model [53, 152].

It is so hard to leave—until you leave. And then it is the easiest thing in the world.

John Green

8 Discussion

In this thesis, we used a continuum approach to explore the role of active stress in the collective behaviour of living systems. This behaviour ranges from the creation of defects and disclination lines in two and three dimensions, large-scale defect ordering in the presence of friction with a substrate, and formation of fractal-type patterns at the interface of a bacterial droplet, to cell elongation and the emergence of nematic order due to activity, and generation of extensile and contractile regions in living tissues.

We summarise the main findings in section 8.1 and provide an outlook for ongoing and future research in section 8.2.

8.1 Summary

In Chapter 3 we investigated the behaviour of topological defects in two-dimensional active systems in contact with a frictional substrate. We found that increasing friction leads to different defect ordering in systems that form an isotropic and a nematic phase without activity:

(i) In systems that form an isotropic phase without activity, increasing friction leads to the nematic ordering of defects. This can be understood by minimising the

elastic free energy of two pairs of $\pm 1/2$ defects and finding the optimum respective orientation of the defect pairs [101].

(ii) In systems with a nematic ground state, we found that increasing friction leads to the formation of arches, polar structures in the director field, and the arches align $+1/2$ defects and lead to polar ordering of the defects. We showed analytically that in a nematic phase with large friction, arches are the steady-state solution of the nematohydrodynamic equations [105].

In chapter 4 we introduced a model to understand the periodic pattern of protrusions at the interface of bacterial droplets and a fractal-type pattern that is later formed. The model accounts for the fact that in the experiments the bacterial suspension forms a gel at the center and the magnitude of the nematic order decreases towards the center of the droplet [79]. This allows for the formation of periodic patterns guided by the creation and motion of $+1/2$ defects in a layer with large nematic order around the interface. In agreement with the experiments, the model predicts that the period of the pattern is not affected by the droplet curvature, but is set by the active length scale which is an intrinsic length-scale in the system, and is proportional to $\sqrt{K_Q/\zeta}$. Consistent with the experiments, we found that the amplitude of the protrusions increases with the interface curvature. This is because places with larger curvature have larger bend deformation which leads to larger active forces and flows. Finally, we showed that the fractal-type patterns that form in the experiments are caused by active nematic instabilities: when a protrusion grows due to the motion of a $+1/2$ defect, it forms an elongated arm (protrusion) that has nematic order. However, nematic order is unstable and leads to the formation of new defects and protrusions in the arm. As a result of several consecutive instabilities, we recover the formation of the fractal-type pattern.

In Chapter 5, we started with individual cell-cell active interactions in a confluent monolayer and built a continuum description for the monolayer in terms of cell orientation, cell anisotropy, cell area and cell velocity. We showed that both extensile and contractile active neighbour-neighbour interactions allow the cells to overcome the free energy barrier for elongation. The mechanism of the elongation is different

in extensile and contractile systems. While in contractile systems cells line up with the neighbours, in extensile systems, cells align perpendicular to their neighbours. We explain that these alignments lead to elongation of the cells in both cases. Our continuum model produces different phases in a monolayer including extensile and contractile active turbulence, a stable jammed phase with isotropic cells, a stable nematic phase with elongated cells, and a capped line phase observed in simulations of phase field models.

In active nematic theories, the direction of the active force is normally considered to be along the cell orientation. By decoupling the dynamics of the cell elongation and active force, we showed that defects in the force field do not necessarily orient along and positionally coincide with defects in the cell orientation field.

In chapter 6, we investigated the relationship between cell shape and cell-generated stresses in confluent cell layers. Analysing experimental data on shape orientation and contractile stress in MDCK and LP-9 colonies, we reported the emergence of correlated, dynamic domains in which misalignment between the directors defined by cell shape and by contractile forces reaches up to 90°, effectively creating extensile domains in a monolayer of contractile cells. To understand this misalignment, we used the continuum model that we introduced in chapter 5. The model allowed us to recover the spatial and temporal correlations in the cell and stress orientation, the distribution of the misalignment angle, and the positioning of defects with respect to the interface between extensile and contractile regions.

Finally, in chapter 7 we used numerical simulations and linear stability analysis to study an active nematic system in a 2D plane, where the director is allowed to point out of the plane. Our results highlight the difference between extensile and contractile systems in three dimensions. Contractile stress suppresses the flows perpendicular to the quasi-2d layer and favors in-plane orientations of the director. By contrast, extensile stress promotes instabilities that can turn the director out of the plane, leaving behind a population of distinct, in-plane regions that continually elongate and divide. This supports extensile forces as a mechanism for the initial stages of layer formation in living systems, and we show that a planar

drop with extensile (contractile) activity grows into three dimensions (remains in two dimensions). The results also explain the propensity of disclination lines in three-dimensional active nematics to be of twist type in extensile or wedge type in contractile materials.

8.2 Outlook

In this thesis, we have seen several examples in which developing a continuum active nematic model that considers key features of experiments can be helpful in understanding the behaviour of biological systems. However, numerous research questions remain unanswered. Here, we introduce some of these questions.

What are the flow patterns that form in 3D droplets on top of a substrate?

In Chapter 4, we showed that the presence of an active layer at the interface of a 2D droplet leads to the formation of periodic patterns of protrusions. The next step would be to extend this to three-dimensional droplets on a substrate and investigate the three-dimensional flows at the interface of the droplet. Since the height of the droplet decreases towards the interface, one would expect that friction with the substrate is more effective in suppressing chaotic flows at the edge compared to the center. This could lead to the taming of the active flows and the formation of patterns of three-dimensional rotating flows at the interface. In a general setting, one would investigate the role of the morphology of the droplet (wetting angle), and activity patterns (width of the active layer at the interface) on the invasion of the active material to its surroundings.

What are the dominant cell shapes in living tissues?

In Chapter 5 of this thesis, we approximated the shape of living cells with an elongated ellipse. During many important life processes such as morphogenesis and epithelial jamming, cells show a variety of shapes and this has an important effect on the active force that they exert on their surrounding cells and on their mobility [27, 30]. As a result, exploring the interplay between active forces and cell morphology in a broader model accommodating diverse cell shapes would be a

fascinating avenue for research. It would also be interesting to study the effect of external stress, such as tissue stretching, on the shape of the cells.

Do active disclination lines form any sort of ordering in 3D?

In chapter 3 of this thesis, we showed that increasing friction with a substrate in a 2D system could lead to defect ordering. It is not clear if such an orientational, and/or positional ordering could be observed in three-dimensional disclination lines. In three dimensions, frictional damping with the substrate becomes less important, but one can still think of a length scale over which the active flows damp. This could be caused by the presence of heterogeneities in a three-dimensional cell culture for example, or due to solid-like structures in the membranes of the cells. The first step would be to simply consider a three-dimensional frictional damping $-\gamma\mathbf{u}$ in the Navier-Stokes equation, and compare the behaviour of disclination lines as the frictional damping length increases with respect to the active length-scale.

How does viscoelasticity change the behaviour of active systems?

In this thesis, we ignored the effects related to viscoelasticity and modeled living systems as a viscous fluid. However, many biological systems, such as living tissues or bacterial suspensions, exhibit viscoelastic behaviour on short time scales. This enables these systems to preserve a fundamental structural integrity due to their solid-like characteristics, while simultaneously allowing for dynamic rearrangements into various configurations due to their viscous properties.

There are several questions that can be addressed here. It would be interesting to study the role of viscoelasticity in the interaction between defects and disclination lines, and in the velocity and the direction of the motion of defects.

Another direction is to look at the interfacial patterns in bacterial droplets. In the experiments that we introduced in chapter 5, bacteria form a gel at the center of the droplet. This is an evidence that viscoelastic properties could be relevant for understanding some features of these experiments. It would be helpful to study the effects of viscoelasticity in this setup, and in particular to see if it could stabilise the protrusions in the simulations for a longer time, in line with the observations in

the experiments.

We have proposed several future research directions, including the exploration of cell shape variations under different experimental conditions, the role of flow screening on the positional and orientational ordering of disclination lines in three dimensions, the role of droplet morphology in flow patterns in active suspensions, and the effect of viscoelasticity on the motion of defects and interface deformations in active droplets.

Appendices

I think perfection is ugly. Somewhere in the things humans make, I want to see scars, failure, disorder, distortion.

Yohji Yamamoto

A

Bend, splay, and twist elastic free energy

In systems in which the elastic constants are not equal, the elastic free energy can be written as

$$\mathcal{F}_g = \frac{L_1}{2}\partial_k Q_{ij}\partial_k Q_{ij} + \frac{L_2}{2}\partial_k Q_{kj}\partial_i Q_{ij} + \frac{L_3}{2}\partial_i Q_{jk}\partial_k Q_{ij}, \tag{A.1}$$

where the terms with coefficients L_i are elastic terms, associated with the energy cost of director distortions [48, 168]. The last term in Eq. A.1 is zero when the system has a periodic boundary condition.

The distortions in nematic liquid crystals are generally divided into three groups: splay $K_{\text{Splay}}(\vec{\nabla}\cdot\boldsymbol{n})^2$, bend $K_{\text{Bend}}(\boldsymbol{n}\times(\vec{\nabla}\times\boldsymbol{n}))^2$, and twist deformations $K_{\text{Twist}}(\boldsymbol{n}\cdot(\vec{\nabla}\times\boldsymbol{n}))^2$. These are shown in **Fig. A.1**.

Assuming a constant magnitude of the order, one can use **Eq. A.1** to find the bend, splay, and twist elastic constants K_i [169]

$$\begin{aligned}
\frac{2K_{\text{Bend}}}{9S_0^2} &= L_1 + \frac{L_2}{2},\\
\frac{2K_{\text{Twist}}}{9S_0^2} &= L_1,\\
\frac{2K_{\text{Splay}}}{9S_0^2} &= L_1 + \frac{L_2}{2}.
\end{aligned} \tag{A.2}$$

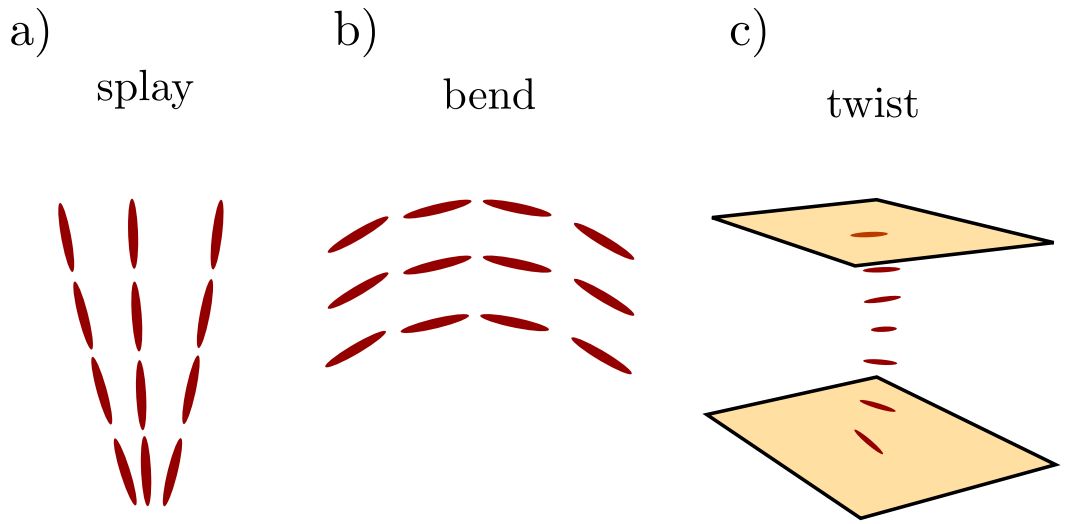

Figure A.1: Schematic representation of three types of director deformations: splay, bend, and twist. Splay and bend distortions can exist in two dimensions, but twist deformations only appear in three dimensions.

In using **Eq. A.2**, one needs to be careful to choose values of L_i so that the bend, splay, and twist elastic constants become positive. This is to penalise deformations in the nematic system [48].

In chapter 7 we study the growth of twist perturbations in three dimensions as a result of extensile flows. In the rest of this thesis, a one-elastic constant approximation has been used (**Eq. 2.4**).

No change of circumstances can repair a defect of character.

Ralph Waldo Emerson

B Defect detection

B.1 2D topological defects

In our 2d simulations, we use a two-dimensional square grid. To find the position of defects, we calculate the winding number for all sets of neighbouring lattice points which form a two-by-two square. As we go around the square clockwise, if the director changes its orientation by $\pm\pi$, we define the position of $\pm 1/2$ defects at the intersection of the four lattice sites.

B.2 Disclination lines

To find defect positions of disclination lines in a three-dimensional simulation, we extended our two-dimensional calculations to three dimensions, meaning we calculate the winding number in all sets of four lattice sites forming a two-by-two square in x-z, x-y and y-z planes. To find the rotation of the director as we turn around the square, we project the director to the three-dimensional orientation space (**Fig. B.1**) at every lattice point. Since we are working with nematic liquid crystals, there are two corresponding projections $\pm n$ associated with the director in each lattice point. We walk clockwise around the four neighbours' director projection, and at every step, we take the next closest director configuration (**Fig. B.1**). Upon returning to the initial starting point, we either regain the original director orientation (Figure

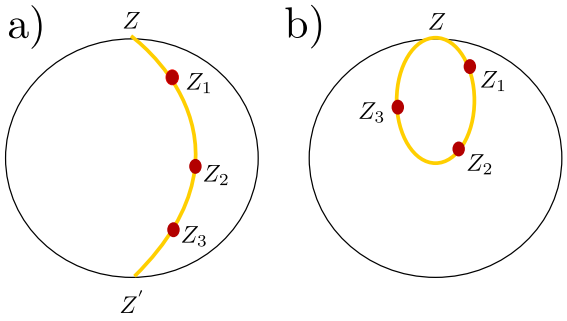

Figure B.1: Detection of disclination lines. The representation of the director in the three-dimensional spherical space. Since we are working with a nematic liquid crystal, the director has two projections $\pm n$. While moving clockwise around a two-by-two lattice square, we establish the initial director as the origin Z on the upper half sphere. Subsequently, we proceed to the position Z_1 of the director on the adjacent lattice site, consistently selecting the new director projection with the least angular deviation from the preceding one. This results in a closed walk from along Z_is, and subsequently either returning to Z (b) or reaching its corresponding point Z' on the lower half sphere (a). If the outcome is Z', it signifies the passage of a half-integer disclination through the four lattice sites. Image is adapted from [170], and modified.

B.1b) or find ourselves on the opposite side of the orientation sphere (Figure B.1a). In the latter case, a half-integer disclination line has traversed this two-by-two grid, establishing a disclination core at the center of the four points. Conversely, in the former scenario, the absence of a disclination line indicates either the absence of disclination or the passage of a full disclination line.

The rotation axis of the defect Ω is defined as the average of the outer product of pairs of directors around the defect.

To find the defect angle α for twist-type defects, we consider a 3×3 square around the defect and find the neighboring site with the largest in-plane director component. We then define α as the angle between the line which connects the center of the defect to this site, and the director orientation at the site.

In the manuscript, we refer to defects as $2D$ ($3D$) defects when $|\cos\beta| > 0.95$ ($|\cos\beta| < 0.95$), where β is the twist angle.

Bibliography

1. Marchetti, M. C., Joanny, J. F., Ramaswamy, S., Liverpool, T. B., Prost, J., Rao, M. & Simha, R. A. Hydrodynamics of soft active matter. *Rev. Mod. Phys.* **85,** 1143–1189 (2013).
2. Gompper, G., Winkler, R. G., Speck, T., Solon, A., Nardini, C., Peruani, F., Lowen, H., Golestanian, R., Kaupp, U. B., Alvarez, L., *et al.* The 2020 motile active matter roadmap. *J. Phys. Condens.* **32,** 193001 (2020).
3. Ramaswamy, S. The mechanics and statistics of active matter. *Annu. Rev. Cond. Mat. Phys.* **1,** 323–345 (2010).
4. Bowick, M. J., Fakhri, N., Marchetti, M. C. & Ramaswamy, S. Symmetry, Thermodynamics, and Topology in Active Matter. *Phys. Rev. X* **12,** 010501 (1 2022).
5. Popkin, G. The physics of life. *Nature* **529,** 16 (2016).
6. Paluch, E. K. Biophysics across time and space. *Nat. Phys* **14,** 646–647 (2018).
7. Trepat, X. & Sahai, E. Mesoscale physical principles of collective cell organization. *Nat. Phys* **14,** 671–682 (2018).
8. Bain, N. & Bartolo, D. Dynamic response and hydrodynamics of polarized crowds. *Science* **363,** 46–49 (2019).
9. Ling, H., Mclvor, G. E., van der Vaart, K., Vaughan, R. T., Thornton, A. & Ouellette, N. T. Local interactions and their group-level consequences in flocking jackdaws. *Proc. Royal Soc. B* **286,** 20190865 (2019).
10. Papadopoulou, M., Hildenbrandt, H., Sankey, D. W., Portugal, S. J. & Hemelrijk, C. K. Self-organization of collective escape in pigeon flocks. *PLoS Comput. Biol.* **18,** e1009772 (2022).
11. Giardina, I. Collective behavior in animal groups: theoretical models and empirical studies. *HFSP journal* **2,** 205–219 (2008).
12. Sumpter, D. J. *Collective animal behavior* (Princeton University Press, 2010).
13. Lange, J. R. & Fabry, B. Cell and tissue mechanics in cell migration. *Experimental cell research* **319,** 2418–2423 (2013).
14. in. *Cell Movement in Health and Disease* (eds Schnoor, M., Yin, L.-M. & Sun, S. X.) 85–100 (Academic Press, 2022).
15. Allen, G. M., Lee, K. C., Barnhart, E. L., Tsuchida, M. A., Wilson, C. A., Gutierrez, E., Groisman, A., Theriot, J. A. & Mogilner, A. Cell mechanics at the rear act to steer the direction of cell migration. *Cell Syst.* **11,** 286–299 (2020).
16. Wolpert, L. Pattern formation in biological development. *Sci. Am.* **239,** 154–165 (1978).

17. Mietke, A., Jemseena, V, Kumar, K. V., Sbalzarini, I. F. & Jülicher, F. Minimal model of cellular symmetry breaking. *Phys. Rev. Lett.* **123,** 188101 (2019).

18. Koch, A.-J. & Meinhardt, H. Biological pattern formation: from basic mechanisms to complex structures. *RMP* **66,** 1481 (1994).

19. Eckmann, J.-P., Feinerman, O., Gruendlinger, L., Moses, E., Soriano, J. & Tlusty, T. The physics of living neural networks. *Phys. Rep.* **449,** 54–76 (2007).

20. Wright, J. & Liley, D. Dynamics of the brain at global and microscopic scales: Neural networks and the EEG. *Behav Brain Sci* **19,** 285–295 (1996).

21. Purcell, E. M. Life at low Reynolds number. *Am. J. Phys.* **45,** 3–11 (1977).

22. Qiu, T., Lee, T.-C., Mark, A. G., Morozov, K. I., Münster, R., Mierka, O., Turek, S., Leshansky, A. M. & Fischer, P. Swimming by reciprocal motion at low Reynolds number. *Nat. Commun* **5,** 5119 (2014).

23. Volfson, D., Cookson, S., Hasty, J. & Tsimring, L. S. Biomechanical ordering of dense cell populations. *PNAS* **105,** 15346–15351 (2008).

24. Li, H., Shi, X.-q., Huang, M., Chen, X., Xiao, M., Liu, C., Chaté, H. & Zhang, H. Data-driven quantitative modeling of bacterial active nematics. *PNAS* **116,** 777–785 (2019).

25. Atia, L., Fredberg, J. J., Gov, N. S. & Pegoraro, A. F. Are cell jamming and unjamming essential in tissue development? *Cells and development* **168,** 1143–1189 (2021).

26. Saw, T. B., Doostmohammadi, A., Nier, V., Kocgozlu, L., Thampi, S., Toyama, Y., Marcq, P., Lim, C. T., Yeomans, J. M. & Ladoux, B. Topological defects in epithelia govern cell death and extrusion. *Nature* **544,** 212–216 (2017).

27. Etournay, R., Popović, M., Merkel, M., Nandi, A., Blasse, C., Aigouy, B., Brandl, H., Myers, G., Salbreux, G., Jülicher, F., *et al.* Interplay of cell dynamics and epithelial tension during morphogenesis of the Drosophila pupal wing. *Elife* **4,** e07090 (2015).

28. Doostmohammadi, A., Thampi, S. P. & Yeomans, J. M. Defect-mediated morphologies in growing cell colonies. *Phys. Rev. Lett.* **117,** 048102 (2016).

29. Tetley, R. J., Staddon, M. F., Heller, D., Hoppe, A., Banerjee, S. & Mao, Y. Tissue fluidity promotes epithelial wound healing. *Nat. Phys.* **15,** 1195–1203 (2019).

30. Atia, L., Bi, D., Sharma, Y., Mitchel, J. A., Gweon, B., A Koehler, S., DeCamp, S. J., Lan, B., Kim, J. H., Hirsch, R., *et al.* Geometric constraints during epithelial jamming. *Nat. Phys.* **14,** 613–620 (2018).

31. Reynolds, C. W. *Flocks, herds and schools: A distributed behavioral model* in *Proceedings of the 14th annual conference on Computer graphics and interactive techniques* (1987), 25–34.

32. Vicsek, T., Czirók, A., Ben-Jacob, E., Cohen, I. & Shochet, O. Novel type of phase transition in a system of self-driven particles. *Phys. Rev. Lett.* **75,** 1226 (1995).

33. Hartmann, R., Singh, P. K., Pearce, P., Mok, R., Song, B., Díaz-Pascual, F., Dunkel, J. & Drescher, K. Emergence of three-dimensional order and structure in growing biofilms. *Nat. Phys.* **15,** 251–256 (2019).

34. You, Z., Pearce, D. J. & Giomi, L. Confinement-induced self-organization in growing bacterial colonies. *Sci. Adv.* **7,** eabc8685 (2021).
35. Toner, J. & Tu, Y. Flocks, herds, and schools: A quantitative theory of flocking. *Phys. Rev. E* **58,** 4828–4858 (1998).
36. Toner, J. & Tu, Y. Long-range order in a two-dimensional dynamical XY model: How birds fly together. *Phys. Rev. Lett.* **75,** 4326–4329 (1995).
37. Dombrowski, C., Cisneros, L., Chatkaew, S., Goldstein, R. E. & Kessler, J. O. Self-concentration and large-scale coherence in bacterial dynamics. *Phys. Rev. Lett.* **93,** 098103 (2004).
38. Sanchez, T., Chen, D. T. N., DeCamp, S. J., Heymann, M. & Dogic, Z. Spontaneous motion in hierarchically assembled active matter. *Nature* **491,** 431–434 (2012).
39. Sumino, Y., Nagai, K. H., Shitaka, Y., Tanaka, D., Yoshikawa, K., Chaté, H. & Oiwa, K. Large-scale vortex lattice emerging from collectively moving microtubules. *Nature* **483,** 448–452 (2012).
40. Doostmohammadi, A., Ignés-Mullol, J., Yeomans, J. M. & Sagués, F. Active nematics. *Nat. Comm.* **9,** 1–13 (2018).
41. Dell'Arciprete, D, Blow, M., Brown, A., Farrell, F., Lintuvuori, J. S., McVey, A., Marenduzzo, D & Poon, W. C. A growing bacterial colony in two dimensions as an active nematic. *Nat. Commun.* **9,** 1–9 (2018).
42. Yaman, Y. I., Demir, E., Vetter, R. & Kocabas, A. Emergence of active nematics in chaining bacterial biofilms. *Nat. Commun.* **10,** 1–9 (2019).
43. Ramaswamy, S., Simha, R. A. & Toner, J. Active nematics on a substrate: Giant number fluctuations and long-time tails. *Europhys. Lett.* **62,** 196 (2003).
44. Kumar, N., Zhang, R., de Pablo, J. J. & Gardel, M. L. Tunable structure and dynamics of active liquid crystals. *Sci. Adv.* **4,** eaat7779 (2018).
45. Balasubramaniam, L., Mège, R.-M. & Ladoux, B. Active nematics across scales from cytoskeleton organization to tissue morphogenesis. *Curr. Opin. Genet. Dev.* **73,** 101897 (2022).
46. Moure, A. & Gomez, H. Phase field modeling of individual and collective cell migration. *Arch. Comput. Methods Eng.* **28,** 311–344 (2021).
47. Mueller, R., Yeomans, J. M. & Doostmohammadi, A. Emergence of active nematic behavior in monolayers of isotropic cells. *Phys. Rev. Lett.* **122,** 048004 (2019).
48. De Gennes, P.-G. & Prost, J. *The physics of liquid crystals* (Oxford university press, 1993).
49. Chaikin, P. M. & Lubensky, T. C. *Principles of condensed matter physics* (Cambridge Univ Press, 2000).
50. Oswald, P. & Pieranski, P. *Nematic and cholesteric liquid crystals: Concepts and physical properties illustrated by experiments* (CRC Press, 2005).
51. Chandrasekhar, S. *Liquid Crystals* (Cambridge University Press, 1980).
52. Vink, R. L. C. Crossover from a Kosterlitz-Thouless phase transition to a discontinuous phase transition in two-dimensional liquid crystals. *Phys. Rev. E* **90,** 062132 (2014).

53. Duclos, G., Adkins, R., Banerjee, D., Peterson, M. S., Varghese, M., Kolvin, I., Baskaran, A., Pelcovits, R. A., Powers, T. R., Baskaran, A., *et al.* Topological structure and dynamics of three-dimensional active nematics. *Science* **367,** 1120–1124 (2020).

54. Beris, A. N. & Edwards, B. J. *Thermodynamics of flowing systems: With internal microstructure* (Oxford University Press, 1994).

55. Marenduzzo, D., Orlandini, E., Cates, M. E. & Yeomans, J. M. Steady-state hydrodynamic instabilities of active liquid crystals: Hybrid lattice Boltzmann simulations. *Phys. Rev. E* **76,** 031921 (2007).

56. Van Horn, B. L. & Winter, H. H. Dynamics of shear aligning of nematic liquid crystal monodomains. *Rheol. Acta* **39,** 294–300 (2000).

57. Aigouy, B., Farhadifar, R., Staple, D. B., Sagner, A., Röper, J.-C., Jülicher, F. & Eaton, S. Cell flow reorients the axis of planar polarity in the wing epithelium of Drosophila. *Cell* **142,** 773–786 (2010).

58. Cahn, J. W. & Hilliard, J. E. Free energy of a nonuniform system. I. Interfacial free energy. *J. Chem. Phys.* **28,** 258–267 (1958).

59. Blow, M. L., Thampi, S. P. & Yeomans, J. M. Biphasic, lyotropic, active nematics. *Phys. Rev. Lett.* **113,** 248303 (2014).

60. Wittkowski, R., Tiribocchi, A., Stenhammar, J., Allen, R. J., Marenduzzo, D. & Cates, M. E. Scalar φ 4 field theory for active-particle phase separation. *Nat. Commun.* **5,** 4351 (2014).

61. Solon, A. P., Stenhammar, J., Cates, M. E., Kafri, Y. & Tailleur, J. Generalized thermodynamics of phase equilibria in scalar active matter. *Phys. Rev. E* **97,** 020602 (2018).

62. Marenduzzo, D., Orlandini, E. & Yeomans, J. M. Hydrodynamics and rheology of active liquid crystals: A numerical investigation. *Phys. Rev. Lett.* **98,** 118102 (2007).

63. Cates, M. E., Henrich, O., Marenduzzo, D. & Stratford, K. Lattice Boltzmann simulations of liquid crystalline fluids: active gels and blue phases. *Soft Matter* **5,** 3791–3800 (2009).

64. Mackay, F., Toner, J., Morozov, A. & Marenduzzo, D. Darcy's law without friction in active nematic rheology. *Phys. Rev. Lett.* **124,** 187801 (2020).

65. Nesbitt, D., Pruessner, G. & Lee, C. F. Uncovering novel phase transitions in dense dry polar active fluids using a lattice Boltzmann method. *New J. Phys.* **23,** 043047 (2021).

66. Carenza, L. N., Gonnella, G., Lamura, A., Negro, G. & Tiribocchi, A. Lattice Boltzmann methods and active fluids. *Eur. Phys. J. E.* **42,** 81 (2019).

67. Thampi, S. P., Doostmohammadi, A., Shendruk, T. N., Golestanian, R. & Yeomans, J. M. Active micromachines: Microfluidics powered by mesoscale turbulence. *Sci. Adv.* **2,** e1501854 (2016).

68. Krüger, T., Kusumaatmaja, H., Kuzmin, A., Shardt, O., Silva, G. & Viggen, E. M. The lattice Boltzmann method. *Springer International Publishing* **10,** 4–15 (2017).

69. Orlandini, E., Cates, M. E., Marenduzzo, D., Tubiana, L. & Yeomans, J. M. Hydrodynamics of active liquid crystals: A hybrid Lattice Boltzmann approach. *Mol. Cryst. and Liq. Cryst.* **494,** 293–308 (2008).
70. Hemingway, E. J., Mishra, P., Marchetti, M. C. & Fielding, S. M. Correlation lengths in hydrodynamic models of active nematics. *Soft Matter* **12,** 7943–7952 (2016).
71. Sulaiman, N, Marenduzzo, D & Yeomans, J. Lattice Boltzmann algorithm to simulate isotropic-nematic emulsions. *Phys. Rev. E* **74,** 041708 (2006).
72. Denniston, C., Marenduzzo, D., Orlandini, E. & Yeomans, J. M. Lattice Boltzmann algorithm for three dimensional liquid crystal hydrodynamics. *Phil. Trans. R. Soc. Lond. A* **362,** 1745–1754 (2004).
73. Simha, R. A. & Ramaswamy, S. Hydrodynamic fluctuations and instabilities in ordered suspensions of self-propelled particles. *Phys. Rev. Lett.* **89,** 058101 (2002).
74. Ramaswamy, S. & Rao, M. Active-filament hydrodynamics: instabilities, boundary conditions and rheology. *New J. Phys.* **9,** 423 (2007).
75. Riley, E. E., Das, D. & Lauga, E. Swimming of peritrichous bacteria is enabled by an elastohydrodynamic instability. *Sci. Rep.* **8,** 1–7 (2018).
76. Ramaswamy, S., Simha, R. A. & Toner, J. Active nematics on a substrate: Giant number fluctuations and long-time tails. *Europhy. Lett. (EPL)* **62,** 196 (2003).
77. Jülicher, F., Grill, S. W. & Salbreux, G. Hydrodynamic theory of active matter. *Rep. Prog. Phys.* **81,** 076601 (2018).
78. Guillamat, P., Ignés-Mullol, J. & Sagués, F. Taming active turbulence with patterned soft interfaces. *Nat. Commun.* **8,** 1–8 (2017).
79. Xu, H., Nejad, M. R., Yeomans, J. M. & Wu, Y. Geometrical control of interface patterning underlies active matter invasion. *PNAS* **120,** e2219708120 (2023).
80. Giomi, L., Bowick, M. J., Mishra, P., Sknepnek, R. & Cristina Marchetti, M. Defect dynamics in active nematics. *Philos. trans., Math. phys. eng. sci.* **372,** 20130365 (2014).
81. Livshits, A., Shani-Zerbib, L., Maroudas-Sacks, Y., Braun, E. & Keren, K. Structural inheritance of the actin cytoskeletal organization determines the body axis in regenerating hydra. *Cell Rep.* **18,** 1410–1421 (2017).
82. Giomi, L. Geometry and topology of turbulence in active nematics. *Phys. Rev. X* **5,** 031003 (2015).
83. Doostmohammadi, A., Shendruk, T. N., Thijssen, K. & Yeomans, J. M. Onset of meso-scale turbulence in active nematics. *Nat. Comm.* **8,** 1–7 (2017).
84. Alert, R., Joanny, J.-F. & Casademunt, J. Universal scaling of active nematic turbulence. *Nat. Phys.* **16,** 682–688 (2020).
85. Thijssen, K., Khaladj, D. A., Aghvami, S. A., Gharbi, M. A., Fraden, S., Yeomans, J. M., Hirst, L. S. & Shendruk, T. N. Submersed micropatterned structures control active nematic flow, topology, and concentration. *PNAS* **118,** e2106038118 (2021).
86. Xu, H., Huang, Y., Zhang, R. & Wu, Y. Autonomous waves and global motion modes in living active solids. *Nat. Phys* **19,** 46–51 (2023).

87. Turiv, T., Koizumi, R., Thijssen, K., Genkin, M. M., Yu, H., Peng, C., Wei, Q.-H., Yeomans, J. M., Aranson, I. S., Doostmohammadi, A., *et al.* Polar jets of swimming bacteria condensed by a patterned liquid crystal. *Nat. Phys* **16,** 481–487 (2020).

88. Ekeh, T., Cates, M. E. & Fodor, E. Thermodynamic cycles with active matter. *Phys. Rev. E* **102,** 010101 (1 2020).

89. Anand, S., Ma, X., Guo, S., Martiniani, S. & Cheng, X. Bacteria Through Obstacles: Unifying Fluxes, Entropy Production, and Extractable Work in Living Active Matter. *arXiv preprint arXiv:2308.08421* (2023).

90. Mori, F., Bhattacharyya, S., Yeomans, J. M. & Thampi, S. P. Viscoelastic confinement induces periodic flow reversals in active nematics. *arXiv preprint arXiv:2307.14919* (2023).

91. Chatterjee, R., Rana, N., Simha, R. A., Perlekar, P. & Ramaswamy, S. Inertia Drives a Flocking Phase Transition in Viscous Active Fluids. *Phys. Rev. X* **11,** 031063 (3 2021).

92. Lauga, E. & Powers, T. R. The hydrodynamics of swimming microorganisms. *Rep. Prog. Phys.* **72,** 096601 (2009).

93. Saintillan, D. Rheology of active fluids. *Annu. Rev. Fluid Mech.* **50,** 563–592 (2018).

94. Reymann, A.-C., Staniscia, F., Erzberger, A., Salbreux, G. & Grill, S. W. Cortical flow aligns actin filaments to form a furrow. *Elife* **5,** e17807 (2016).

95. Guillamat, P., Ignés-Mullol, J. & Sagués, F. Control of active liquid crystals with a magnetic field. *PNAS* **113,** 5498–5502 (2016).

96. Srivastava, P., Mishra, P. & Marchetti, M. C. Negative stiffness and modulated states in active nematics. *Soft Matter* **12,** 8214–8225 (2016).

97. Putzig, E., Redner, G. S., Baskaran, A. & Baskaran, A. Instabilities, defects, and defect ordering in an overdamped active nematic. *Soft Matter* **12,** 3854–3859 (2016).

98. Oza, A. U. & Dunkel, J. Antipolar ordering of topological defects in active liquid crystals. *New J. Phys.* **18,** 093006 (2016).

99. Shankar, S. & Marchetti, M. C. Hydrodynamics of Active Defects: from order to chaos to defect ordering. *Phys. Rev. X* **9,** 041047 (2019).

100. Doostmohammadi, A., Adamer, M. F., Thampi, S. P. & Yeomans, J. M. Stabilization of active matter by flow-vortex lattices and defect ordering. *Nat. Comm.* **7,** 10557 (2016).

101. Thijssen, K., Nejad, M. R. & Yeomans, J. M. Role of Friction in Multidefect Ordering. *Phys. Rev. Lett.* **125,** 218004 (2020).

102. Tang, X. & Selinger, J. V. Orientation of topological defects in 2D nematic liquid crystals. *Soft Matter* **13,** 5481–5490 (2017).

103. DeCamp, S. J., Redner, G. S., Baskaran, A., Hagan, M. & Dogic, Z. Orientational order of motile defects in active nematics. *Nat. Mat.* **14,** 1110–1115 (2015).

104. Patelli, A., Djafer-Cherif, I., Aranson, I. S., Bertin, E. & Chaté, H. Understanding dense active nematics from microscopic models. *Phys. Rev. Lett.* **123,** 258001 (2019).

105. Nejad, M. R., Doostmohammadi, A. & Yeomans, J. Memory effects, arches and polar defect ordering at the cross-over from wet to dry active nematics. *Soft Matter* (2021).

106. Sultan, S. A., Nejad, M. R. & Doostmohammadi, A. Quadrupolar active stress induces exotic patterns of defect motion in compressible active nematics. *Soft Matter* **18,** 4118–4126 (2022).

107. Vafa, F., Bowick, M. J., Shraiman, B. I. & Marchetti, M. C. Fluctuations can induce local nematic order and extensile stress in monolayers of motile cells. *Soft Matter* **17,** 3068–3073 (2021).

108. Turner, L., Zhang, R., Darnton, N. C. & Berg, H. C. Visualization of flagella during bacterial swarming. *J. Bacteriol.* **192,** 3259–3267 (2010).

109. Giverso, C., Verani, M. & Ciarletta, P. Branching instability in expanding bacterial colonies. *J. R. Soc. Interface.* **12,** 20141290 (2015).

110. Du, H., Xu, Z., Anyan, M., Kim, O., Leevy, W. M., Shrout, J. D. & Alber, M. High density waves of the bacterium Pseudomonas aeruginosa in propagating swarms result in efficient colonization of surfaces. *Biophys. J.* **103,** 601–609 (2012).

111. Fauvart, M., Phillips, P, Bachaspatimayum, D, Verstraeten, N., Fransaer, J., Michiels, J. & Vermant, J. Surface tension gradient control of bacterial swarming in colonies of Pseudomonas aeruginosa. *Soft Matter* **8,** 70–76 (2012).

112. Trinschek, S., John, K. & Thiele, U. Modelling of surfactant-driven front instabilities in spreading bacterial colonies. *Soft Matter* **14,** 4464–4476 (2018).

113. Troian, S. M., Wu, X. L. & Safran, S. A. Fingering instability in thin wetting films. *Phys. Rev. Lett.* **62,** 1496–1499 (1989).

114. Daniels, R., Vanderleyden, J. & Michiels, J. Quorum sensing and swarming migration in bacteria. *FEMS Microbiol. Rev.* **28,** 261–289 (2004).

115. Matsuyama, T. & Matsushita, M. Fractal morphogenesis by a bacterial cell population. *Crit. Rev. Microbiol.* **19,** 117–135 (1993).

116. Ben-Jacob, E. From snowflake formation to growth of bacterial colonies II: Cooperative formation of complex colonial patterns. *Contemp. Phys.* **38,** 205–241 (1997).

117. Pieuchot, L., Marteau, J., Guignandon, A., Dos Santos, T., Brigaud, I., Chauvy, P.-F., Cloatre, T., Ponche, A., Petithory, T., Rougerie, P., *et al.* Curvotaxis directs cell migration through cell-scale curvature landscapes. *Nat. Commun.* **9,** 3995 (2018).

118. Dell'Arciprete, D, Blow, M., Brown, A., Farrell, F., Lintuvuori, J. S., McVey, A., Marenduzzo, D & Poon, W. C. A growing bacterial colony in two dimensions as an active nematic. *Nat. Commun.* **9,** 1–9 (2018).

119. Budrene, E. O. & Berg, H. C. Dynamics of formation of symmetrical patterns by chemotactic bacteria. *Nature* **376,** 49–53 (1995).

120. Melton, D. Pattern formation during animal development. *Science* **252,** 234–241 (1991).

121. Murray, J. D., Maini, P. K. & Tranquillo, R. T. Mechanochemical models for generating biological pattern and form in development. *Phys. Rep.* **171,** 59–84 (1988).

122. Luo, N., Wang, S. & You, L. Synthetic pattern formation. *Biochemistry* **58,** 1478–1483 (2019).

123. Park, J.-A., Atia, L., Mitchel, J. A., Fredberg, J. J. & Butler, J. P. Collective migration and cell jamming in asthma, cancer and development. *J. Cell Sci.* **129,** 3375–3383 (2016).

124. Malinverno, C., Corallino, S., Giavazzi, F., Bergert, M., Li, Q., Leoni, M., Disanza, A., Frittoli, E., Oldani, A., Martini, E., *et al.* Endocytic reawakening of motility in jammed epithelia. *Nat. Mater.* **16,** 587–596 (2017).

125. Vecchio, S. L., Pertz, O., Szopos, M., Navoret, L. & Riveline, D. Spontaneous rotations in epithelia as an interplay between cell polarity and RhoA activity at boundaries. *bioRxiv* (2021).

126. Vedula, S. R. K., Hirata, H., Nai, M. H., Brugués, A., Toyama, Y., Trepat, X., Lim, C. T. & Ladoux, B. Epithelial bridges maintain tissue integrity during collective cell migration. *Nat. Mater.* **13,** 87–96 (2014).

127. Ascione, F., Caserta, S., Esposito, S., Villella, V. R., Maiuri, L., Nejad, M. R., Doostmohammadi, A., Yeomans, J. M. & Guido, S. Collective rotational motion of freely expanding T84 epithelial cell colonies. *J. R. Soc. Interface* **20,** 20220719 (2023).

128. Nejad, M. R. & Yeomans, J. M. Spontaneous rotation of active droplets in two and three dimensions. *arXiv preprint arXiv:2305.04018* (2023).

129. Tlili, S, Durande, M, Gay, C., Ladoux, B, Graner, F & Delanoë-Ayari, H. Migrating epithelial monolayer flows like a Maxwell viscoelastic liquid. *Phys. Rev. Lett.* **125,** 088102 (2020).

130. Mongera, A., Rowghanian, P., Gustafson, H. J., Shelton, E., Kealhofer, D. A., Carn, E. K., Serwane, F., Lucio, A. A., Giammona, J. & Campàs, O. A fluid-to-solid jamming transition underlies vertebrate body axis elongation. *Nature* **561,** 401–405 (2018).

131. Yevick, H. G., Duclos, G., Bonnet, I. & Silberzan, P. Architecture and migration of an epithelium on a cylindrical wire. *PNAS* **112,** 5944–5949 (2015).

132. Maître, J.-L. & Heisenberg, C.-P. The role of adhesion energy in controlling cell–cell contacts. *Curr. Opin. Cell* **23,** 508–514 (2011).

133. Balasubramaniam, L., Doostmohammadi, A., Saw, T. B., Narayana, G. H. N. S., Mueller, R., Dang, T., Thomas, M., Gupta, S., Sonam, S., Yap, A. S., *et al.* Investigating the nature of active forces in tissues reveals how contractile cells can form extensile monolayers. *Nat. Mater.* **20,** 1156 (2021).

134. Guillamat, P., Blanch-Mercader, C., Pernollet, G., Kruse, K. & Roux, A. Integer topological defects organize stresses driving tissue morphogenesis. *Nat. Mater.* **21,** 588–597 (2022).

135. Trushko, A., Di Meglio, I., Merzouki, A., Blanch-Mercader, C., Abuhattum, S., Guck, J., Alessandri, K., Nassoy, P., Kruse, K., Chopard, B., *et al.* Buckling of an epithelium growing under spherical confinement. *Dev. Cell* **54,** 655–668 (2020).

136. Petitjean, L., Reffay, M., Grasland-Mongrain, E., Poujade, M., Ladoux, B., Buguin, A. & Silberzan, P. Velocity Fields in a Collectively Migrating Epithelium. *Biophys. J.* **98,** 1790 –1800 (2010).

137. Mark, S., Shlomovitz, R., Gov, N. S., Poujade, M., Grasland-Mongrain, E. & Silberzan, P. Physical model of the dynamic instability in an expanding cell culture. *Biophys. J.* **98,** 361–370 (2010).

138. Duclos, G, Blanch-Mercader, C, Yashunsky, V, Salbreux, G, Joanny, J.-F., Prost, J & Silberzan, P. Spontaneous shear flow in confined cellular nematics. *Nat. Phys.* **14,** 728–732 (2018).

139. Großmann, R., Aranson, I. S. & Peruani, F. A particle-field approach bridges phase separation and collective motion in active matter. *Nat. Commun.* **11,** 1–7 (2020).

140. Zhang, G. & Yeomans, J. M. Active forces in confluent cell monolayers. *Phys. Rev. Lett.* **130,** 038202 (2023).

141. Saintillan, D. & Shelley, M. J. Instabilities and pattern formation in active particle suspensions: Kinetic theory and continuum simulations. *Phys. Rev. Lett.* **100,** 178103 (2008).

142. Meacock, O. J., Doostmohammadi, A., Foster, K. R., Yeomans, J. M. & Durham, W. M. Bacteria solve the problem of crowding by moving slowly. *Nat. Phys.* **17,** 205–210 (2021).

143. Mitchel, J. A., Das, A., O'Sullivan, M. J., Stancil, I. T., DeCamp, S. J., Koehler, S., Ocaña, O. H., Butler, J. P., Fredberg, J. J., Nieto, M. A., *et al.* In primary airway epithelial cells, the unjamming transition is distinct from the epithelial-to-mesenchymal transition. *Nat. Commun.* **11,** 1–14 (2020).

144. Lushi, E. & Peski, C. S. Modeling and simulation of active suspensions containing large numbers of interacting micro-swimmers. *Comput. Struct* **122,** 239–248 (2013).

145. Nejad, M. R. & Yeomans, J. M. Active extensile stress promotes 3D director orientations and flows. *Phys. Rev. Lett.* **128,** 048001 (2022).

146. Wensink, H. H., Dunkel, J., Heidenreich, S., Drescher, K., Goldstein, R. E., Löwen, H. & Yeomans, J. M. Meso-scale turbulence in living fluids. *PNAS* **109,** 14308–14313 (2012).

147. Nejad, M. R., Ruske, L. J., McCord, M., Zhang, J., Zhang, G., Notbohm, J. & Yeomans, J. M. Stress-shape misalignment in confluent cell layers. *arXiv preprint arXiv:2309.04224* (2023).

148. Vromans, A. J. & Giomi, L. Orientational properties of nematic disclinations. *Soft matter* **12,** 6490–6495 (2016).

149. Pellegrin, S. & Mellor, H. Actin stress fibres. *J. Cell Sci.* **120,** 3491–3499 (2007).

150. Beris, A. N., Edwards, B. J. & Edwards, B. J. *Thermodynamics of flowing systems: with internal microstructure* **36** (Oxford University Press on Demand, 1994).

151. Binysh, J., Kos, Z., Čopar, S., Ravnik, M. & Alexander, G. P. Three-dimensional active defect loops. *Phys. Rev. Lett.* **124,** 088001 (2020).

152. Binysh, J., Pollard, J. & Alexander, G. P. Geometry of bend: Singular lines and defects in twist-bend nematics. *Phys. Rev. Lett.* **125,** 047801 (2020).

153. You, Z., Pearce, D. J. G., Sengupta, A. & Giomi, L. Mono- to multilayer transition in growing bacterial colonies. *Phys. Rev. Lett.* **123,** 178001 (2019).

154. Chu, E. K., Kilic, O., Cho, H., Groisman, A. & Levchenko, A. Self-induced mechanical stress can trigger biofilm formation in uropathogenic Escherichia coli. *Nat. Commun.* **9,** 4087 (2018).

155. Duvernoy, M.-C., Mora, T., Ardré, M., Croquette, V., Bensimon, D., Quilliet, C., Ghigo, J.-M., Balland, M., Beloin, C., Lecuyer, S., *et al.* Asymmetric adhesion of rod-shaped bacteria controls microcolony morphogenesis. *Nat. Commun.* **9,** 1120 (2018).

156. Grobas, I., Polin, M. & Asally, M. Swarming bacteria undergo localized dynamic phase transition to form stress-induced biofilms. *Elife* **10,** e62632 (2021).

157. Nie, P., Alarcon, F., López-Montero, I., Orgaz, B., Valeriani, C. & Ciamarra, M. P. In-silico modeling of early-stage biofilm formation. *Soft Mater.* **19,** 346–358 (2021).

158. Simha, R. A. & Ramaswamy, S. Hydrodynamic fluctuations and instabilities in ordered suspensions of self-propelled particles. *Phys. Rev. Lett.* **89,** 058101 (2002).

159. Nejad, M. R. & Najafi, A. Chemotaxis mediated interactions can stabilize the hydrodynamic instabilities in active suspensions. *Soft Matter* **15,** 3248–3255 (2019).

160. Mozaffari, A., Zhang, R., Atzin, N. & de Pablo, J. J. Defect spirograph: Dynamical behavior of defects in spatially patterned active nematics. *Phys. Rev. Lett.* **126,** 227801 (2021).

161. Hemingway, E. J., Mishra, P., Marchetti, M. C. & Fielding, S. M. Correlation lengths in hydrodynamic models of active nematics. *Soft Matter* **12,** 7943–7952 (2016).

162. Shendruk, T. N., Thijssen, K., Yeomans, J. M. & Doostmohammadi, A. Twist-induced crossover from two-dimensional to three-dimensional turbulence in active nematics. *Phys. Rev. E* **98,** 010601 (2018).

163. Warren, M. R., Sun, H., Yan, Y., Cremer, J., Li, B. & Hwa, T. Spatiotemporal establishment of dense bacterial colonies growing on hard agar. *Elife* **8,** 41093 (2019).

164. Beroz, F., Yan, J., Meir, Y., Sabass, B., Stone, H. A., Bassler, B. L. & Wingreen, N. S. Verticalization of bacterial biofilms. *Nat. Phys.* **14,** 954–960 (2018).

165. Grant, M. A., Wacław, B., Allen, R. J. & Cicuta, P. The role of mechanical forces in the planar-to-bulk transition in growing Escherichia coli microcolonies. *J. R. Soc. Interface* **11,** 20140400 (2014).

166. Boyer, D., Mather, W., Mondragón-Palomino, O., Orozco-Fuentes, S., Danino, T., Hasty, J. & Tsimring, L. S. Buckling instability in ordered bacterial colonies. *Phys Biol.* **8,** 026008 (2011).

167. Su, P.-T., Liao, C.-T., Roan, J.-R., Wang, S.-H., Chiou, A. & Syu, W.-J. Bacterial colony from two-dimensional division to three-dimensional development. *PLOS ONE* **7,** 1–10 (Nov. 2012).

168. Demus, D., Goodby, J. W., Gray, G. W., Spiess, H. W. & Vill, V. *Handbook of liquid crystals, volume 2A: low molecular weight liquid crystals I: calamitic liquid crystals* (John Wiley & Sons, 2011).

169. Schiele, K. & Trimper, S. On the elastic constants of a nematic liquid crystal. *Physica Sta. Solid.* **118,** 267–274 (1983).

170. Hobdell, J. & Windle, A. A numerical technique for predicting microstructure in liquid crystalline polymers. *Liquid crystals* **23,** 157–173 (1997).